Automatic UAV-borne Monitoring of Inland Waters with Hyperspectral Sensors

Zur Erlangung des akademischen Grades eines

DOKTOR-INGENIEURS

von der KIT-Fakultät für
Bauingenieur-, Geo- und Umweltwissenschaften
des Karlsruher Instituts für Technologie (KIT)

genehmigte

DISSERTATION

von

M.Sc. Jens Kern
aus Speyer

Tag der mündlichen Prüfung:	06.02.2024
Referent:	Prof. Dr.-Ing. habil. Stefan Hinz
Korreferent:	Prof. Dr.-Ing. Tobias Bleninger

Karlsruhe 2024

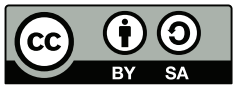

Kurzfassung

Wasser ist für viele Bereiche des täglichen Lebens eine wichtige Ressource, deren Qualität kontinuierlich überwacht werden muss. Dies gilt insbesondere für Oberflächengewässer wie Trinkwasserreservoire, die stärker als Grundwasser Umwelteinflüssen ausgesetzt sind. Häufig werden die zur Überwachung notwendigen Parameter arbeits- und kostenintensiv durch in-situ Messungen oder durch die Analyse von Wasserproben ermittelt. Viele relevante Wasserqualitätsparameter, wie z.B. der Schwebstoffgehalt, die Chlorphyll-a Konzentration und die Temperatur der Wasseroberläche können auch mit Fernerkundungssensoren erfasst werden. Insbesondere für die Fernerkundung der Ozeane werden traditionell multispektrale Satelliten eingesetzt. Flugzeuggestützte Systeme hingegen ermöglichen eine flexiblere Datenerfassung zu gewünschten Zeitpunkten, sind jedoch kostenintensiv und erfordern eine vorgegebene Infrastruktur sowie ausgebildete Piloten. Seit einigen Jahren sind kompakte, bildgebende hyperspektrale Sensoren kommerziell verfügbar, die in kleine UAVs integriert werden können. Dies ermöglicht im Gegensatz zu anderen Fernerkundungsplattformen eine kostengünstige, räumlich und zeitlich flexible Datenerfassung. Diese leichten und ungekühlten Sensoren haben meist eine weniger stabile Sensorcharakteristik und Einflüsse wie Wind und wechselnde Bewölkung können die Datenerfassung und -auswertung erschweren. Daher sind bisher keine vollständig integrierten Systeme kommerziell verfügbar, die eine automatisierte und damit kostengünstige Auswertung der Daten ermöglichen.
Im Rahmen dieser Arbeit wird ein Sensorsystem, bestehend aus einer Wärmebildkamera, einer Hyperspektralkamera und einem weiteren Spektrometer zur Messung der einfallenden Solarstrahlung, auf einem kompakten UAV integriert. Darüber hinaus werden Methoden entwickelt, die eine weitgehend automatisierte Datenverarbeitung ermöglichen. Als Ergebnis erhält der Nutzer zuverlässige Parameterkarten der Wasseroberflächentemperatur und der Schwebstoffkonzentration. Die entwickelten Methoden werden jeweils anhand realer Daten einer Messkampagne validiert. Die Methoden und Ergebnisse zur Kalibrierung der Spektralsensoren werden vorgestellt. Für die Wärmebildkamera, die aufgrund stark variierender Sensorcharakteristik nicht vorab kalibriert werden kann, werden datengetriebene Methoden von der Korrektur bis zur Berechnung von Mosaiken aus Einzelbildern entwickelt.
Zur Schätzung der Parameter aus den hyperspektralen Bildern werden maschinelle Lernverfahren eingesetzt. Die Modelle werden ausschließlich mit simulierten Daten trainiert und anschließend mit realen Daten evaluiert. Die entwickelten Postprocessing-Methoden berücksichtigen dabei auch Einflüsse wie die Totalreflexion des Sonnenlichts an der Wasseroberfläche und auftretende Wolkenschatten bei wechselnder Bewölkung. Die Evaluierung zeigt hier, dass die maschinellen Lernverfahren ANN und CNN im Vergleich zu einfacheren Verfahren bessere Ergebnisse liefern können und die Parameterschätzung auch weniger durch geringe Wassertiefen beeinflusst wird. Durch die entwickelten Methoden und die mit dem System gewonnenen Erkenntnisse leistet diese Arbeit einen Beitrag zur automatisierten Fernerkundung von Wasserqualitätsparametern mit kostengünstiger mobiler Sensorik.

Abstract

Water is a relevant resource for many areas of our daily lives, and its quality must be continuously monitored. This applies particularly to surface waters such as drinking water reservoirs, which are more exposed to environmental influences than groundwater. The parameters required for monitoring are often determined through labor-intensive and costly in-situ measurements or by analyzing water samples. Many relevant water quality parameters, such as the total suspended solids concentration, the chlorophyll-a concentration, and the water surface temperature can also be observed using remote sensing sensors. Multispectral satellites are traditionally used for remote sensing of the oceans in particular. On the other hand, airborne systems allow a more flexible data acquisition at desired times but are cost-intensive and require a given infrastructure and professional pilots. Compact hyperspectral imaging sensors that can be integrated into small UAVs have been commercially available for several years. In contrast to other remote sensing platforms, this enables cost-effective, spatially and temporally flexible data acquisition. These lightweight and uncooled sensors usually have less stable sensor characteristics, and influences such as wind and changing cloud cover can make data acquisition and evaluation more difficult. As a result, fully integrated systems enabling automated and cost-effective data evaluation are not yet commercially available.

This work integrates a sensor system consisting of a thermal imaging camera, a hyperspectral camera, and a further spectrometer for measuring the incident solar irradiance on a compact UAV. In addition, methods are developed that enable largely automated data processing. As a result, the user receives reliable parameter maps of the water surface temperature and the suspended solids concentration. The methods developed are validated using real data acquired during a measurement campaign. The methods and results for calibrating the spectral sensors are presented. Due to varying sensor characteristics, the thermal camera cannot be calibrated in advance. Therefore, data-driven methods for image correction and calculating mosaics from the individual images are developed.

Machine learning methods are used to estimate the parameters from the hyperspectral images. The models are trained exclusively with simulated data and then evaluated with real data. The developed post-processing methods also consider influences such as the total reflection of sunlight on the water surface and cloud shadows that occur when cloud cover changes. The evaluation shows that the machine learning methods ANN and CNN can achieve better results than simpler methods. Also, the parameter estimation is less influenced by shallow water depth. This work contributes to automated remote sensing of water quality parameters with low-cost mobile sensors through the methods developed and the knowledge gained with the system.

Acknowledgement

First, I would like to express my sincere gratitude to my supervisor, Prof. Dr. Stefan Hinz. For the offer to work at the IPF, the ongoing support and the opportunity to work on further projects beyond the MuDaK-WRM project and thus to be able to complete this thesis.

Second, a thank you to my direct supervisor, Dr. Andreas Schenk, for the constructive, critical comments during my entire time at the IPF, especially in the last months, which have always brought this work forward. In addition, for the measurement campaigns in Germany and Brazil, and the many activities outside of work.

Third, I would like to thank everyone involved in the MuDaK-WRM project for the excellent professional and friendly environment.
In particular, I would like to thank Prof. Dr. Tobias Bleninger, who organized meetings, logistics, laboratory analyses, and much more. I would also like to thank him for his constant interest in my work, and I am delighted that he is the co-referee of my thesis.
Also, I thank Prof. Dr. Jorge Centeno, who supported me during measurement campaigns and at whose chair I could spend a few weeks.
Special thanks also go to Dr. José Eduardo Gonçalves, who accompanied me on almost all field trips. Without his knowledge of dealing with UAVs, many campaign days would have been lost. The opportunity to use the electronics lab of SIMEPAR. And, of course, all the leisure activities and the road trip to Minas Gerais.
Thanks also to Adrian, Betty, Carla, Ilich, Klajdi, Lisa, Mario, Pedrosa, Stephan.

I want to thank Dr.-Ing. Klaus Trampert, who supported me in calibrating the spectral sensors and made it possible for me to work in the laboratories of LTI at KIT.

I thank the Graduate School of Climate and Environment (GRACE) at KIT for financially supporting this work and my stay at the UFPR in Curitiba.

Next, I would like to thank all my colleagues at the IPF. For the good and pleasant cooperation in the projects and the professional input. The open culture and the harmonic atmosphere have always motivated me to continue completing this thesis. I would also like to thank you for all the events outside of work, which were enriching in many ways.

I would not like to forget the students who collected data and explored further areas in the context of bachelor's and master's theses.

Thanks also to Christian Starck, Kai Dierenbach, and Philipp Maier for reading through this work and for their valuable comments.

I want to thank my parents, Andrea and Jürgen, for their constant and unconditional support. Also, my brother, Lars, who spent some weekend shifts with me during his studies and the many moments we spent together.

Finally, to you, Xiaoting, thank you for everything: for always being there for me and understanding the time I spent on this work.

Contents

CHAPTER 1

Introduction

Water is a relevant resource whose world wide consumption has sixfold during the last 100 years and further increases by 1% per year [1]. The availability of fresh and clean water directly affects health [2], energy production [3], agriculture [4], industrial development [5] and a lot of other parts of our daily life. Due to climate change, it is very likely, that in regions that suffer from water stress, the situation will get worse and even regions with sufficient water resources will face periods with limited availability of water [6]. For example, higher water temperatures and less dissolved oxygen will harm freshwater ecosystems and can degrade water quality to an extent that should not be underestimated. Due to the importance of inland waters, in many countries and regions they are also given special attention at the legal and political level, for example, with the European Water Framework Directive [7] and the US Clean Water Act [8]. Especially surface waters are much more affected by annual and long-term climate variability than groundwater. Therefore, particular attention must be paid to the monitoring and management of drinking water reservoirs that provide drinking water for millions of people around the world. Key parameters that should be monitored continuously are, among others, the temperature of the water, total suspended solids (TSS) and the chlorophyll-a (chl-a) concentration [9].

Traditionally, the monitoring of water quality parameters is done with the help of in-situ measuring probes or the analysis of water samples, which is labor-intensive and mostly limited to single measuring points for a few water bodies. This means that especially short-term phenomena such as algal blooms and their spatial distribution cannot be captured to full extent [10, 11].

Another method for monitoring water quality parameters is remote sensing. Passive sensors can be used to monitor the water temperature and also many of the different water constituents, such as TSS and chl-a, as a proxy for phytoplankton abundance, which are optically significant and influence the light reflected from the water body through absorption and scattering processes [12, 13]. The measurement and analysis of the light reflected by the water body allows to conclude about the concentration of the corresponding parameter.

The remote sensing of water quality parameters can be very well investigated with ground-based systems like point spectrometers to further optimize the methods for parameter estimation. However, the simple handling and mostly good spectral properties are, like the in-situ probes, opposed by the limitation to single point measurements.

In satellite-based multispectral remote sensing, on the other hand, these properties have been used for decades to monitor the oceans, and in the last 30 years, the theories of optical oceanography are transferred to inland waters where remote sensing of water quality parameters is far less successful [12]. With this, on a global scale, remote sensing is able to reveal large-scale processes, but until today, lacks on high spatial and temporal resolution, which is not always sufficient for applications like the monitoring on small scales [1]. As a result, it is often impossible to monitor the processes in inland waters, some of which are very small and usually have complex optical characteristics [10]. Last but not least, it is a major disadvantage of satellite-based remote sensing that the acquisition times are not freely selectable and, for example, cloud cover further limits the availability of usable data.

In addition to multispectral [14, 15, 16] and more recently hyperspectral [17, 18, 19] satellite missions, airborne campaigns [20, 21, 22] were also conducted to collect areal hyperspectral data from inland waters and perform mapping of water quality parameters such as TSS and chl-a. Airborne campaigns make it possible to collect data with very high spatial resolution at desired times, in contrast to satellites. However, the sensor technology used is usually expensive, and specially prepared aircraft are required for data acquisition, which further complicates the application and makes it expensive and thus not economically attractive for continuous monitoring tasks.

The recent progress in the development of small UAV and new lightweight sensors such as compact hyperspectral and thermal cameras enable new possibilities for environmental monitoring tasks [23, 24, 25, 26]. Methods used with space and airborne remote sensing are now transferred to these systems, which will make it possible to perform continuous monitoring tasks with high spatial and temporal resolution at low costs for areas of some square kilometers [27, 28]. Also, in the field of remote sensing of water quality parameters, these systems have been finding their way into research now, for example, to map the temperature of the water surface or parameters such as TSS and chl-a with high spatial and temporal resolution [29, 30, 28].

1.1 Research Goals

The advantages of compact UAVs and mobile sensors are accompanied by several disadvantages and challenges. Many UAVs are vertical take-off multicopters that have a limited range due to the high energy consumption and the weight of the sensors. Also, environmental influences like wind gusts cause unwanted movements of the UAV and the sensors attached to it, which complicate the georeferencing of the images. In addition, the mostly uncooled low budget sensors have a poorer SNR and lower dynamic range compared to sensors for

aircraft and satellites. Furthermore, these innovative hyperspectral sensors suffer from less geometric and radiometric stability and optical limitations compared to the traditional sensors for airborne missions. Therefore, characterization and calibration of the sensors need to be done before data acquisition [31]. Another challenge after successful data acquisition is the reliable and automated analysis of the collected data, for which no suitable software packages are available today. Challenges here are the georeferencing of the data over water, where the use of traditional image-based methods is not possible over water. Using UAV borne systems provides the advantage of flying below clouds, but there are also disadvantages due to fastly changing irradiance caused by cloud shadows. In general, a system which can automate the process from data acquisition to cosistent maps of water quality parameters is not available.

This work aims to set up a multimodal system with a thermal and a hyperspectral camera on a compact UAV and the application of this system for the measurement and mapping of water surface temperature and the estimation of water quality parameters in the context of a research project. The following questions will be addressed in particular:

1. **Can a low budget multimodal sensor system mounted on a UAV be used to ...**
   a) **... acquire data in an easy way?**
      Currently, no fully integrated systems are commercially available and spectral sensors usually have to be calibrated by the user.
   b) **... automatically process the data?**
      An automated process is absolutely essential for cost-effective use. This includes in particular the preprocessing of the data and the subsequent parameter estimation.
   c) **... generate consistent and reliable parameter maps?**
      For the use and evaluation of the results, it is necessary that the generated maps are consistent and influenced as little as possible by ambient influences.
2. **Is it possible to use the system below the cloud cover?**
   For continuous monitoring, it is essential to obtain data at fixed time intervals. Satellite remote sensing cannot guarantee this due to the often prevalent cloud cover. UAVs, on the other hand, can fly below the clouds
3. **Is it possible to use only few ground truth data?**
   The collection of ground truth data to train and validate machine learning models is very time consuming and costly. What are the alternatives to the synchronous acquisition of a vast amount of reference samples?

1.2 Thesis Outline

This thesis is divided into nine chapters. Chapters 1 to 3 introduce the topic, describe necessary basics (Chap. 2) and embed the work in the context of recent research also discussing the challenges mentioned above (Chap. 3). Because of the importance of the calibration of the spectral sensors for the success of this work, Chap. 4 describes the sensor system and discusses the methods and results of the calibration of the spectral sensors. Data collected during a measurement campaign at the drinking water reservoir Passaúna in the west of Curitiba, Brazil in 2020 are presented in Chap. 5. Remote sensing of the water surface temperature using a thermal camera, including recent research and developed methods, are considered separately in Chap. 6. Subsequently, Chap. 7 deals with the spectral data acquired with the sensor system, the developed processing tools and the obtained results in the context of parameter estimation using the example of TSS concentration. In Chap. 8 the summary of the work and the embedding of the results in the context of current research work is given. Finally, the conclusions concerning the previously presented research questions are presented and an outlook on future developments in the field of automatic remote sensing of water quality parameters with small UAVs is given in Chap. 9.

This work contributes to the automated water quality monitoring of inland waters using low budget imaging sensor systems on UAVs. These small systems can provide data with a high temporal and spatial resolution which is a clear advantage compared to traditional methods like in-situ sampling or satellite remote sensing. To be cost-effective, these systems need to be easy to use and it must be possible to process the data in an automated way. It should be possible even for non experts to generate consistent and reliable maps of the water surface temperature, total suspended solids concentration and other parameters without time consuming interaction during the processing from raw data to final image mosaics.

CHAPTER 2

Fundamentals and Methods

Light incident on water interacts in different ways. Remote sensing uses the radiation leaving the water body in relation to the incident radiation to conclude about the composition of the water body. This chapter first presents typical, optically significant constituents of inland waters and their interaction with light. After this, it introduces the quantities observable by remote sensing and the influences affecting the remote sensing observations. Simulated spectra show typical characteristics as a function of the concentration of water constituents. Finally, the chapter deals with the methods for estimating the parameters from the remote sensing data.

A standard work on optical properties of waters is The Oceanic Optics Book by Curtis D. Mobley [13] which has its origins in the methods of ocean color remote sensing. Many of the fundamentals discussed in this chapter refer to this book. Another book about the remote sensing of the oceans and the role of light in aquatic ecosystems is Light and photosynthesis in aquatic ecosystems by John T. O. Kirk [32]. A focus on the remote sensing of coastal aquatic environments can be found e.g. in [33, 34]. In [12] fundamentals and studies related to the remote sensing of inland waters are presented. A tool to understand, analyze and simulate spectral measurements of open waters is the freely available software WASI (Water Colour Simulator, [35]).

2.1 Light and Water

Essentially for this work is the range of the visible and near infrared (NIR) of the electromagnetic spectrum which can be measured with spectrometers. Relevant measures will be discussed in the following.

Many substances in waters, whether dissolved or particulate, are optically significant and highly variable [13]. Due to the combination of physical properties of the constituents (e.g. particle size and shape, etc.) with optical properties, optical measurements can be used to obtain information about the constituents in aquatic systems. These inherent optical

properties (IOP) are based on absorption and scattering and are linked to the water [36]. Therefore, these parameters can be determined equally in-situ in the water and in the laboratory [13]. In a given volume of water, absorption A, scattering S, and transmittance T can be determined, where fluorescence is to be seen as part of the scattering processes. The sum of these must be $A + S + T = 1$ due to the conservation of energy. These properties of water change in the presence of e.g. phytoplankton and mineral particles by magnitudes compared to pure water. The following components are particularly relevant for water: Absorption by water (see Fig. 2.1a), phytoplankton (see Fig. 2.1b), colored dissolved organic matter, mineral particles, and scattering by water and particles present in it [12]. The associated most relevant IOPs are the absorption coefficient and the backscattering coefficient.

Phytoplankton

Phytoplankton is one of the most important parameters for the monitoring of waters due to its importance for the food chain and the human health, as some of the species are toxic. Especially, due to the increase of algal blooms in waters used e.g. for drinking water production and irrigation, the monitoring of the concentration and composition of phytoplankton is of increasing interest [11, 37]. A major component of phytoplankton is chlorophyll-a (chl-a), which was already measured in the 1970s using remote sensing methods [38]. There are many different phytoplankton species which all have different spectral characteristics. In Fig. 2.1b the absorption coefficients of two classes (cyanobacteria and green algae) are visualized. The third class represents a combined absorption spectrum of the typical phytoplankton mixture of Lake Constance (Phyto) where multiple present species result in a combined signal. Characteristic for phytoplankton absorption is the peak at ca. 670 nm. Besides absorption, there is also the emission of light due to chlorophyll fluorescence which is not covered here as it is beyond the scope of this work and it is referred to the literature [32, 12, 13]. According to [39] the relationship between phytoplankton and inorganic particles is used for classification into case-I and case-II waters. Case-I is used for waters where the composition is strongly influenced by phytoplankton (open ocean), case-II for all other waters where also e.g. mineral particles have a significant impact on the water color (coastal, inland waters).

CDOM

Colored Dissolved Organic Matters (CDOM, gilvin, yellow substance), are formed during the decomposition of organic material in soil or water [32] and have a yellow or brown color [40]. In inland and coastal waters, CDOM usually dominates absorption [12]. Larger concentrations affect mainly the reflectance in the blue and green regions of the spectrum (especially below 500 nm) [41]. The shape of the spectral absorption curve can be approximated by an exponential function [42, 13]. Since CDOM only absorbs radiation and does

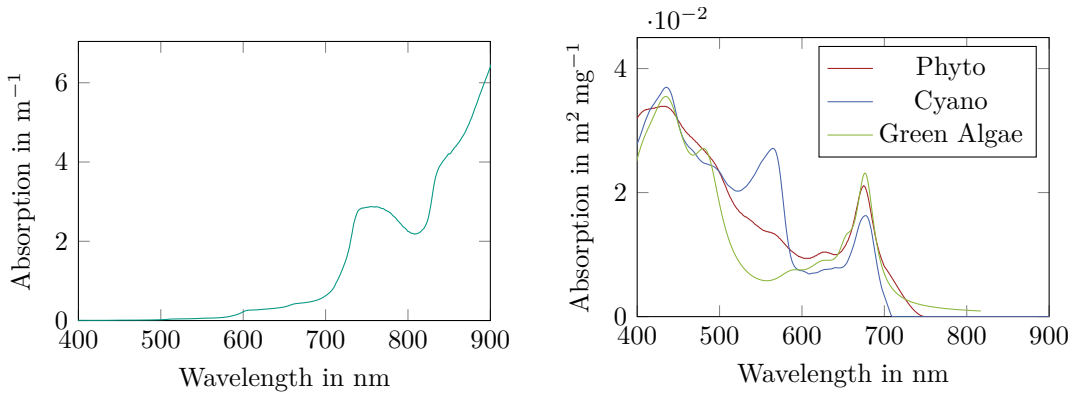

(a) Pure water.

(b) Phytoplankton.

Figure (2.1) Absorption coefficients of (a) pure water and (b) phytoplankton. The spectrum labeled Phyto in (b) represents a typical mixture for Lake Constance. The label Cyano in (b) stands for cyanobacteria. The single phytoplankton classes have highly variable absorption coefficients. The signal of multiple present species in the water result in a combined absorption spectrum as it is shown for the typical phytoplankton mixture of Lake Constance (Phyto). The spectra are exported from WASI [35].

not reflect it, waters with high CDOM concentration have low reflectance. In particular, the determination of CDOM using satellite remote sensing is difficult because atmospheric correction in the blue spectral region is difficult and low concentrations are usually obscured by backscattering of light from suspended particles [43].

Total Suspended Solids

Natural waters always contain a variety of particles that scatter light [32]. These are e.g. mineral particles, phytoplankton, bacteria, etc. The sum of all these components is called total suspended solids (TSS). Since suspended sediment also influences primary production, e.g. by binding phosphorus, the determination of TSS is of interest [44]. In addition, especially in shallow lakes, the input of TSS contributes to siltation and prevents light penetration into deeper layers of the water, which can affect the organisms living there [45]. The scattering of light depends mainly on the size and concentration of the particles, while the absorption properties depend strongly on the constituents [12]. In general, a higher concentration of TSS contributes to higher reflectance (R_{rs}, see Sect. 2.2) values [46], which also results in the characteristic local reflectance peak at approx. 800 nm (see Fig. 2.4a).

Apparent Optical Properties

While the IOP (absorption and backscattering coefficients) can be determined well in the laboratory with the help of sensors, the direct measurement with remote sensing methods is not possible. Therefore, the measurement of the AOP is used. AOP are properties of water

that depend on the IOP and the geometry of the radiance distribution and display enough regular features and stability to be useful descriptors of a water body [13]. They are defined as ratios of radiometric quantities since these are less dependent on the light field than the quantities themselves [12]. The AOP relevant for this work is the remote sensing ratio (Eq. 2.3) measured above the water surface which is formed as the ratio of incident solar radiation into the water and radiation reflected from the water body. A further explanation using the example of remote sensing of water quality parameters using UAV carried sensor systems follows in the next section.

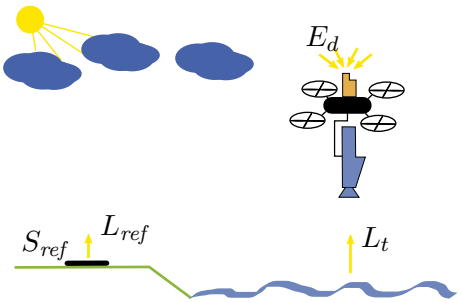

Figure (2.2) Remote sensing of water using a reference panel with known spectral characteristics S_{ref} to measures L_{ref} and calculate downwelling irradiance E_d or an upward looking spectrometer attached to the UAV to measure E_d. The upwelling radiance L_t is measured by the downward looking hyperspectral camera.

2.2 Remote Sensing of Water

Passive remote sensing of water quality parameters has its origins in ocean color remote sensing with satellites more than forty years ago [37, 13]. While the focus at that time was on an intensive understanding of oceans, the exploration of the optically more complex inland waters is increasingly developing, which is only possible due to the advancement of sensors towards higher spatial and spectral resolutions. Mostly, the passive remote sensing of water uses the spectral bands in VIS, NIR and TIR. Here, the use of reflected radiation in VIS and NIR measured by hyperspectral sensors above the water surface on UAVs is discussed. Therefore, all notations are intended for measurements above water.

Remote sensing reflectance is usually chosen as the starting point for calculating water quality parameters from remote sensing data:

$$R_{rs} = \frac{L_w}{E_d}[sr^{-1}] \quad . \tag{2.1}$$

This is formed from the water leaving radiance L_w and the downwelling irradiance E_d. L_w is the part of the incident radiation that has interacted with the water body and leaves it through the water surface in a certain direction with a certain solid angle. Schematically, for the case of the use of a UAV, this is shown in Fig. 2.2.

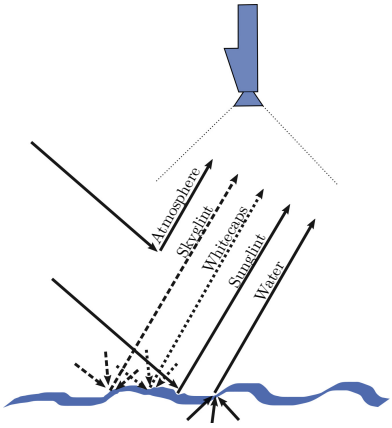

Figure (2.3) The received signal at the downward looking camera is a combination of multiple signals as e.g. the water leaving radiance and scattered light on particles in the atmosphere and the total reflection of sunlight at the water surface. Adopted from [47].

The calculation of the reflectance is often done in UAV campaigns using reference panels where not E_d but L_{ref} is measured [46]. Taking into account the spectral properties S_{ref} of the reference panel, E_d can be determined:

$$E_d = \pi \frac{L_{ref}}{S_{ref}} [Wm^{-2}] \quad . \tag{2.2}$$

Recently, UAV systems have been supplemented by an additional spectrometer to be able to continuously measure the incident radiation with the simultaneous measurement of the downwelling irradiance. Since the measurement of radiance and irradiance is done with two different sensors, an exact calibration of the sensors is necessary [13].

While actually the water leaving radiance L_w is of interest, in remote sensing the combined signal L_t is measured as the sum of L_w and a variety of other signals at the sensor. This results in the ratio named remote sensing ratio [13], which is defined here for measurements above the water surface:

$$RSR = \frac{L_t}{E_d} [sr^{-1}] \quad , with \tag{2.3}$$

$$L_t = L_w + L_{sun} + L_{sky} + L_{wc} + L_{atm} \quad . \tag{2.4}$$

These ambient influences (see Fig. 2.3) are e.g. reflection of the sun at the water surface (sun glint, L_{sun}), reflection of the sky (sky glint, L_{sky}), radiance reflected by whitecaps and foam (L_{wc}), and scattering in the atmosphere (L_{atm}) [47]. Sun glint is the strongest overlay of the L_w signal and due to the possible high intensity it can lead to saturated pixels on the sensor and thus to data that cannot be evaluated and must be taken into account accordingly when planning a campaign and later data evaluation.

The correction of sun glint and sky glint is feasible with additional effort [48]. It requires measurements of the sky radiance with another sensor particularly in the area of the sky that

is reflected on the water surface. During the processing of the measurements, a factor ρ must be calculated to determine the reflected proportion of sun and sky glint on the measurement L_t, which depends on several factors. These are, e.g. wind speed (as wind induces surface roughness [49]), sensor field of view, prevailing cloud cover, and the inclination and azimuth of sensor and sun [50]. Therefore, the determination is not trivial and must be elaborately modeled using numerical simulations, which can be performed e.g. with the commercially available radiative transfer numerical model Hydrolight [51].

Often R_{rs} and RSR are given in % when multiplied with 100. When reflectance is mentioned in this work, RSR is always meant.

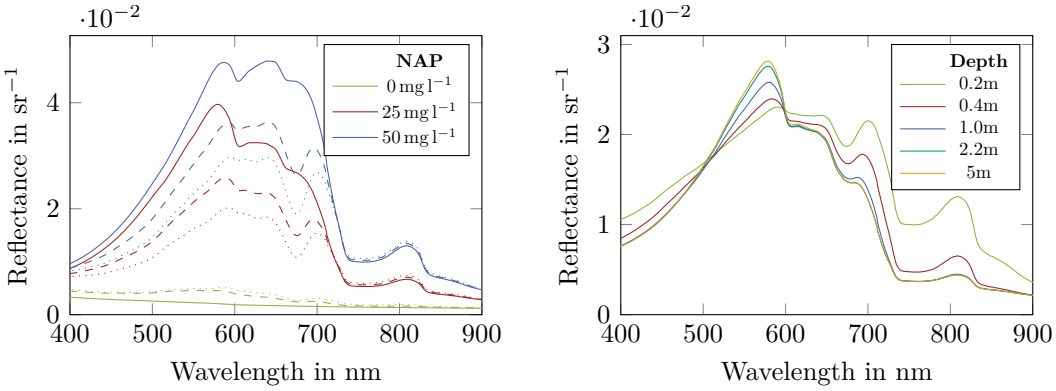

(a) Variation of Phyto and NAP.

(b) Variation of the water depth.

Figure (2.4) Simulated reflectance spectra with variation of (a) phytoplankton (Phyto) and non algal particles (NAP), and (b) water depth in the case of shallow water and bottom type sand. In (a) the different colors represent the variation of the non algal particle concentration in $\mathrm{mg\,l^{-1}}$: $0\,\mathrm{mg\,l^{-1}}$ (green), $25\,\mathrm{mg\,l^{-1}}$ (red), and $50\,\mathrm{mg\,l^{-1}}$ (blue). The line style represents the concentration of phytoplanktion in $\mathrm{\mu g\,l^{-1}}$: $0\,\mathrm{\mu g\,l^{-1}}$ (solid), $25\,\mathrm{\mu g\,l^{-1}}$ (dashed), and $50\,\mathrm{\mu g\,l^{-1}}$ (dotted). In (b) low concentrations for NAP and phytoplankton where chosen.
The spectra were generated with WASI [35].

In Fig. 2.4, exemplary reflectance spectra are shown which were simulated with WASI [35]. The left plot shows the influence of present phytoplankton and non algal particles (NAP) in varying concentrations on the reflectance spectrum for the case of deep water. With increasing NAP, the reflectance increases overall. An increasing concentration of phytoplankton increases the dent at approx. 670 nm due to absorption (cf. Fig. 2.1b).
For shallow water the bottom of the water body also influences the measured reflectance spectra which is visualized in Fig. 2.4b. Low concentrations for phytoplankton ($5\,\mathrm{\mu g\,l^{-1}}$) and NAP ($15\,\mathrm{mg\,l^{-1}}$), and the bottom type sand were chosen in WASI to generate this plot. The water depth was varied from 0.2 m to 5 m. A variation of the reflectance depending on the water depth is particularly visible in the region above 700 nm. Also, the peak at approx. 570 nm increases. For water depths larger than 2.2 m, almost no further variation is visible in this case.

2.3 Water Quality Parameter Retrieval

Based on the measured AOP, three types of estimation methods for determining the water quality parameters can be distinguished [37]. Analytical models invert the physical model which is based on IOP and AOP. In contrast, empirical models use existing data sets to build models for the parameter estimation of unknown data sets. Whereas traditional empirical models are often based on linear relationships, the more and more widespread machine learning methods can also represent complex non-linear relationships and have therefore been applied in parameter estimation for some years.

Analytical Models

The knowledge about the IOP facilitates the development of analytical models to simulate the spectral properties of arbitrary waters. Further assumptions, e.g. the composition of the atmosphere, allow the calculation of the AOP. In addition to forward modeling, inversion of these models is also possible. This approach is followed in the estimation of water quality parameters from remote sensing data using analytical models. Even though these models allow to represent the complex physics, the inversion is not easily possible. Many constituents have IOPs that overlap spectrally and thus an ambiguous solution is possible. Also assumptions about the atmosphere contribute to errors in the calculation and inversion. In general, the application of analytical models to estimate water quality parameters requires expert knowledge and, partly, additional in-situ measurements to determine starting values for the inversion.

Empirical Models

A common method for estimating water quality parameters are empirical models. Specific wavelength bands are selected either automatically or manually to be related to the desired parameters either directly or by using the relationships of several bands. In the literature this is called band ratio (BR) and the estimation of parameters is based on previously determined regressions between these ratios and the corresponding parameters. Especially these models are applied to the multispectral data of satellites. Whereas the choice of the used bands is transferable to other data, the chosen parameters of the models are often bound to one water body and are not transferable. Therefore, it is usually necessary to have corresponding reference measurements for each water body.

Machine Learning Models

A special form of empirical models are machine learning models. In recent years, due to the increased computational capacity and the increasing spread in almost all scientific fields, these methods are also used in the evaluation of remote sensing data for the regression of

water quality parameters. In contrast to image classification tasks, the data for the regression of continuous water quality parameters are mostly reflectance spectra of dimension one. While traditional empirical models are simple and often based on linear relationships, these methods also allow the mapping of complex nonlinear relationships between input data and target variables. In several studies, these methods performed well and can even outperform existing traditional empirical models [37]. However, for a reliable application, a huge amount of data is needed to obtain generalizing models [52]. Also, a deep understanding of the methods is required to train the models with the available data in such a way that they do not exhibit overfitting or underfitting. All supervised machine learning models have in common that the data to be used must be preprocessed. The data should be cleaned of large outliers as far as possible and normalized if necessary to ensure successful training of the models. Furthermore, it must be ensured that, ideally, independent data are used for training and validation during model optimization, and testing of the final models, so that the generalizability of the models can be assessed.

- PLS

  Especially when processing spectral data, Partial Least Squares regression (PLS) [53] is an often used robust method [54]. PLS is a bilinear factor model and can handle a high dimension of observations and multicollinearity by projecting the observations and the unknowns into new spaces. PLS has similarities with PCA, but in contrast, it also includes the parameter space of the target variable by searching for the corresponding direction of the maximum variance in the target parameter space to the direction in the observation space. In short, PLS performs a dimensionality reduction but also considers the target parameter space in order to take into account variables with low variance but high influence on the target size, which is a decisive advantage compared to PCR. The advantages of PLS are ease of use, fast training time, and applicability to small data sets [54]. The disadvantages are usually a reduced performance and generalizability compared to other machine learning models like ANN. The application of PLS on spectral data to estimate water quality parameters is presented for example in [55, 56, 57].

- RF

  Random Forests (RF) [58] are part of the ensemble methods where multiple base estimators are combined to improve generalizability. An RF combines several decision trees, each of which is trained with a randomly chosen subset (a sample drawn with replacement) of the training data. The best split for a node of a tree is found by using all features or a random subset with a chosen maximum size. By using these two sources of randomness the variance of the estimator and the probability of overfitting are reduced. The injected randomness can lead to decoupled prediction errors, which are reduced by averaging the individual predictions. An advantage of RF is a relatively short training and evaluation time due to the parallelizability even with large data sets.

Furthermore, the results can be interpreted with the help of the feature importance [54]. The application of RF on spectral data to estimate water quality parameters is presented for example in [59, 60, 61].

- ANN

Artificial neural networks (ANN) are inspired by the architecture of the brain and work with artificial neurons. However, these have come a long way from their biological cousins [62]. While the first mention can be traced back to 1943, for a long time there was no intensive research on ANNs. Only in the 1990s and particularly since the 2010s, however, ANNs are no longer to be excluded from modern data processing. An ANN consists of artificial neurons (units) which are connected to each other. The neurons consist of input connections and corresponding weights. The weighted inputs are then applied to an activation function and the result is passed on to the next neurons. For example, using the backpropagation method, it is then possible to adjust all weights in the ANN to minimize the estimation error and optimize the ANN for a regression problem [63]. ANN usually consist of several neurons which are built up in several layers and are fully connected to each other. The simplest structure consists of an input layer with a certain number of neurons and an output layer with one neuron. If further layers (hidden layers) are inserted between the two layers, one speaks of a deep neural network. In the context of regression tasks, the output layer has a linear activation function. Currently, deep neural networks usually use the ReLU activation function [64]. To optimize the weights mostly the Adam algorithm is used [65]. ANN can handle large datasets and their structure is adaptable to individual problems even to solve nonlinear problems. But they need, depending on the structure of the ANN and the regression problem, a large amount of data which lead to long training times and the whole process can be seen as a black box system. Applications of ANN to estimate water quality parameters from spectral data can be found in [66, 67].

- CNN

A special kind of neural networks are convolutional neural networks (CNN) [68] which have at least one input, one convolutional and one output layer. Usually, fully connected layers are integrated into the network between the convolutional layers and the output layer. The idea of CNNs is to extract local features using convolution kernels (filters), which are learnable filters, thus automating the manual step of filter engineering inevitable in traditional methods [68]. In a CNN, every element of the convolution kernel is used at every position of the input (except possibly edge pixels). This reduces the number of free parameters (parameter sharing), since only one set of parameters is free instead of many sets (for each input dimension) [69] which also significantly reduces the memory requirements of the model. Furthermore, each convolutional layer is usually followed by a pooling layer which further reduces the

output of the layer and helps to make the representation invariant to small shifts. In the case of regression of hyperspectral data the use of 1D nets is recommended, the application of 2D nets goes beyond the scope of this work. The application of a 1D CNN on spectral data to estimate chl-a is presented in [70]. Other research using CNNs in the framework of spectral remote sensing of water quality can be found in [71, 72].

CHAPTER 3

Related Work and Challenges

Remote sensing of waters in general has its origins in the 1960s [73, 74, 75, 13] and was initially used primarily in the context of ocean exploration. Methods were invented by the oceanographer community initially and have been transferred to inland water applications especially in the last three decades [13]. While a number of studies use multispectral satellite data for remote sensing of inland waters [46, 76, 77, 78], there are now also hyperspctral satellites [79, 17, 19] and airborne campaigns [80, 81, 20, 82].

As sensors become smaller, the application of UAVs becomes more attractive [28, 83, 57, 84] to acquire remote sensing data of inland water bodies to better understand the processes therein or to improve their mangagement. Compared to traditional methods such as remote sensing using satellites and airplanes, the low costs for the setup and operation of UAV borne sensor systems are a major advantage. Also, UAVs can be operated below the cloud cover while in regions with frequent cloud cover satellites often cannot provide data for weeks.

In the following, current research in the field of remote sensing of water quality parameters using UAV-mounted systems is discussed and challenges are presented.

3.1 Remote Sensing of Water with UAVs

Optical remote sensing using UAVs can make use of different sensor technologies. On the one hand, there are multispectral sensors with usually less than 10 spectral bands [85] and on the other hand hyperspectral sensors with usually more than 100 spectral bands [86], which cover e.g. the visible and near infrared range and are usually used for remote sensing of water quality parameters.

Hyperspectral sensors can generally be subdivided into point spectrometers, line scanners and imaging sensors [27]. While point spectrometers have a very high spectral resolution, they do not provide spatial information, which must be generated e.g. by appropriate

flight planning in UAV campaigns [87]. Line scanners, on the other hand, usually offer high spectral and high spatial resolution along one dimension. An areal acquisition of data with two spatial and the spectral dimension is only possible with imaging sensors. These use either fixed optical components to enable a snapshot system [88], or like fabry perot interferometer (FPI) based systems a scanning of the spectral dimension to generate the hyperspectral cubes [89]. FPI based cameras can achieve high spectral and spatial resolution, but individual geometric correction is required for all channels, since the sequential scanning of bands with the sensor in motion causes geometric offsets [90]. Snapshot systems usually have fixed channels with lower spectral and spatial resolutions, but allow the acquisition of full hyperspectral cubes at high frame rates. In contrast to the use of point spectrometers and line scanners, hyperspectral imaging cameras allow the use of redundancy along the flight line to create parameter maps.

In remote sensing of water quality parameters, multispectral cameras [91, 84] and partly hyperspetral cameras [92, 93] integrated on UAVs are increasingly used due to smaller dimensions and decreasing costs in comparison to airborne systems and campaigns to study e.g. the spatial distribution of pyhtoplankton. Also, measurement campaigns with compact UAVs can generally be planned and implemented quickly, as neither special infrastructure for takeoff and landing nor a professional pilot are required. In addition to a flexible data acquisition in terms of time and space, the ability to quickly switch between different sensor systems on the UAV (e.g. active and passive sensors) is also an advantage.

Especially hyperspectral sensors allow the use for various applications due to the wide spectral range covered and provide the necessary spectral properties even for the remote sensing of complex inland waters. Good results can also be obtained with multispectral sensors, but here not only the bandwidth of the channels but their number and especially the position of the channels in the spectrum is crucial, for example to cover different phytoplankton classes [94, 52].

The estimation of parameters is often based on models trained with the help of fine tuned band ratio models using local reference samples. This usually results in very high accuracies for single water bodies but the models are not transferable to others. In contrast, analytical models are more general but they usually need good initial values and probably further in-situ measurements for inversion. Therefore, they do not yet seem to play a role in the area of UAV borne remote sensing of water quality. However, a promising approach is the use of simulated data using these analytical models to obtain generic machine learning models for parameter estimation [52].

In general, UAV are already used for remote sensing of CDOM [95, 57], TSS [92, 96, 84] and chl-a [29, 87, 93, 97]. There, band ratios [91], partial least squares regression [28, 57] or neural networks [67] are used to estimate the parameters, for example.

3.2 Challenges and Limitations

Even though there are now numerous studies that deal with compact hyperspectral sensors on UAVs in the context of different research fields and especially parts of the research of [57] are similar to this work, there are still existing challenges and limitations. While the sensors get smaller and cheaper they usually suffer e.g. from less stable spectral characteristics and the small UAVs are more affected by environmental influences as wind gusts which can complicate the processing of the data. In the following, challenges which need to be considered in this work are presented.

UAV

Especially with vertical launch multirotor UAVs, the flight duration (mostly below 30 min) and thus the maximum range is strongly limited [98]. Fixed wing UAVs, on the other hand, can cover long distances (flight duration over 1 h), but require a larger flat area for takeoff and landing. In addition, on these systems the camera is usually not stabilized by a gimbal which complicates the georeferencing of the images. Another restriction for the operation of UAVs are also country-specific laws and regulations for the use of UAVs, whereby the use, for example, in nature reserves or in the vicinity of infrastructure is limited or not possible at all [99]. Finally, even though a lot of UAVs are now available and easy to use, the operation of customized UAVs require experienced operators and technicians for maintenance.

Sensor Calibration

When setting up the systems, care must be taken to ensure an appropriate calibration of the sensors, especially when using an additional spectrometer for irradiance measurement [100, 57]. Also checking of the calibration parameters for stability at regular time intervals is recommended. Especially for the comparison of spectral data with different sensors and the combination of different sensor types, calibration is indispensable. In the context of remote sensing of water quality parameters, for example, it was shown in [101] that insufficient radiometric calibration of a hyperspectral camera has non-negligible effects on the estimated parameters. Fig. 3.1 shows the effect of varying wavelength scales between the individual pixels of a hyperspectral camera. Clearly visible are undulation patterns in the data of estimated turbidity (mid column) using the hyperspectral images caused by the missing wavelength calibration. After an pixel individual calibration of the wavelength scales, these effects are eliminated (right column).

Geocoding

While most remote sensing applications have sufficient features in the image data to generate mosaics using feature based structure from motion algorithms, the water surface is too

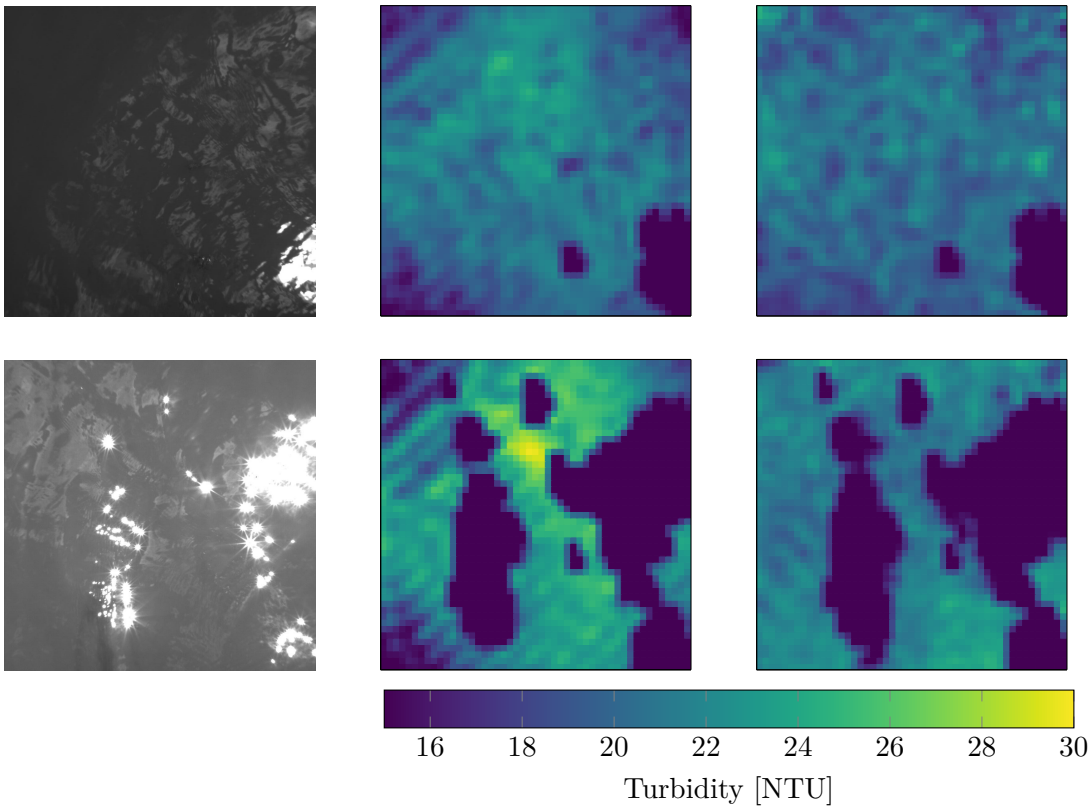

Figure (3.1) Effect of an uncalibrated wavelength scale of a hyperspectral camera on the parameter estimation. The left column shows two panchromatic images captured with the hyperspectral camera close to the water surface. The mid column shows the estimated turbidity in this area before wavelength calibration. After the pixel individual wavelength calibration the systematic effects visible as undulation patterns are eliminated (right column). Figure after [101].

homogeneous or existing features (i.e. waves) too variable to apply automated image-based algorithms [84]. Therefore, remote sensing of large water surfaces with UAVs depends on accurate pose parameters of the used sensors.

Atmosphere, Clouds and Surface Effects

While satellite data cannot do without the correction of atmospheric influences, these are usually considered negligible for UAV data in the literature [32, 102] and are therefore not considered in detail in this work.

A challenge in the remote sensing of water quality parameters are reflections at the water surface [103, 95]. These are, on the one hand the total reflection of sunlight (sun glint) depending on the position of the sun, the viewing angle on the water and possible variations by waves, and on the other hand the reflection of the sky (sky glint). To correct for these effects, point spectrometer systems usually use at least one additional spectrometer to

measure the sky radiance in the area of the sky that is reflected from the water surface [104]. In conjunction with numerical simulations, which include the motion of the water surface, a correction can be determined [50]. While mobile or fixed point spectrometers allow the use of an optimal geometric configuration different from nadir with multiple spectrometers, this is usually not possible with UAV borne imaging systems. Only [29] presents a system that uses two multispectral cameras on a UAV to additionally measure the sky radiance synchronously.

An alternative is presented in [105] where sky radiance is reduced by using in-situ measurements of the water leaving radiance using the multispectral camera inside a black tube. As the camera needs to be detached from the UAV or another sensor is needed, this method ist not applicable with our system presented in Chap. 4.

Analytical models try to simulate and invert sun and sky glint, but this requires, among other things, expert knowledge of the user and usually further in-situ measurements [103], making an automated correction difficult. The application and analysis of such an analytical model to reduce water surface effects is described in [106] and [104] using simulated and station based point spectrometer data.

Using polarization filters is another possibility to reduce glint [107]. Studies with imaging spectrometers at a fixed station show that the application of polarization filters can achieve similar results as the analytical methods mentioned [108]. At the same time, however, further challenges are pointed out depending on the optical components used in the sensor and further influences with moving sensors on UAVs. An application of hyperspectral cameras with polarization filters on UAV for the reduction of glint is not known.

Also, a variable cloud cover further complicates the processing of the spectral data as the irradiance changes continuously and cloud shadows on the water surface add even more challenges to the task of parameter estimation from hyperspectral data. In [109] an analytical model is used to estimate parameters under changing cloud conditions. However, specific parameters for absorbance and scattering have been measured in-situ and are introduced to the model (e.g. the specific backscattering coefficient of TSM), whereas parameters for sky reflectance and cloud cover where fitted during the inversion of the model. Overall, the approach provides promising results, but there are larger deviations from reference values (approx. 30 %) when estimating parameters, and here, too, an operator with sufficient background knowledge must operate the software.

Bottom Reflectance

Depending on the water depth and the attenuation of light in the water column, the bottom can affect the measured spectrum at the sensor (cf. Fig. 2.4b) which was also noted as a problem in [57]. The influence on the spectrum then depends on the type and constitution of the bottom whereas pure sand would mainly affect e.g. the estimation of total suspended solids. The presence of plants in contrast would have an influence on the estimation of

phytoplankton parameters. Therefore, the water depth should be available as measured bathymetry or the estimation methods should be chosen in a way that they can handle low water depths in the estimation process.

3.3 Summary

Due to the fast progressing development of compact UAVs and lightweight sensor systems, they become more and more attractive for remote sensing tasks in general but also for remote sensing of water quality parameters in particular. Especially, the now available compact hyperspectral cameras provide the necessary high spectral resolution for remote sensing of water quality parameters. However, before setting up a system, the advantages and disadvantages of each camera technology should be considered in the context of the application. Crucial for the quality of the results is a precise calibration of the sensors. Especially the wavelength scale of the single pixels of a camera should be checked and calibrated if necessary. For remote sensing of water bodies, an accurate measurement of the camera pose or its stabilization using a gimbal is necessary to simplify the georeferencing of the data as much as possible, since feature based methods are usually not applicable over water. The acquired hyperspectral images of water bodies are partly influenced by water surface effects like sun glint, which makes the evaluation more difficult. The use of redundancy can help to improve the final parameter maps. For this purpose, suitable methods for the creation of parameter mosaics from overlapping hyperspectral images have to be developed.

CHAPTER 4

Sensor System and Calibration Methods

The multi modal sensor system consists of a hyperspectral camera, an irradiance spectrometer, a thermal camera and an RGB camera (see Fig. 4.1 and Tab. 4.1). All sensors are integrated on a coaxial octocopter with a total weight of less than 10 kg (see Fig. 4.2). The imaging sensors are mounted on a two axis gimbal to maintain a nadir orientation of the sensors during the flight. First, this chapter presents the sensors and their specifications, then the methods to calibrate the spectral sensors are explained (see Sect. 4.2). To calibrate the spectral sensors, standard methods are used and adapted to the sensors, especially for the hyperspectral camera. The results of the calibration of the spectrometer, the hyperspectral camera, and their cross calibration are shown in Sect. 4.3. As the copter and the sensor system share different time scales, a data driven method for synchronizing was developed that enables the inclination correction of the irradiance measurements (Sect. 4.4) which is inevitable to calculate the remote sensing ratio which is the foundation for the estimation of water quality parameters in this work. Sect. 4.5 provides a short summary and embeds the results into the context of related work.

(a) (b) (c) (d)

Figure (4.1) Used sensors from left to right: hypserspectral camera (Cubert S185), irradiance spectrometer (Broadcom Qmini), thermal camera (Flir Tau2), RGB camera (Mapir Survey 3).

Figure (4.2) Integrated sensor system mounted to the UAV. The two axis gimbal maintains the desired viewing angle of the cameras during the flight. The irradiance spectrometer is mounted on a pole next to the GPS antenna.

Table (4.1) Sensor specifications of the hyperspectral camera S185, the irradiance spectrometer Qmini and the thermal camera Tau 2 as given by the manufacturers.

	S185	Qmini	Tau 2
Wavelength in µm	0.450 - 0.95	0.225 - 1.0	7.5 - 13.5
Channels	125	2500	1
Resolution in nm	8 @ 532	1.5	-
Sampling in nm	4	0.31	-
Weight in g	490	60	100
Sensorsize	50x50	1	640x512
PAN in pixel	1000x1000	-	-
Sensor	CCD	CCD	Micro Bolometer
FOV in deg	26x26	- *	44x36
A/D converter in bit	12	16	-

*cosine corrector

4.1 Sensors

The hyperspectral camera S185 from Cubert is used to map the water surface to estimate water quality parameters like turbidity. In combination with the upward looking spectrometer Qmini from Broadcom it is possible to measure the changing downwelling irradiance during the flight. The thermal camera (Flir Tau 2) is used to map the temperature of the water surface. To get more visual information about the conditions during the flight, the Survey3 RGB camera from MAPIR is integrated into the system. It follows first the description of the spectrometer and then the hyperspectral camera and thermal camera.

Spectrometer

The upward looking spectrometer (Qmini, Broadcom Inc.) is used to measure the downwelling irradiance in the range from 225 nm to 1000 nm with 2500 channels. The spectrometer uses a linear 16 bit CCD sensor array, whereas the typical spectral resolution (FWHM) is specified as 1.5 nm. To measure the irradiance, the spectrometer is equipped with a cosine collector, which is a diffuser to collect the signal from the upper hemisphere before entering the entrance slit of the device. Using the irradiance measurements during the flight allows the dynamic calculation of reflectance values adjusted to the current conditions.

Hyperspectral Camera

Compared to the well established pushbroom, fabry perrot interferometer and filter based sensors, the used hyperspectral camera (S185, Cubert GmbH) features snapshot acquisition of hyperspectral images (see [27]). It provides a 50 x 50 pixel data cube, where each pixel has 137 channels in the range from 450 nm to 998 nm with a spectral sampling of 4 nm. However, the manufacturer recommends only using the first 125 channels. Inside the camera the three dimensional problem of a hyperspectral cube is projected on a two dimensional CCD sensor. Simply said, the incoming light is focused on an optical element, which unfolds the spectrum at the 50 x 50 points to its components which are projected on different areas of the sensor array. The read out of the raw data cube already contains the pre calculated hyperspectral data, whereat the raw two dimensional data is proprietary and not used in this work. The spectral resolution decreases significantly from short to long wavelengths (see Fig. 4.3). Beside the hyperspectral data, the camera features an additional coregistrated high resolution panchromatic channel (1000 x 1000 pixel). The field of view of approximately 26° facilitates a ground sampling distance (GSD) of about 1 m at a flight height of 100 m above ground level (AGL). Under sunny conditions the typical integration time over water is 12 ms increasing to more than 100 ms under overcast sky. First use cases and investigations of this sensor and possible issues and challenges that could occur using this type of sensor are presented in e.g. [110, 111, 31, 112, 101].

Especially [113] is relevant in the context of this thesis. They integrate the same hyperspectral camera as used here and a spectrometer on a UAV which uses a method similar to the one presented in this thesis to correct the systematic tilting effects of the irradiance spectrometer. Their investigation of the spectral resolution reveals a worse resolution, especially for longer wavelengths compared to the specifications provided by the manufacturer. In contrast to this work, the effect of nonlinearity was only investigated, instead of a calibration they only use the linear range of the sensor.

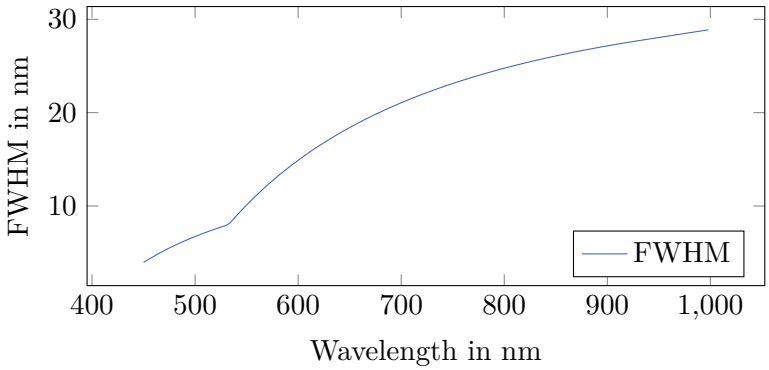

Figure (4.3) The spectral resolution for each channel of the hyperspectral camera is given as FWHM in nm by the manufacturer. The spectral sampling is 4 nm starting at 450 nm.

Thermal Camera

The thermal infrared camera Tau 2 from Flir has an uncooled micro bolometer array with 640 x 512 pixels and is used to measure the water surface temperature. At a flight height of 100 m the GSD is about 13 cm. To measure the temperature, the spectral band from 7.5 µm to 13.5 µm is used. The data is recorded using the ThermalCapture 2.0 from TeAx and has a specified resolution of 0.04 K. As various studies using uncooled micro bolometer cameras show effects overlaying the signal (e.g. [114]) it is expected that these effects also occur in the data. Mainly there are two effects, first, a general drift in temperature and second a vignette like overlay of the data. These effects show temporal variabilities and have a number of possible causes, as spatiotemporal variations of the temperature of the lens, the housing, and the sensor array (see [115, 116, 114]). Due to the temporal variability of the effects, laboratory calibration is impossible. Therefore, a data driven correction approach was developed which is applied during the processing of the data (see Chap. 6).

4.2 Calibration Methods for Spectral Sensors

Almost all available sensors have individual characteristics affecting the signal to be measured depending e.g. on temperature and optical elements. The modeling and correction of these characteristics are necessary to measure reliable values and are inevitable if different sensors are combined in a multi modal sensor system like the presented one. In this work, the calibration is crucial especially to calculate reliable reflectance values as the ratio of radiance and irradiance, measured by different sensors (see Sect. 2.2). To calculate the reflectance values from two different sensors, either an absolute calibration of each sensor or a cross calibration between the sensors is necessary. In the following, calibration methods for the spectral sensors used in this work and results are described in detail. The methods for geometrical calibration are omitted, and it is referred to the well established methods in

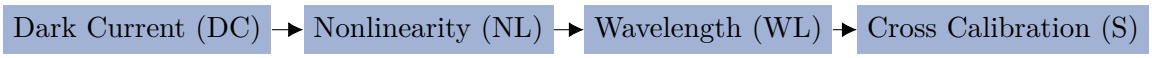

Figure (4.4) The calibration process aims to individually characterize the sensors (DC, NL, WL) and to calculate the cross calibration factor (S) between them. The cross calibrated sensors enable the direct measurement of the remote sensing ratio.

literature and software (e.g. [117]). The geometrical calibration of the cameras was carried out using an asymmetric circles pattern and the camera calibrator app of MATLAB®.

4.2.1 General Methods

First, general methods to calibrate spectral sensors are presented as they are applied to the irradiance spectrometer, which measures one spectrum at a time. After this, the extensions of these methods to calibrate the hyperspectral camera are illustrated (see Sect. 4.2.2) which synchronously measures multiple spectra and also has further optical elements that needs to be considered. Finally, the cross calibration of these two sensor types is described in Sect. 4.2.3.

The calibration of spectral sensors (see Fig. 4.4) starts by modeling the dark current (DC) which depends on the integration time and the temperature of the sensor array. The nonlinearity (NL) is a sensor specific deviation from a linear behavior of the incoming signal. As the next step, the wavelength (WL) calibration ensures that the correct wavelength is assigned to each channel. Instead of an absolute calibration of the radiance and irradiance values, the last calibration step is the cross calibration of the irradiance spectrometer and the hyperspectral camera. Whereby the individual spectral resolution of the two sensors is also taken into account. The DC, NL and WL calibration were carried out for each spectral sensor in a lab using professional equipment.

Dark Current

Even when no radiation enters the detector, a small electric current can be measured, which is called dark current (DC). It consists of fixed patterns and temporal noise. The fixed patterns can be measured by averaging multiple measurements when no photons enter the device. These fixed patterns can be characterized by a model depending on the integration time and temperature of the sensor. A dataset to model the dark current must cover the integration times and sensor temperatures which are expected to occur in the planned measurement setups. The sensor should be heated and cooled down slowly while acquiring the data to check for different behavior between heating and cooling. The DC correction can be written as follows:

$$Y'(k) = Y(k) - DC(\tau,T) \quad , \tag{4.1}$$

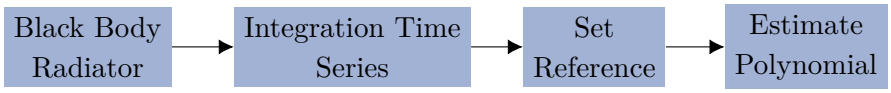

Figure (4.5) Nonlinearity calibration of a CCD sensor using a black body radiator (e.g. a stabilized halogen lamp). A linear reference is set to the not linearly changing measurements of an integration time series. The deviation is modeled by a polynomial.

where τ is integration time, T is the temperature of the sensor array and k is the channel of the measured signal Y. If there is no temperature sensor inside the device, the behavior of the sensor must be investigated for its characteristics while changing integration time and temperature. In this case, dark current measurements should be carried out as often as possible during measurements, especially when the temperature of the sensor changes or the integration time is adjusted.

Nonlinearity

The deviation of the sensor readout to the expected behavior of a linear changing incoming signal is called nonlinearity. This effect can be observed by either changing the incoming signal with known reference values or changing the integration time while keeping the incoming signal stable.
In this work, the latter approach is used. The process to model the nonlinearity (see Fig. 4.5) of a sensor starts by acquiring a dataset of a luminance standard with changing integration times of the sensor. Then a representative channel k is chosen which shows very low and high values over a wide range of integration times. Mean values of multiple acquired measurements for each integration time τ_i should be used and must be DC corrected to retrieve $Y'(k,\tau_i)$. If $Y'(k,\tau_i)$ does not change linearly when changing the integration time, an arbitrary linear polynomial $Q'(k,\tau_i)$ must be set as a reference. The ratio $P'(k,\tau_i) = Y'(k,\tau_i)/Q'(k,\tau_i)$ fitted to $Y'(k,\tau_i)$ represents the model of the nonlinearity $NL(Y'_i(k))$ of the sensor:

$$NL(Y') = fit(Y'(k,\tau_i),P'(k,\tau_i)) \quad . \tag{4.2}$$

The nonlinearity can usually be estimated as a second degree polynomial representative for all channels. A correction of nonlinearity depends only on the DC corrected measured signal and the corrected signal should be normalized by the integration time τ_i:

$$Y''(k) = Y'(k)NL(Y'(k))/\tau_i \quad . \tag{4.3}$$

Wavelength

The calibration of the wavelength scale allocates the corresponding wavelength in nm to each spectral channel of the sensor. This calibration step can be done using a monochromator or wavelength calibration lamps like mercury lamps which have spectral lines with known

Figure (4.6) Wavelength calibration using the measured spectra of traceable wavelength standards. The sub channel positions of peaks are estimated by polynomial fits. The corresponding pairs of sub channel position and wavelength are used to fit an appropriate polynomial.

positions on the wavelength scale.
The distance between the lines should be appropriate to the spectral resolution of the sensor. Otherwise, the spectral resolution must be taken into account while calibrating. The spectral lines of the calibration standards are measured as peaks with the spectrometer, and their maxima are fitted with an appropriate polynomial to achieve a sub channel precision of the peak position. A polynomial that fits the identified peak positions to the traceable wavelength allows the assignment of the corresponding wavelength λ to each channel k.

$$Y''(\lambda) = WL(Y''(k),k) \tag{4.4}$$

Finally, using an appropriate interpolation method allows an equidistant sampling of the spectrum which might be inevitable for further processing.

4.2.2 Camera specific Calibration

Calibrating the used hyperspectral camera requires some additional considerations and steps. First, each of the camera's pixels must be treated as a single spectrometer. Second, the spectral resolution of the camera must be considered when using spectral calibration lamps to calibrate the wavelength scale and for cross calibration with other spectral sensors. Third, there are more optical components inside the camera compared to the spectrometer which could affect the measurement, especially vignetting effects that are expected and must be corrected. To perform the calibration steps for all sensor elements it is necessary to use homogeneously illuminated surfaces with approximately Lambertian characteristics e.g. luminance standards, integrating spheres or panels with known reflectance characteristics.

Resampling of Spectra

As the camera has a decreasing spectral resolution with increasing wavelength, this must be taken into account while calibrating the wavelength where adjacent spectral peaks result in a superimposed signal. Especially, to perform the cross calibration of the camera and spectrometer, the resampling of the spectra of the irradiance spectrometer is inevitable as their spectral resolutions differ clearly from each other. The resampling method described in the following is also published in [101] and based on the approach presented in [118].

The spectral resolution is e.g. given by the manufacturer as the full width at half maximum (FWHM) for each channel k. The spectral resolution of the original spectrum is $FWHM_o$,

and the spectral resolution of the resampled spectrum is $FWHM_d$. These values are used to calculate the σ_k of a Gaussian kernel $\mathcal{N}(\lambda_k - \lambda', \sigma_k^2)$ (see Equation 4.5). Equation 4.6 represents the resampling process. For each channel k a new value $Y''_{d,k}$ is computed by integration of the convolution of a Gaussian kernel $\mathcal{N}(\lambda_k - \lambda', \sigma_k^2)$ with the original spectrum $Y''_{o,k}$ in the interval of $\lambda_k \pm 3\,\sigma_\mathrm{k}$:

$$\sigma_k = \left(2\sqrt{2\ln(2)}\right)^{-1} \sqrt{FWHM_{d,k}^2 - FWHM_{o,k}^2} \quad , \tag{4.5}$$

$$Y''_{d,k}(\lambda, FWHM_d) = \int_{\lambda_k - 3\sigma_k}^{\lambda_k + 3\sigma_k} Y''_{o,k}(\lambda', FWHM_o) * \mathcal{N}(\lambda_k - \lambda', \sigma_k^2)\,\mathrm{d}\lambda' \quad . \tag{4.6}$$

4.2.3 Cross Calibration

Instead of an absolute calibration of the radiance or irradiance values to traceable SI-units it is sufficient in this work to calculate the calibration factor between the two spectral sensors. This cross calibration is necessary to calculate the remote sensing ratio (see Sect. 2.2) using the measurements of the hyperspectral camera and the spectrometer. The calibration was performed outdoors using an optimized setup under sunny conditions (see Fig. 4.7). Both sensors were mounted on a matt black stand and oriented to reduce the effects of reflections and stray light on the measurements. The spectrometer was mounted on the top and aligned horizontally. The hyperspectral camera looked nadir on a plate with known reflectance characteristics. The data was acquired synchronously, and the calibrated mean spectra of the camera Y''_C and the spectrometer Y''_Q of multiple measurements were calculated. The measurements Y''_Q are then resampled to the spectral resolution of the camera. The cross calibration factor is calculated per channel as follows:

$$S_{QC}(\lambda) = Y''_C(\lambda) / Y''_{Q_d}(\lambda) \quad . \tag{4.7}$$

4.3 Sensor Calibration Results

This section presents the results of the investigation and calibration of the sensor system with a focus on the spectral sensors. It starts with the individual steps for the spectrometer and the camera. Then, the results of the cross calibration of both sensors are shown.

4.3.1 Spectrometer

The sensor specific calibration was performed in a lab without changing the assembly of the spectrometer between the individual measurements. It follows first the investigation

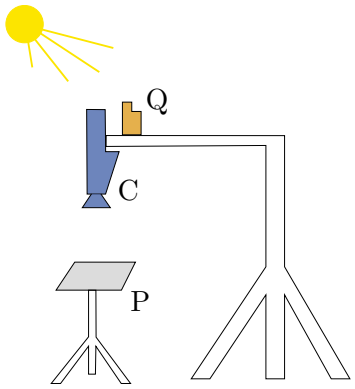

Figure (4.7) Schematic figure of the cross calibration. The sensors are mounted on a stand. The irradiance spectrometer (Q) is looking upwards, and the hyperspectral camera (C) is looking downwards on a reference panel (P) with known spectral characteristics. The sensors acquire synchronized data of the downwelling solar irradiance outdoors under sunny conditions.

and modeling of DC. After this, the NL was characterized, and finally the WL scale was calibrated.

Dark Current Calibration

The data for this calibration task was acquired by closing the entrance slit of the spectrometer and heating the device using a thermal radiation source. Measurements from 28 °C to 45 °C sensor array temperature and integration time settings of 0.01 s, 0.25 s, 0.5 s, 1 s have been used to investigate and model the DC of the Qmini spectrometer (see upper left in Fig. 4.9). For typically used integration times of less than 0.02 s, the DC values are normally distributed. Higher values show a positive skew which should be taken into account, if necessary (see Fig. 4.8).
DC depends on two variables, the temperature T of the sensor array and the integration time τ. Therefore, the chosen model is a polynomial surface, whereas a degree of three for each variable fits best for this sensor. The fitted polynomial of the dataset acquired while heating the device is shown in Fig. 4.9a.
Measurements of heating and cooling the sensor have been acquired. The difference between the polynomials between heating and cooling is shown in Fig. 4.9b. In the expected temperature range from 30 °C to 35 °C and used integration time of less than 0.02 s (see red box in Fig. 4.9b) the difference between heating and cooling is small, and the mean of both polynomials is used for later DC correction.

Nonlinearity Calibration

To perform the nonlinearity calibration, a series of measurements of the luminance standard LMT-LN3 were acquired, DC corrected, and measurements with identical integration times

(a) Integration time: 0.01 s. **(b)** Integration time: 1 s.

Figure (4.8) Histograms representing the DC of the irradiance spectrometer at 30 °C for two different exposure times. The distribution is changing to a positive skew for long integration times. The Histograms show values of four measurements for all pixels.

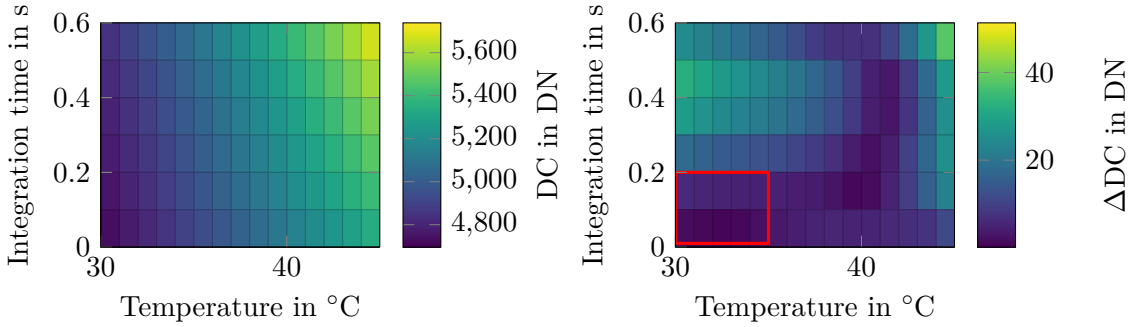

(a) **(b)**

Figure (4.9) Results of the DC calibration of the irradiance spectrometer. Measurements have been acquired while heating and cooling the device. (a) The polynomial fit of dark current depends on temperature and integration time. (b) Delta of fitted dark current between heating and cooling. The red box represents the value range in which the spectrometer is operated during the field campaigns.

averaged. The integration time was varied in thirteen steps from 0.01 s to 0.6 s. For further processing, the spectra with values $Y'_k > 5000$ for channel $k = 1300$ were chosen (see upper left of Fig. 4.10). This reduces the dataset to eight measurements with integration times from 0.1 s to 0.6 s. The first few hundred channels show only small and noisy values caused by the light source, which emits no radiation in this wavelength range. After normalizing the spectra by their individual integration time the plot in the upper right of Fig. 4.10 shows deviations from the desired overlap of all normalized spectra which is caused by the nonlinearity characteristics of the sensor.

To model the nonlinearity the first step is to choose an arbitrary linear reference $Q'(\tau) = 58333.33\,\tau$ to the measured $Y'_k(\tau)$. In the next step, this linear polynomial is evaluated at the corresponding integration times of the measurements. Finally a polynomial of degree two is fitted to $Y'_k(\tau)$ and $Z'(\tau) = Y'_k(\tau)/Q'(\tau)$. Fig. 4.10b visualizes this step. The dots represent the factors $Z'(\tau)$ and the red line is the fitted polynomial, which is the model of

the nonlinearity:

$$NL(Y') = 0.9169 + 8.2517 \cdot 10^{-6}\, Y' - 1.4334 \cdot 10^{-10}\, Y'^2 \quad . \tag{4.8}$$

The figures 4.10c and 4.10d show all spectra normalized by integration time and each divided by the mean spectrum of all eight measurements before and after applying the nonlinearity correction. The X-axis is limited to the range where the sensor is sensitive and the incoming signal is high to prevent analyzing other sensor specific effects. In Fig. 4.10c, systematic sensor characteristics are visible, in Fig. 4.10d, the characteristics are corrected, and only noise of 2% is remaining.

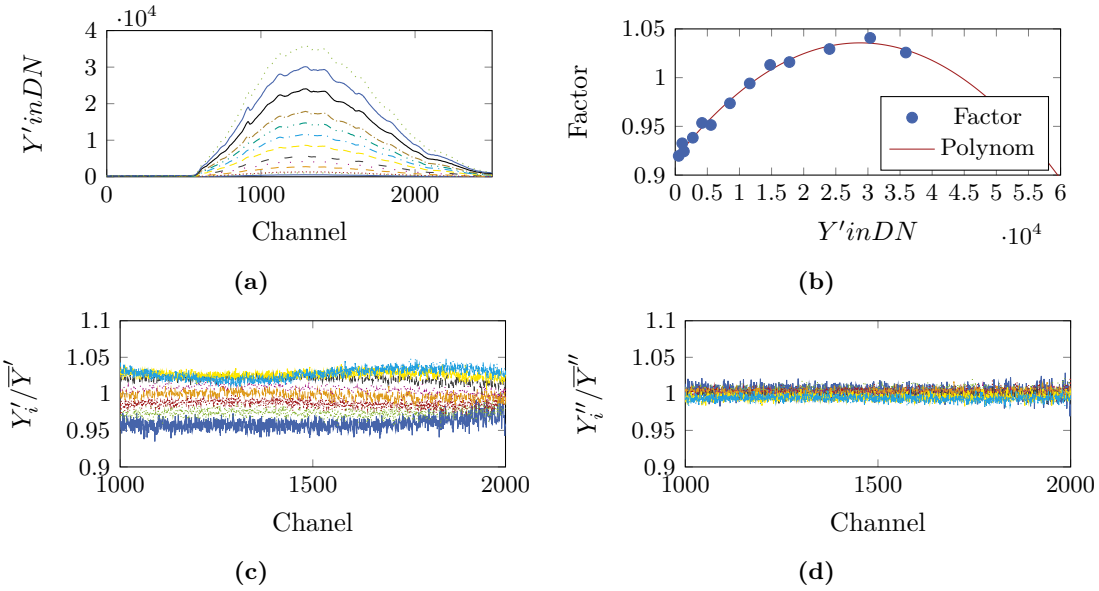

Figure (4.10) Nonlinearity calibration of the irradiance spectrometer using measurements of a luminance standard. The DC corrected measured spectra of an integration time series (a) are used to calculate the nonlinearity factors for multiple discrete steps (dots in b) and are fitted by a polynomial of degree two (red line in b). The lower two figures show the effect of applying the NL calibration in the range from channel 1000 to 2000. While in (c), the channel individual factor of spectra with different integration times Y_i' (each normalized by integration time) divided by the mean of all spectra $\overline{Y}_i'$ shows variations of up to 5 % before calibration and varies over the range of channels, these effects are reduced after calibration (d).

Wavelength Calibration

To calibrate the wavelength scale of the Qmini spectrometer, four different calibration lamps were used (Argon, Ar; Mercury, Hg; Neon, Ne; Xenon, Xe). These lamps emit distinct spectral lines in a wide range. It is sufficient to calibrate the wavelength in the operating range of the hyperspectral camera. Therefore, only relevant peaks in the range from 400 nm to 1000 nm, which are as evenly distributed as possible were chosen (see Fig. 4.11b). Starting with Hg in the blue region, Ar and Ne in the red region, and finally, lines in

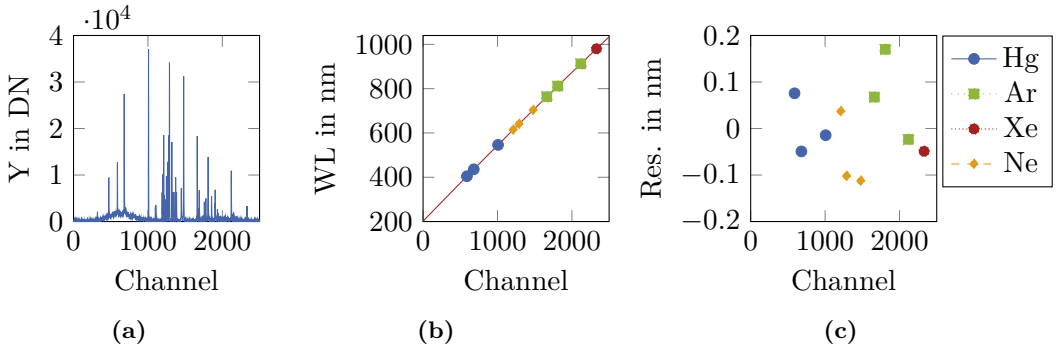

Figure (4.11) Wavelength calibration of the irradiance spectrometer. The first figure (a) shows a combined spectrum from measurements of four different calibration lamps (Hg, Ar, Xe, Ne). The positions with subchannel position of selected peaks and their corresponding wavelengths are visualized in (b). The polynomial fit between channel and wavelength is marked as a red line. The last plot (c) shows the residuals of the polynomial fit.

the near infrared region of the Xe lamp. The combined spectrum of the four individually measured spectra is shown in Fig. 4.11a. The individual spectral peaks were fitted using a second degree polynomial. The position with sub channel accuracy is plotted against the corresponding wavelength of the peak in Fig. 4.11b. This relationship was fitted using a second degree polynomial (red line)

$$WL(k) = 201.487 + 0.348\,k - 6.022 \cdot 10^6\,k^2 \quad , \tag{4.9}$$

which is the model to calculate the wavelength (WL) of each channel k in nm. The residuals of the fit are visualized in the right plot and show deviations of less than 0.2 nm (see Fig. 4.11c).

4.3.2 Hyperspectral Camera

In the following, the investigation and calibration of the hyperspectral camera is presented. The DC could not be modeled due to a missing temperature sensor, it is therefore only investigated. Not all calibration steps could be performed individually for each pixel. Most plots are given for one representative pixel, and some investigations are visualized for all sensor elements to reveal spatial patterns.

Dark Current Analysis

The hyperspectral camera does not provide a temperature sensor, therefore, the DC could not be modeled, only investigated. For a first investigation, the camera was powered on and the lens was covered. Data acquisition with changing integration times started after

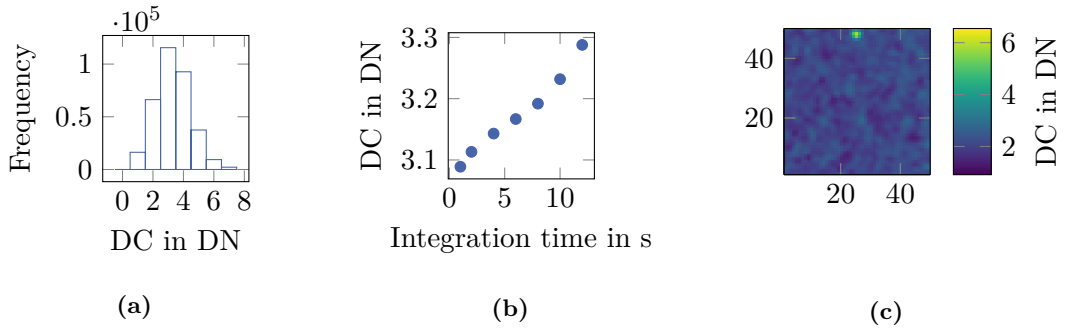

Figure (4.12) DC Investigation of the hyperspectral camera. The histogram of all pixels and channels with an integration time of 12 ms and a housing temperature of approximately 40 °C is shown in (a). The DC values are almost normally distributed, and a slightly increasing mean DC for increasing integration time is present (b). A mean image of 10 acquisitions of channel 35 at 33 °C is shown in (c). This is similar to other channels where some pixels have higher DC values than the average (visible at the upper image margin).

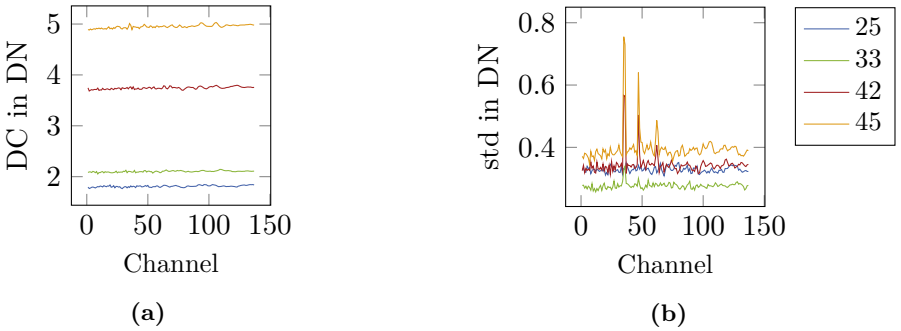

Figure (4.13) Statistics for each channel of mean images calculated from each ten measurements at different housing temperatures with each 10 ms integration time. Figure (a) reveals an increasing DC per channel with increasing temperature. The standard deviation per channel plotted in (b) indicates channels with biased pixels.

30 min. The second experiment aimed to investigate the temperature dependency of the DC. To perform these measurements, the camera was put into a closed black box, and a temperature sensor was attached to the outside of the housing.
The histogram for all pixels and channels of a single acquisition (cf. Fig. 4.12a) shows normally distributed values in all cases for changing integration time and temperature. With increasing integration time, the mean DC of all pixels and channels of 10 acquisitions for each integration time increases slightly (see Fig. 4.12b).
Analyzing the mean DC of each channel with changing temperature for a fixed integration time setting (10 ms) shows an increasing value (see Fig. 4.13a). Some channels show pixels with higher DC than the average (see Fig. 4.12c). These channels can be identified by a higher standard deviation (see Fig. 4.13b). This should be remembered if these effects are visible in further experiments. DC measurements during field campaigns always were in the range of 2 DN which is consistent with the analysis in the lab with a housing temperature

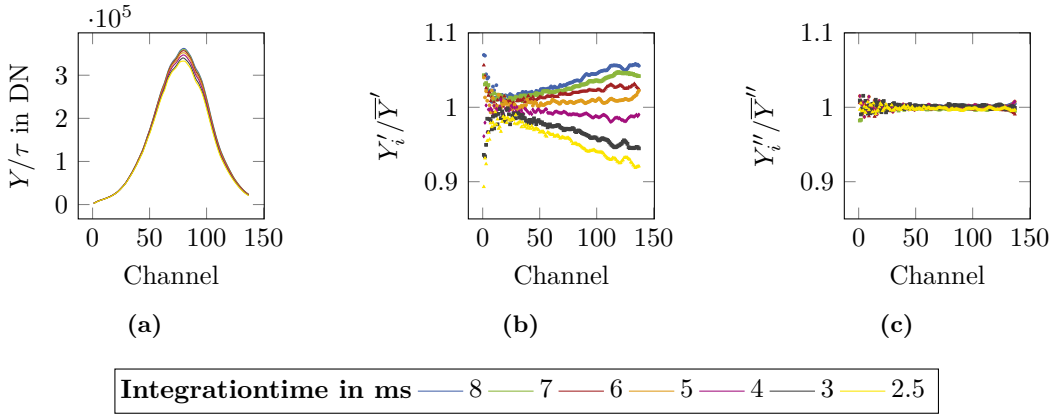

Figure (4.14) Nonliearity calibration of the hyperspectral camera using measurements of the LMT-LN3. An individual nonlinearity polynomial was estimated for each channel using a pixel in the image center. Subfigure (a) shows the raw spectra normalized by integration time. The normalized spectra divided by the mean spectrum of all normalized spectra are visualized in (b) where systematic deviations are visible. After applying the nonlinearity calibration, these systematic deviations are reduced (c).

of 30 °C. If no corresponding DC measurement is available to field measurements, a DC value of 2 could be used.

Nonlinearity Calibration

Like the nonlinearity calibration of the Qmini, this characterization step is based on a series of measurements of the luminance standard LMT-LN3. The nonlinearity calibration was performed using the spectra of one central pixel shown in Fig. 4.14a. These are the mean of each ten individual acquisitions, which are DC corrected.
As the estimated nonlinearity polynomial of one channel is not representative for all, the procedure was performed individually for each channel. First, k individual linear polynomial $Q'_k(\tau)$ were chosen as reference. Then, for each channel, a polynomial of degree two is fitted to $Y'_k(\tau)$ and $Z'_k(\tau) = Y'_k(\tau)/Q'_k(\tau)$ which gives k nonlinearity models $NL_k(Y')$.
The resulting factors of the polynomials are shown in Fig. 4.15. The quality of the fit varies between the channels, especially channels 1 to 40 show worse results than the others (see Fig. 4.15d). The results show that an individual correction for each channel produces good results, but further analysis revealed that this does not apply to other data. The correction that fits best to the applications of this work is presented in the evaluation paragraph of this section.

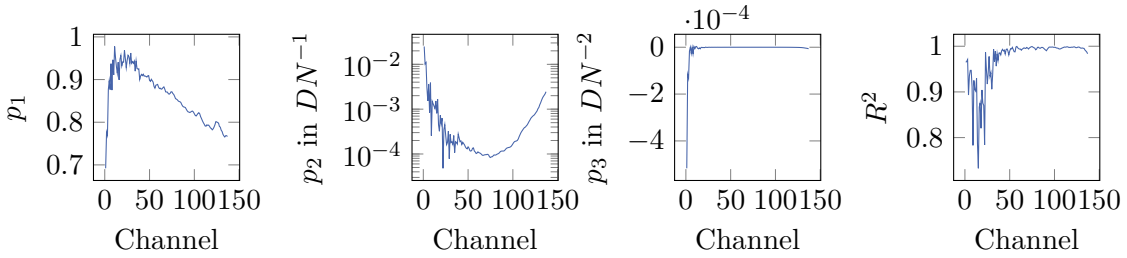

(a) p_1. **(b)** p_2. **(c)** p_3. **(d)** R^2.

Figure (4.15) For each channel of the hyperspectral camera, a polynomial of degree two was estimated to model the nonlinearity $NL = p1 + Y'p_2 + Y'^2p_3$. The figures represent the individual coefficients of each polynomial and the corresponding R^2.

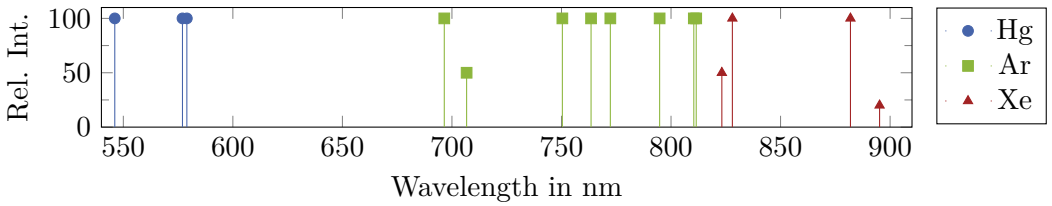

Figure (4.16) Position of relevant spectral lines of Ar, Hg, and Xe lamp which are used to calibrate the wavelength scale of the hyperspectral camera. The position and relative intensity of the lines are based on [119].

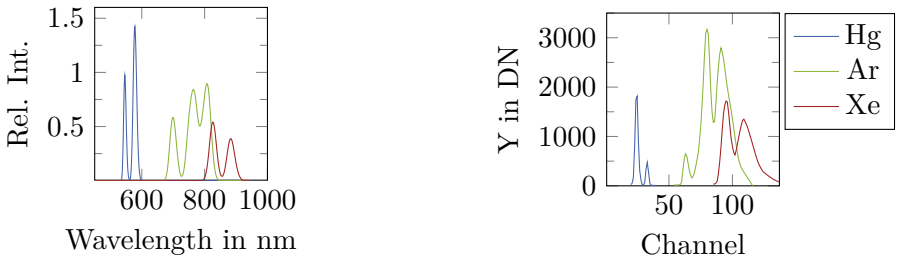

(a) **(b)**

Figure (4.17) Simulated (a) and measured (b) spectra of spectral calibration lamps. The figures show only peaks that are relevant to the calibration task (cf. Fig. 4.16). The simulated spectra use the reference peaks, which were resampled to the FWHM of the hyperspectral camera, also taking into account the relative intensity. A central pixel is chosen for visualization in (b).

Wavelength Calibration

The investigation of the wavelength scale of the hyperspectral camera was performed using the spectral peaks of an Ar, Hg, and Xe lamp. Relevant peaks with their relative intensity according to [119] are shown in Fig. 4.16. Due to the low and varying spectral resolution of the camera (see Fig. 4.3) it is necessary to resample these peaks to the resolution of the

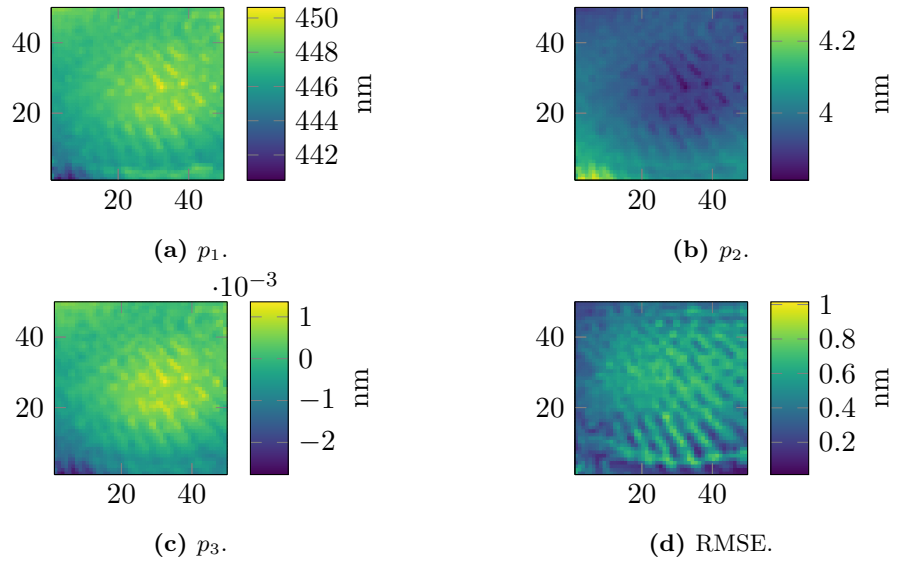

(a) p_1. **(b)** p_2. **(c)** p_3. **(d)** RMSE.

Figure (4.18) For each pixel the wavelength scale was estimated with a polynomial of degree two: $WL(k) = p_1 + kp_2 + k^2p_3$. The coefficients and RMSE for each pixel are visualized.

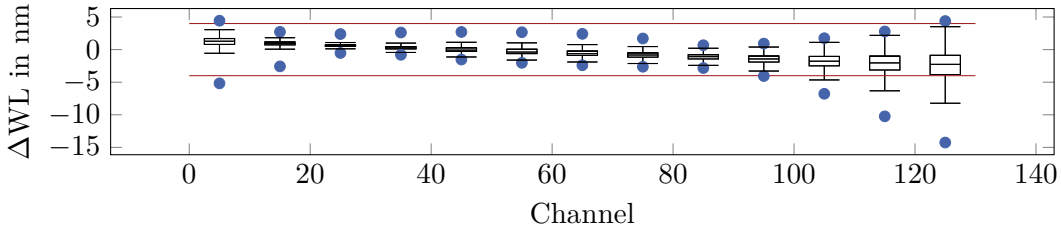

Figure (4.19) For each pixel of the hyperspectral camera, the wavelength scale was estimated with a polynomial of degree two. The box plots show deviations between the estimated scale and the scale specified by the manufacturer. Each box plot combines all pixels of ten channels. The bottom and top edges of the box indicate the 25th and 75th percentiles. A distance to the limits of the box of 1.5 times interquartile range is chosen to mark the whiskers. Values larger and smaller than the whiskers are treated as outliers. The blue dots mark only the maximum and minimum outliers. The horizontal red lines mark the spectral sampling of 4 nm. A slight trend, and especially for high and low channels, larger deviations and scattering are visible. Only the first 130 channels are visualized.

sensor before starting the calibration itself (see Fig. 4.17a). In Fig. 4.17b, the measured spectra for one central pixel are shown. The comparison of these two plots exhibits also some deviations, which may be caused by the spectral sensitivity of the sensor, inaccuracies of the spectral resolution model provided by the manufacturer, or the values for relative intensity of the spectral peaks.

The maxima of the resampled peaks are then fitted with a second degree polynomial to serve as the reference. Also, the positions of the maxima of the measured spectra are fitted with a second degree polynomial. This process is done for each pixel individually, and the

wavelength scales are fitted by a second degree polynomial. The parameters and RMSE of the pixel individual fits are shown in Fig. 4.18.
Fig. 4.19 shows the differences between the calibrated wavelengths and the wavelengths provided by the manufacturer for each channel as box plots. Each box represents all pixels of ten channels, starting with the first channel and ending with channel 130. A distance to the limits of the box of 1.5 times the interquartile range is chosen to mark the whiskers. Values larger and smaller than the whiskers are treated as outliers. Instead of visualizing all outliers, only maximum and minimum values are plotted. Two horizontal lines mark the 4 nm sampling of the sensor. Most of the deviations from the given wavelength scale are smaller than the spectral sampling and much smaller as the spectral resolution specified in Fig. 4.3. Larger deviations are only present at the edges of the wavelength range. This is mainly caused due to missing reference peaks and can not be evaluated. Therefore, the wavelength calibration should not be applied in this particular case, instead the parameters provided by the manufacturer are used. An improvement of the wavelength calibration can only be achieved by using a monochromator (cf. [31]), which can produce individual spectral peaks. This ensures that there is no overlapping of peaks in the measured spectrum due to the low spectral resolution of the HS camera.

Vignette Calibration and Residual Pattern

Measurements, which are DC and NL corrected show a strong vignetting effect of approximately 50 % from the image center to its margins caused by the optics of the camera (see Fig. 4.20a). This vignette can be estimated using measurements of a homogeneously illuminated Lambertian surface. In this work, the measurements were performed outdoors under perfect sunny conditions on a reference panel with known reflectance characteristics. To reduce the effects caused by the setup, multiple measurements with changing orientations of the camera and the reference panel were used and averaged. An exemplary result of an estimated vignette correcting factor for one channel is shown in Fig. 4.20b. As the reference, the mean value of each channel is chosen. The used polynomial is of degree four in u and v and individually fitted for each channel. After applying the calibration steps DC, NL and vignette correction, a residual pattern remainins which is similar for each channel. To reduce this pattern, it is estimated as a correcting factor individual for each pixel and channel (see Fig. 4.20c).

Evaluation

The calibration of the hyperspectral camera aims to obtain reliable measurements for each pixel, which are assigned to the correct wavelength and behave linearly to the signal. To evaluate the calibration steps with respect to the homogeneity of the hyperspectral images, an image of a white reference (outdoor, sunny conditions) was acquired, and the coefficient of variation (COV, [120]) was calculated for each channel after applying the individual

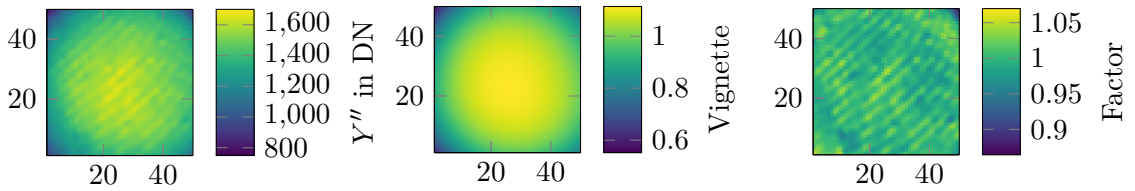

(a) Raw image. **(b)** Estimated vignette. **(c)** Residual pattern.

Figure (4.20) Vignette of the hyperspectral camera visualized for channel 80 (a). The vignette is modeled (b) for each channel individually as a factor where the reference is the mean value of each channel. A remaining residual pattern (c) of channel 80 after correction of the vignette is visualized as a factor where the reference is the mean of the channel.

calibration steps (see Fig. 4.21):

$$COV_k = \frac{1}{2500} \sum_{u=1}^{50} \sum_{v=1}^{50} \frac{\mu_{k,u,v}}{\sigma_{k,u,v}} \quad . \tag{4.10}$$

Here k corresponds to the channel and u,v to the pixel coordinates. The lower the COV, the more homogeneous the image of a homogeneously illuminated surface for each represented channel. First, the channel individual nonlinearity calibration (NLindiv) only slightly enhances the data compared to the raw image (Raw), but it is evident that the channel individual calibration does not provide good results for short wavelengths. Only for channel 60 and higher, the individual nonlinearity calibration provides good results. Therefore, an approach was chosen, which combines the individual calibration for channels starting from 60 with a constant model for the first 59 channels, which uses the model of channel 60. Applying the vignette calibration (Vig) after the nonlinearity calibration, the COV drops, as expected, to a much lower level. At this point, it is noticeable that applying the wavelength calibration (WL) does not improve the result, especially for long and short wavelengths where the COV increases. This affirms the decision not to apply a wavelength calibration other than the scale provided by the manufacturer. Finally, applying all calibration steps and the correction of the residual pattern further increases the homogeneity of each channel (Final).

4.3.3 Cross Calibration and Integrated Sensor System

The cross calibration was performed outdoors using two different reference panels, one with a specified reflectance of around 96 %, and one with around 51 %. The Qmini spectrometer simultaneously measured the downwelling irradiance (see Fig. 4.7) while capturing hyperspectral images of the reference targets with the camera. First, a series of measurements was acquired and averaged. The data was calibrated according to the previously described steps for each sensor. The spectra of the Qmini were resampled to the spectral resolution of the hyperspectral camera (see Fig. 4.22a). An exemplary spectrum of the hyperspectral camera is given in Fig. 4.22b. Using multiple acquisitions with different orientations of the

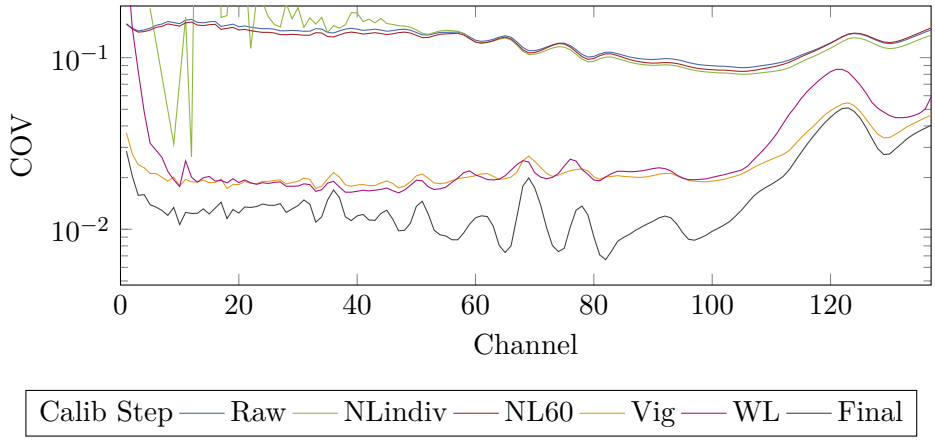

Figure (4.21) COV per channel between pixels for different calibration steps indicating the effect on enhancing the quality of the data. The data was acquired outdoors on a white reference under sunny conditions. Raw represents the raw data. The nonlinearity was estimated individually for each channel for NLindiv. One representative nonlinearity estimation of channel 60 was used for all channels (NL60). The curve Vig and WL show the COV after applying vignette and wavelength correction. The COV of the best combination of correction steps is plotted as Final.

hyperspectral camera relative to the sun and rotating the reference panels reduced environmental influences and allows calculating a mean cross calibration factor as the quotient of the resampled Qmini spectrum and the spectra measured with the camera. In Fig. 4.22c, a mean factor of all pixels and acquisitions is plotted. The other two lines represent the mean factor $\pm 3\,\sigma$ standard deviation.
An evaluation of the cross calibration was performed using two measurements that are independent of the calculation of the calibration factor. First, the acquisition of a dataset of the 51 % reference panel and second of the 96 % reference panel, each with synchronously measured irradiance. The first plot of Fig. 4.23 shows the respective mean reflectance spectra and $\pm$ the standard deviation, and red lines specify the reference values of the panels. The other two images represent the mean reflectance image of all channels respective to the plot above. Even if the deviations are small, especially in the right image, a spatial dependency is visible as a trend of about 4 % from the lower image margin to the top margin. This effect could be caused by stray light entering the lens system from outside the reference panel due to a slight lit towards the sun. During field campaigns depending on the ambient conditions and acquisition strategy, this effect was observed to be even larger. Therefore, it is not recommended to use reference panels in a setup like it is shown in Fig. 4.24. Here, the angles between the sun and the camera's line of sight are unfavorable, and the distance between the reference and the camera is also very short. This means that influences such as shading and reflections can affect the measurement. An experimental setup also revealed that flexible reference materials (calibration tarp) must be used with caution. Variations

of up to 20 % depending on the structure have been observed (Fig. 4.25). These influences would have a direct effect on the calculation of the remote sensing ratio when using this image as a reference and would thus systematically affect the results.
Therefore, reference panels of sufficient size should be used in the field. These should be able to be measured in flight at low altitude, or ideally from the intended flight altitude. Reference tarps should not be folded for transport, but rolled up to avoid creasing. It is also advisable to measure the reflectance standards with different orientations of the camera, especially changing the azimuth to the sun. This allows directional effects to be taken into account in post-processing.

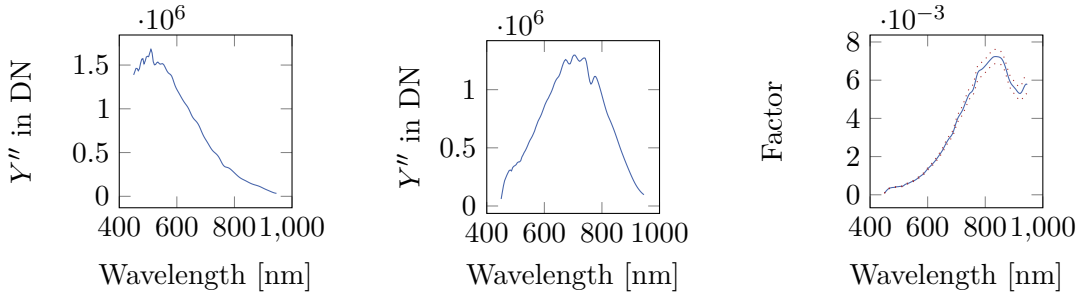

(a) Irradiance Spectrometer. **(b)** Hyperspectral camera. **(c)** Cross calibration factor.

Figure (4.22) Cross calibration of the hyperspectral camera and the irradiance spectrometer. The calibrated and resampled spectrum of the irradiance spectrometer (a) and the calibrated spectrum of the hyperspectral camera (b) are calculated from multiple synchronous acquisitions. Calculating the channel wise factor between these measurements results in the cross calibration factor (c). Mean cross calibration factor (solid line) and standard deviation (dotted).

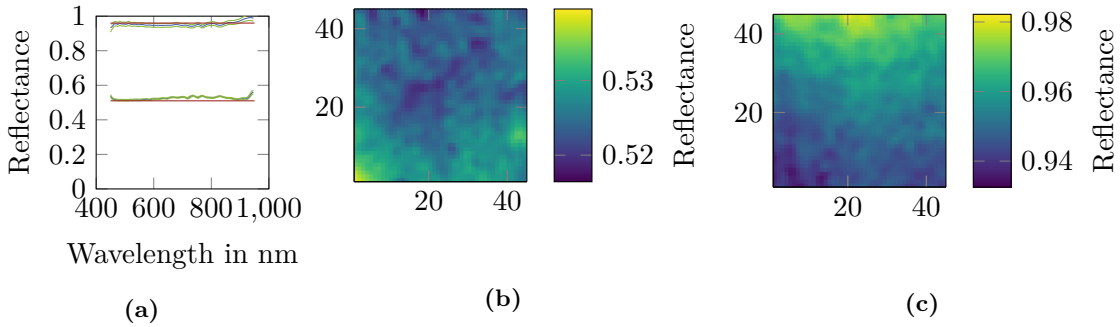

(a) **(b)** **(c)**

Figure (4.23) Evaluation of the cross calibration using two independent measurements on two different reference panels. (a) Measured mean reflectance (blue lines) of a 51 % and a 96 % (red lines). The area between the green lines marks the standard deviation. (b) Mean reflectance of all channels of the 51 % panel. (c) Mean reflectance of all channels of the 96 % panel. A trend from the lower to the upper image margin is visible.

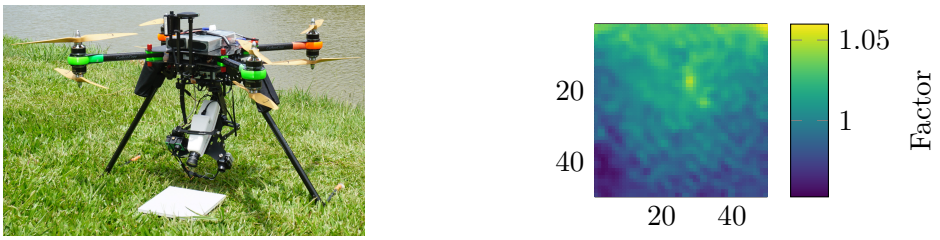

(a) **(b)**

Figure (4.24) Reflectance measurement of a 51 % calibration panel in the field (a) placed underneath the UAV close to the hyperspectral camera for field reference measurements. The normalized image of the channel at 686 nm (b) shows a systematic drift across the image in a range from −5 % to 5 % of the mean reflectance value.

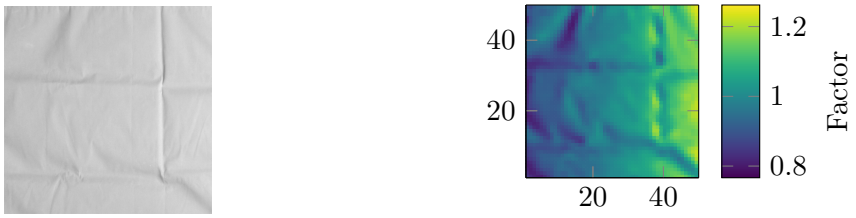

(a) Pan image.

(b) Channel at 686 nm normalized by mean.

Figure (4.25) Reflectance measurement of a 56 % reflectance tarp normalized by mean. The pan image (a) shows wrinkles caused by folding the tarp for transport which are visible in the hyperspectral image (b) as well. Deviations of up to 20 % are visible e.g. for the selected channel at 686 nm.

4.4 Irradiance Correction and Sensor Synchronisation

The downwelling irradiance E_0 is measured by the upward looking spectrometer, which uses a diffusor disk. Therefore, the measured signal E with this spectrometer depends on the angle θ between the z-axis of the copter and the vector from the copter position to the sun. Based on Lambert's cosine law, the measured signal can be corrected as follows:

$$E_0 = E\frac{\cos(\theta_0)}{\cos(\theta)} \quad , \tag{4.11}$$

where θ_0 corresponds to the solar zenith angle [113].

For the correction, it is therefore necessary to know the actual inclination of the copter for each measurement of the irradiance spectrometer. However, the time axes of the copter and the spectral sensors are not synchronized, so a direct application of the correction is not possible, and the time scales have to be synchronized first. By manual inspection of the data, it is only possible to set the time shift with a precision of maximum 0.5 s.

However, the above described relationship between the irradiance measurement influenced by the inclination of the copter can be used to estimate the offset of the time axes between

the copter and the spectral sensors. Here it is assumed that the z-axis of the spectrometer matches the z-axis of the copter. Instead of a spectral channel, the CCD load of the spectrometer can be used. A visualization of the relationships can be found in Fig. 4.26. The first subfigure (Fig. 4.26a) visualizes the CCD load (red) of the irradiance spectrometer and the angle θ (blue) for one exemplary flight. The ups and downs of the CCD load mark different flight lines moving to the sun or away from it. Clearly visible is the relation between the two measured signals. The lower two plots of Fig. 4.26 show scatter plots of CCD load and the angle θ for two situations. First for a time shift of 5 s and second for the same dataset but with synchronized data. This relationship can be linearly approximated by a polynomial for different time shifts Δt around the initial value for the time offset, which is the basis for the following algorithm to find the time offset between the copter and spectral sensors time:

1. Calculate the angle θ for all logged inclination data of the copter.
2. Calculate the RMSE of the linear fit between θ and CCD load for different Δt.
3. Fit a second degree polynomial between Δt and $RMSE(\Delta t)$ to calculate the minimum corresponding to the time offset.

Blue dots in Fig. 4.26b mark the root mean squared error (RMSE) for every time shift Δt. The fitted polynomial of degree two to calculate a more precise estimate of the time shift is visualized as a red line in Fig. 4.26b. Using the estimated time shift, it is possible to get better corresponding copter poses for each measurement of the hyperspectral camera and the irradiance spectrometer, which share the same time axis and therefore enables a more precise georeferencing of the images and a more reliable inclination correction of the irradiance measurements.

4.5 Summary

The aim of the methods, developed procedures, and analyses described in this chapter are, on the one hand the investigation of the spectral sensors and, on the other hand, their calibration. The individual calibration of the two spectral sensors themselves and the subsequent determination of the cross calibration are indispensable for this work. Only the dark current correction, the wavelength calibration, and the determination of the nonlinearity of each spectral sensor enable the cross calibration. After this step, the remote sensing ratio can be measured with the system, which is the basis for the estimation of water quality parameters. Due to the different time scales of the copter and the spectral sensors, the inclination correction of the irradiance measurements was not initially possible. Therefore, a method was developed, to estimate the time offset between the two time scales using the measured irradiance data, the logged copter pose, and Lambert's cosine law.

In the following, the analyses of the hyperspectral camera are briefly reflected and placed in the context of related research work. The camera used in the context of this work has

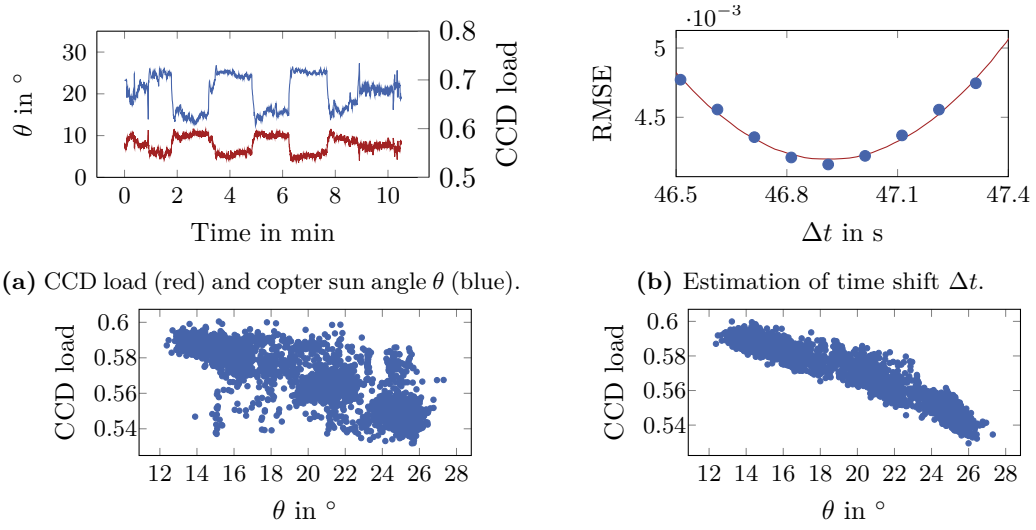

(a) CCD load (red) and copter sun angle θ (blue).

(b) Estimation of time shift Δt.

(c) Time shift: 5 s.

(d) Synchronized data.

Figure (4.26) Synchronization of the hyperspectral sensors and the copter using irradiance measurements (CCD load) and the copter sun angle θ (a). The relationship of the CCD load and θ is plotted for a time shift Δt of 5 s (c) and a synchronized dataset (d). This relationship is approximated by a linear fit for different Δt and the minimum RMSE is estimated to calculate the time shift (b).

already been used in the context of different research works and was also investigated in e.g. [110, 112, 113]. The determined values for the DC are similar to the studies in [111]. [110, 121, 112] also found an undulating pattern similar to Fig. 4.20 which could be caused by a coating of a beam splitter [111].
In [113] the spectral resolution of the camera was examined with the help of a monochromator. Here, clear deviations from the values provided by the manufacturer are visible, whereby the spectral resolution becomes worse with increasing wavelength than specified by the manufacturer (cf. Fig. 4.3).
While in [101] and [31] also variations of the center wavelengths could be detected, this was not possible within the scope of this work due to the available measurement equipment and the spectral resolution of the camera. However, the investigations here showed that possible variations with the used camera occur below the spectral sampling. The large deviations of the center wavelengths of this hyperspectral camera published in a previous study [101] (see also Fig. 3.1) can probably be attributed to a damage of the sensor since these were no longer measurable after an overhaul of the sensor by the manufacturer. Due to the drop in spectral resolution with increasing wavelengths and possible variations of center wavelengths at the edges, the range for further use of the spectra is restricted to the range from channel 5 to channel 95, which equals a wavelength range of 466 nm to 826 nm.
In the context of this work, the nonlinearity of the sensor was calibrated, while in other works, the use of the measurements is limited to the linear range of the sensor [111, 113], our approach allows the use of the sensor over a wider range. Nevertheless, spectra with

low maximum signal amplitudes should not be used to ensure a good signal-to-noise ratio. Therefore, spectra with a maximum amplitude of 500 DN or smaller were not included in further steps.

In addition to limiting the wavelength range and discarding spectra with low amplitudes, the use of spectral calibration standards in the field was also investigated. With the help of the cross-calibrated system it was shown that, depending on the acquisition geometry and material of a spectral calibration standard, systematic deviations can occur and therefore the cross-calibrated approach is preferable.

The following recommendations can be made regarding the frequency of calibration. It is particularly recommended to check the wavelength calibration before campaigns and after software updates or possible damage. The check can be carried out without laboratory equipment using standard fluorescent lamps. These provide the necessary spectral peaks, which enable a rough check of the calibration. Due to the continuous stress on the sensor caused by vibrations and bumps during operation on a UAV, a complete characterization should be carried out annually, including a check of the cross calibration or absolute calibration of the spectral sensors.

In Chap. 7, the influence of the calibration is taken up again as part of the overall evaluation. It is shown that continuous measurement of the irradiance is necessary for reliable parameter estimation and that the tilt correction of the irradiance spectrometer also has an influence on the target variables.

CHAPTER 5

Study Area and Field Campaign

To evaluate the remote sensing system, developed methods and the processing pipeline, data were acquired during a field campaign in 2020 on an artificial water reservoir close to Curitiba, Brazil. Ground truth data was generated from analyzed water samples and in-situ measurements to evaluate processed remote sensing data. The following sections briefly introduce the study area and describe the process of reference data sampling and the data itself. Followed by a description of the datasets acquired with the UAV.

5.1 Study Area

All datasets have been acquired at the drinking water reservoir Passaúna in the west of Curitiba, Brazil (see Fig. 5.1) in the framework of the research project MuDak-WRM [9]. The artificial lake is about 11 km long, has a surface of approximately 8.5 km^2 and a mean depth of 9 m [122, 123]. It was built in the 80s and provides drinking water to 0.7 mio people. The trophic state is oligotrophic to mesotrophic [9, 124].

The part in the north of the reservoir, the so-called buffer region, and the adjacent part of the main reservoir are especially interesting in terms of large temporal variations and flow dynamics. Therefore, this region is chosen to serve as the study area in this work. The sediment load of the incoming river in the north can settle down in the buffer, before entering the main reservoir. At the end of the buffer, after passing a bridge, a lateral gradient of suspended sediment was observed (see Fig. 5.1) and therefore, it is an adequate situation to investigate the performance of the system and algorithms.

The field campaign was carried out in March 2020, from the 5th to the 15th, on five selected days. The weather was always sunny in combination with occasional larger and smaller clouds. There was no heavy rain event during the campaign and no strong winds.

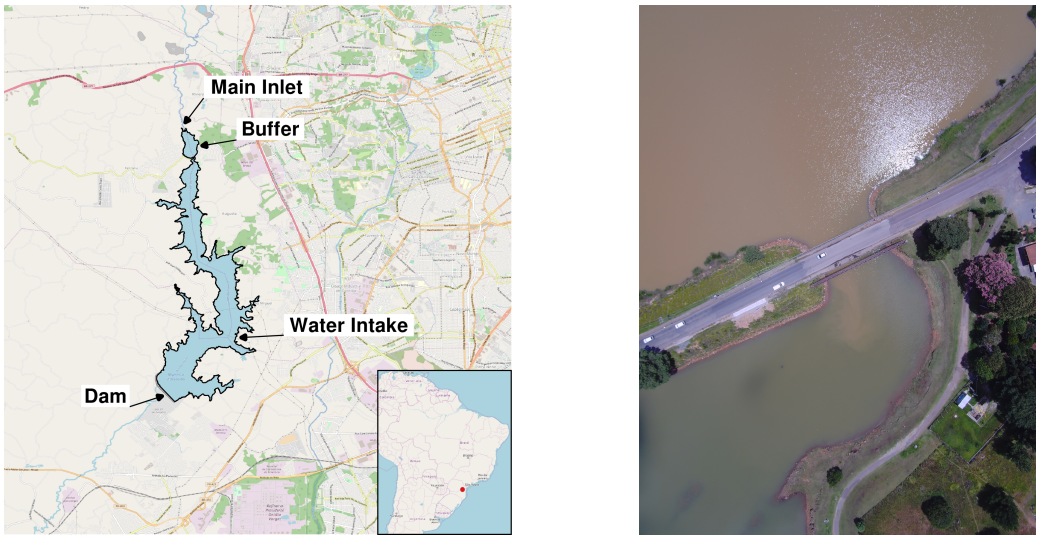

Figure (5.1) Passaúna reservoir, located in the west of Cuitiba, Brazil. The right image shows an RGB image acquired with the system. It shows the area where the water passes the bridge at the end of the buffer. In the upper part of the image, the water of the buffer with a high sediment concentration can be seen, and a gradient after passing the bridge. Map data ©OpenStreetMap contributors.

5.2 Groundtruth Measurements

During the field campaign, the following parameters have been sampled as reference to evaluate the remote sensing data: water temperature, TSS, turbidity, chl-a, and phycocyanin. The water samples were taken and in-situ measurements were acquired from a boat in approximately 15 cm depth. The chosen sampling positions are overlapped by as many flights with the UAV as possible. During the campaign, the in-situ measurements were carried out as simultaneously as possible or with a small time offset to the remote sensing data. However, time offsets of up to two hours are possible. The parameters were measured with different sensors and methods. The sensors and acquired data are described briefly below.

Water Surface Temperature

The water temperature (in °C) was measured using a CastAway-CTD by Sontek. The accuracy of the temperature measurements is specified as 0.05 °C by the manufacturer. To measure the water temperature close to the surface, the profile measurement setup was used. At least two profiles were measured at each point to prevent erroneous measurements due to possible heating of the device while stored in the vessel. The temperature measurements were screened, and the values registered in a water depth of 15 cm were used.

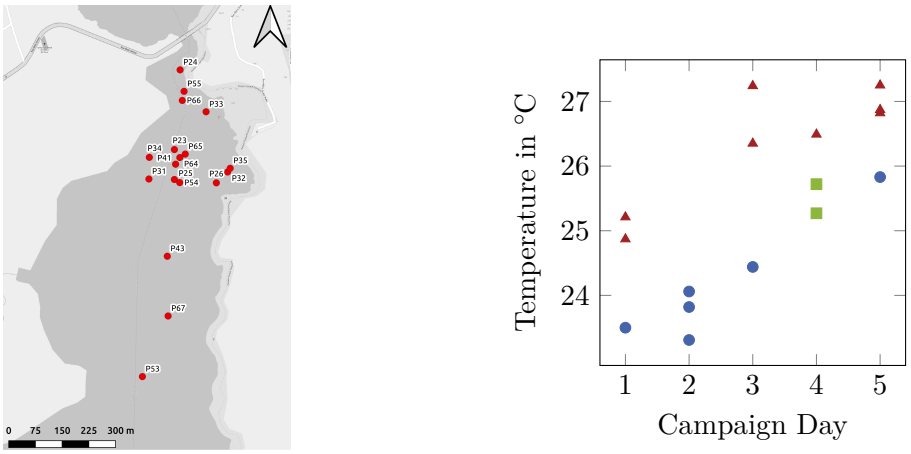

(a) Sampling positions of ground truth data.

(b) Measured water temperatures.

Figure (5.2) At each day of the campaign multiple in-situ measurements were carried out and water samples taken at different positions (a). In (b) the water temperatures measured on each day of the campaign are visualized. The blue dots mark measurements before the flights, the green squares during the flights, and the red triangles after the flight. Map data ©OpenStreetMap contributors.

A representation of the water temperatures for each campaign day is given in Fig. 5.2b. The temperature measurements are classified according to the time of measurement. Measurements, which were made before the flights are marked as dots, during the flight as squares, and after the flight as triangles. Even if the temperature measurements were partly at different positions, there are temperature differences between the measurements before and after the flights, which can only be related to a change of the water temperature in total and not relative to the measurement points. These daily temperature variations are expected and are also mentioned in the literature, e.g. [125, 126]. Therefore, the choice of the in-situ measurements for referencing the temperature mosaics and their validation must be made with measurements that are close in time to each other and to the flights. Overall the measurements show a general increase in the water temperature from the first to the last day of the campaign.

Turbidity, TSS and chl-a

Turbidity (in NTU), chl-a (in $\mu g\,L^{-1}$), and phycocyanin (in $\mu g\,L^{-1}$) concentrations were measured using the respective TriOS sensors nanoFlu and Turb. The manufacturer of the in-situ sensors specifies the accuracy by $\pm 5\,\%$. During the processing of the data, the first few measurements at each sampling position of the in-situ sensors are ignored due to a running-in characteristic. All remaining values of each point were averaged.

Total suspended solids (TSS, in $mg\,L^{-1}$) were determined through analysis of taken water samples. The taking of water samples was performed simultaneously while acquiring multiple

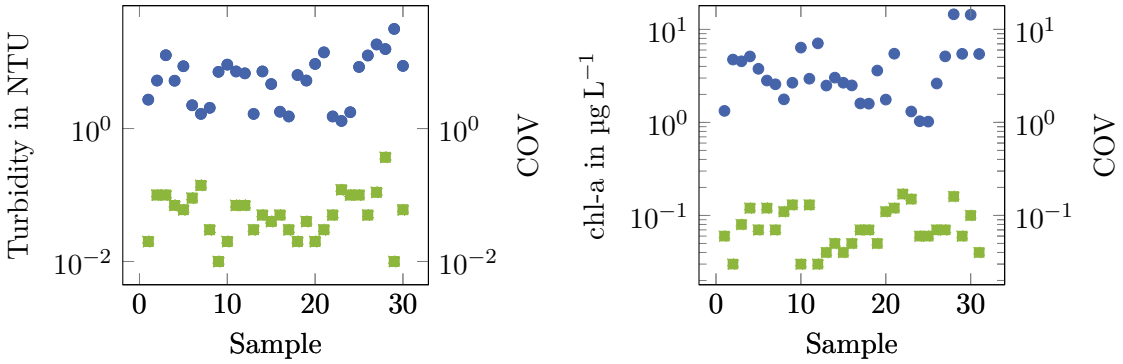

(a) Turbidity.

(b) chl-a.

Figure (5.3) Mean turbidity and chl-a concentration measured in-situ (blue dots) at each sampling position during the campaign. The corresponding coefficient of variation is plotted as green squares.

measurements with the in-situ sensors. At each sampling point, the sample volume was at least 1 L, at points with expected low turbidity, 2 L of water have been sampled. The water samples were stored in a thermo box until the analysis in the lab. Per water sample, the TSS concentrations were analyzed by at least two sub-samples to identify outliers and to get an averaged result. The filtering of the water samples for the determination of the TSS concentration was carried out according to [127]. Additionally, independent turbidity measurements were conducted in the lab.

An overview of the measured reference data for turbidity and chl-a concentration and the coefficient of variation for each parameter and sample is given in Fig. 5.3. The in-situ measurements show turbidity values less than 40 NTU for all samples during the campaign. The chl-a measurements are also low, with a maximum value of 23 µg L^{-1}. The mean coefficient of variation (COV) for turbidity is 0.07 and chl-a is 0.08. Measurements of phycocyanin show values close to zero with high standard deviations. Therefore, these measurements are not further used and discussed in this work.
The analyzed water samples have TSS concentrations less than 70 mg L^{-1}. A comparison of turbidity measured in-situ and in the lab, and analyzed water samples is given in Fig. 5.4. The left figure shows a scatter plot of the measured turbidity in the lab and the TSS concentrations determined through the analysis of the water samples. In the right scatter plot, the in-situ measured turbidity is plotted against TSS. Both plots also show a linear fit which is forced to intersect the origin. The metrics of the fit indicate that the measurements and lab analyses are plausible and that the units of this campaign data can be transformed into each other.

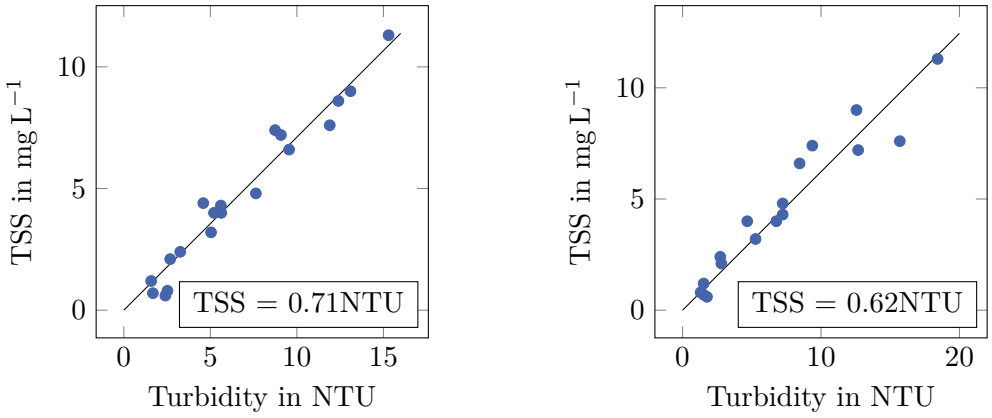

(a) Turbidity measured in the lab. $R^2 = 0{,}9576$. **(b)** Turbidity measured in-situ. $R^2 = 0{,}9184$.

Figure (5.4) Scatter plots of TSS lab analysis and (a) lab and (b) in-situ measurements of turbidity. The lines show a linear fit for each plot forced to intersect the origin. The corresponding formula is also given. Outliers due to inappropriate sampling have been removed.

Bathymetry

Based on the bathymetry obtained from a high-resolution echo-sounder survey [128] and the calculated relationship between measurements of secchi disk depth and turbidity (see Fig. 5.5a), a map showing areas with less than 1.2 m water depth at a water level of 885 m a.s.l. was generated (see Fig. 5.5b). The threshold of 1.2 m was chosen based on turbidity values of 7 NTU in the relevant part of the study area. This mask can be used later to mask areas where the parameter estimation may have been influenced by bottom effects due to the low water level during the campaign.

5.3 UAV Datsets

With the system presented in Chap. 4, RGB images, thermal images, hyperspectral images and irradiance measurements were acquired in parallel continuous streams with different but at least 1 Hz acquisition rate during the campaign. The RGB and hyperspectral camera recorded images with at least 1Hz, the thermal camera and the spectrometer with more than 20 Hz. The imaging sensors were mounted on a gimbal to allow a nadir configuration, but the values of the orientation of the gimbal could not be recorded. Therefore, a nadir configuration is assumed. Data were acquired with different trajectories (see Fig. 5.6) during a sunny weather period with only occasional larger and smaller clouds. The flight plans were chosen in such a way that firstly, a large area can be covered, secondly, there is an overlap between the flights, and thirdly, the orientation of the camera is changed.

Tab. 5.1 lists the flights and the corresponding flight plan configurations. Gray entries show flights where the hyperspectral camera did not acquire any data or acquired unusable data.

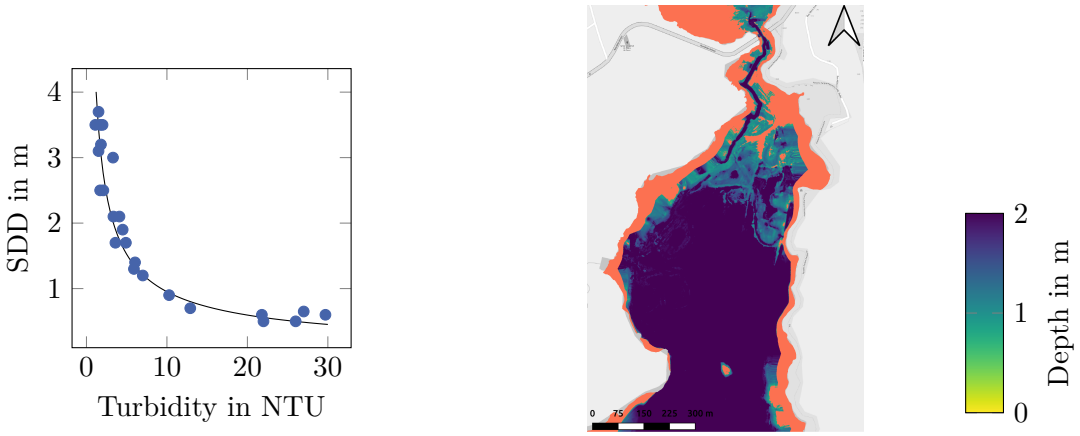

(a) (b)

Figure (5.5) Scatter plot of turbidity and secchi disk depth (a) and bathymetry map (b). The orange overlay of the map shows area with possible bottom reflectance where the water depth is less than 1.2 m. Map data ©OpenStreetMap contributors.

The methods and results of processing the thermal remote sensing data are presented in Chap. 6, and the parameter estimation from spectral measurements is discussed in detail in Chap. 7.

Table (5.1) Acquisition dates and flight plan types. Gray entries mark flights where no, or no usable hyperspectral data were acquired. The paths of the flight plans are visualized in Fig. 5.6.

Day	Date	Flight Plans
1	05.03.2020	A, B, C
2	06.03.2020	A, B, C
3	09.03.2020	A, B, C
4	10.03.2020	A, B, C
5	15.03.2020	A, B, C

Instead of a stop-and-go mode of the copter and single acquisitions of the sensors, a continuous flight mode was chosen. This is necessary, as the gimbal can not fully compensate the abrupt starts and stops, and a logging of the gimbal orientation is not possible with this system. Therefore, the deviations from the nadir view of the cameras would directly affect the georeferencing of the images. However, there are advantages of using a constant flight speed and a high data rate. First, the movement of the copter and also of the orientations of the attached sensors are smoother, which simplifies the processing of the data. Second, the high spatial overlap of the images along the flight track can be used in the further processing of the data and enables the generation of more reliable image mosaics due to the high redundancy for each ground point. Third, a continuous flight mode enables a faster measurement progress compared to stopping for each acquisition.

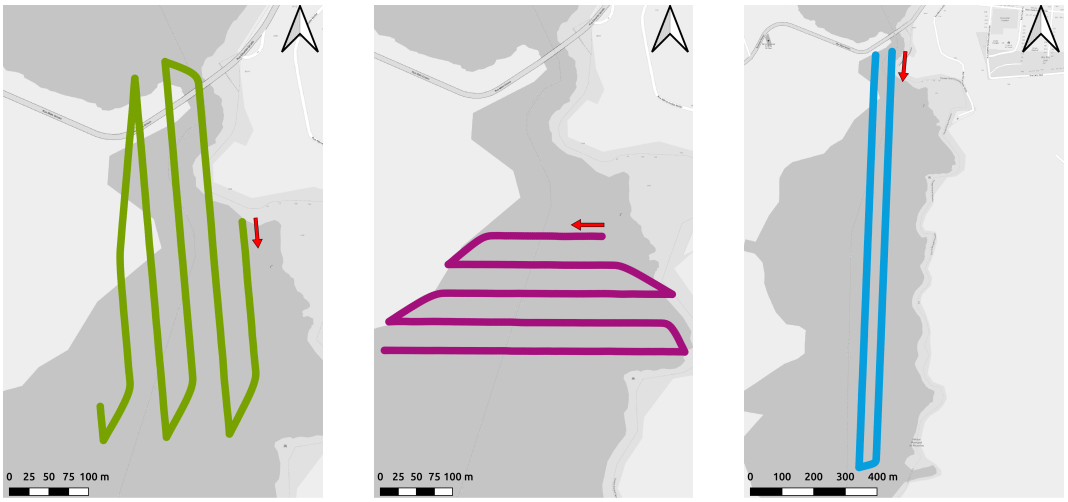

(a) Flight plan A. **(b)** Flight plan B. **(c)** Flight plan C.

Figure (5.6) Flight paths of the different flight plans. The red arrow marks the direction of the flight and the starting point for data acquisition.

The flight height of the system is set to 120 m above ground level (AGL) with a flight speed of $6\,\mathrm{m\,s^{-1}}$. The flight duration was approximately 10 min, with approximately 900 hyperspectral images and 3500 thermal images acquired during each flight. The collected data of each flight covers an area of about $0.14\,\mathrm{km^2}$.

Geocoding

The georeferencing of the single images is done in several steps and is the same for each camera. First, the images are georeferenced, assuming a nadir image using the intrinsic calibration parameters of the respective camera and the pose of the copter at the time of acquisition. Subsequently, a correction of the georeferencing for each flight strip and, if necessary, a global correction must be applied. The geometrical offset between the flight lines is determined from several overlapping image pairs from two adjacent flight lines. For this purpose, images acquired over land are used, and features are detected using the KAZE algorithm [129] implemented in MATLAB. Subsequently, a mean offset in X and Y is estimated using several image pairs and the detected corresponding points. Finally, the mosaic may be shifted to adjust a residual offset using ground control points. The description of the mosaic generation and corresponding blending procedures for each sensor type are described separately in the chapters on thermal (Chap. 6) and spectral data (Chap. 7).

CHAPTER 6

Water Surface Temperature

The water temperature is a determinant factor for primary production [130], and its change affects the composition of occurring species and oxygen concentration [11]. Therefore, the temperature is a key parameter for water resource management. While e.g. thermistor chains allow studying the vertical temperature profile at single points with high accuracy, a spatially extended acquisition of temperature measurements is difficult to realize and costly [131]. Another method to measure the water surface temperature is the use of thermal remote sensing sensors which measure the emitted thermal radiation of objects which can be related to the object temperature. Hence, thermal remote sensing is used to measure the water surface temperature as a complementary parameter with a wide variety of systems on ground, air, and space [131, 132, 133].

In this chapter, the remote sensing of the water surface temperature and relevant research papers are briefly introduced. After this, the acquired thermal images are analyzed and the developed methods to correct the sensor characteristics and to calculate mean mosaics are presented. Finally, the results are evaluated qualitatively and quantitatively using reference measurements.

6.1 Thermal Remote Sensing of Water

Like all terrestrial objects, water emits thermal radiation which is usually measured by remote sensing sensors in the wavelength range from 8 µm to 14 µm. As the emitted radiation of real objects differs from an ideal black body, the emissivity of the object needs to be considered and in the case of water, an emissivity of $\varepsilon \approx 1$ is usually assumed to measure the radiation temperature. Since the radiation temperature differs from the true temperature of the respective surface, an appropriate correction by in-situ measurements or further assumptions is necessary [134]. Traditionally thermal remote sensing is carried out by sensors on satellites and airplanes.

In recent years, the development of small, and lightweight, but uncooled, thermal infrared (TIR) cameras enabled the use of small UAV for remote sensing of the water surface temperature at low costs [114, 30, 135]. These systems allow the acquisition of high-resolution data at low costs, flexible times, and with little preparation effort. Therefore, the system used here is also equipped with a lightweight thermal camera (see Sect. 4.1). However, the great added value of the data from these small, usually uncooled, sensors is opposed to difficulties in evaluating it. Findings from three other research papers [24, 136, 116] are briefly listed below to highlight these challenges.

Many of these challenges using uncooled and not radiometrically calibrated TIR cameras are described in [24], which is shortly summarized in this paragraph. The sensitivity and offsets of the single microbolometers of the sensor array, which capture the incoming thermal radiation, change with sensor temperature, which is especially crucial during the warm up phase after turning on the camera. Also, the thermal radiation emitted from other parts inside the camera affects the measurement. While operating on a UAV, special attention must be paid to the changing characteristics due to wind-induced temperature changes of the camera body, lens, and sensor. Usually, the parameters to correct these characteristics are updated regularly during acquisition by taking a dark image with an internal shutter closed. However, this flat field correction usually does not provide reliable results especially when e.g. strong temperature gradients and wind affect the individual components of the camera differently. Therefore, further corrections must be applied after data acquisition which is called nonuniformity correction (NUC).

Some practical considerations of UAV based TIR acquisition are shared in [136]. They recommend acquiring data with a nadir looking sensor to reduce angular-dependent effects like reflections (e.g. sky and bankside objects) and changes in emissivity. Depending on the setup, atmospheric corrections need to be included in the processing. In particular, this is necessary when absolute data needs to be acquired directly and no in-situ measurements are available for reference.

A comparison of data acquired with a cooled and an uncooled sensor is presented in [116], where the presented workflow attempts to correct all sensor-specific characteristics and is evaluated against in-situ measurements. It is shown that the calibration of all unknown parameters is challenging, and it is currently impossible to measure absolute temperatures. Therefore, in-situ measurements are essential to receive reliable surface temperature measurements. As their final mosaics still show residual nonuniformity characteristics, a high overlap of the flight lines or optimized processing is recommended. The use of classical photogrammetric methods is hardly employable to the homogeneous water surface to automate the mosaicking process.

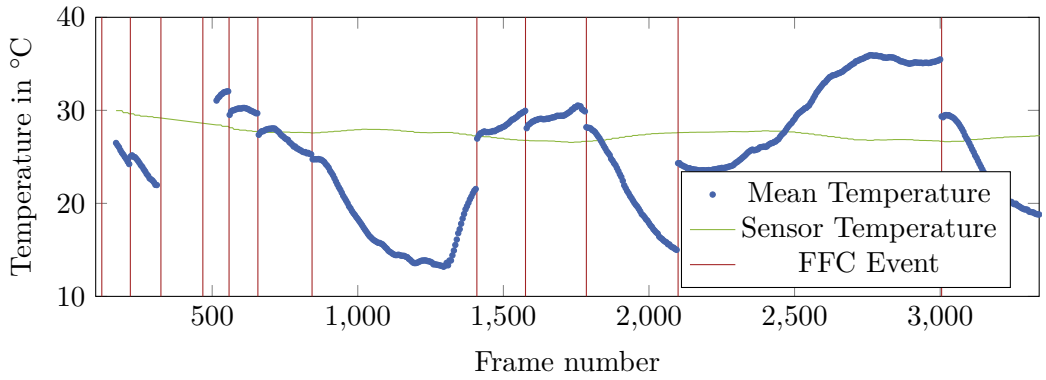

Figure (6.1) Mean temperature of all water pixels per frame of a flight (blue dots). The flight duration was 8 min. Frames over land surface have been excluded. The mean temperature deviates strongly from the expected temperature range between 20 °C and 30 °C while the sensor temperature (green line) only has a slight drift of less than 5 °C. Large temperature offsets occur after the camera performs flat fielding, these events are marked with vertical lines.

6.2 Analysis of thermal Images

During a field campaign in March 2020 at the Passaúna reservoir, close to Curitiba, Brazil, nadir looking thermal images were acquired using a small UAV (see Chap. 4). Data with the uncooled thermal camera was acquired with a frame rate of more than 20 Hz and different flight plan configurations were used (see Chap. 5). To have a general overview of the performance of the thermal camera, the data are analyzed first concerning temporal variation and then concerning spatial variation.

The average temperature of each frame of a chosen flight is visualized in Fig. 6.1 to analyze the temporal variation of the data. The blue dots show the average temperature values of frames showing only water. The sensor temperature of the thermal camera is plotted as a green line. Data points of frames over the land surface were removed. Vertical red lines mark the flat fielding correction (FFC) events of the camera when the internal shutter was closed and the internal NUC updated. The analysis of this raw data acquired during a flight shows a temporal variation and some large offsets. Whereas slight spatial gradients in the water body are expected, the mean temperature of all water pixels per frame shows large temporal variations and offsets that are not expected to occur in the scene. Also, the measured sensor temperature of the camera does not match these effects.

Besides these temporal effects, the spatial variations are analyzed. The investigation of different frames of one flight shows strong varying sensor characteristics superimposing the signal of the water, which should show a more homogeneous temperature distribution (see Fig. 6.2). These variations have magnitudes of up to ±10 °C whereas a much smaller range of maximum ±2 °C is expected. Even if it appears similar to vignetting in some cases, these nonuniformity characteristics deviate from the assumptions of radially symmetric patterns.

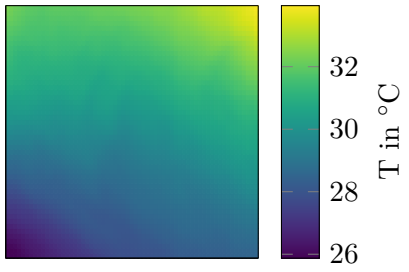

(a) Raw data of frame 1575.

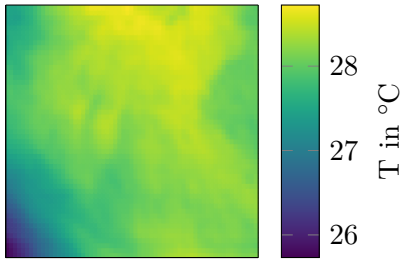

(b) Non uniformity corrected frame 1575.

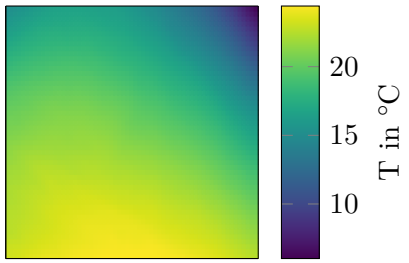

(c) Raw data of frame 3534.

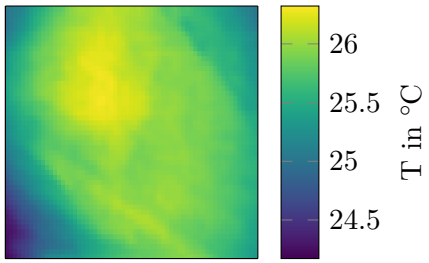

(d) Non uniformity corrected frame 3534.

Figure (6.2) The two rows show two different frames captured with the thermal camera over water during the flight shown also in Fig. 6.1. In the left column the raw data is displayed and in the right column the same frame after correction of the individual nonuniformity. It is clearly visible that the nonuniformity overlaying the signal has a strong variation in shape and magnitude.

Therefore, these effects can not be modeled using the cos^4-law which is usually used for optical cameras (e.g. [137]). Further analysis of the metadata reveals that large offsets and a big change of nonuniformity occur after the flat fielding correction (FFC) events of the camera. The flat fielding is meant to reduce systematic characteristics as e.g. the pixel to pixel bias by closing an internal shutter [138]. However, the analyzed data show that this does not work reliably, and the remaining nonuniformity must be corrected. Due to the strong variation of these dynamic effects, a laboratory calibration is not sufficient for correction. In fact, it is necessary to estimate these characteristics as part of post processing which is illustrated in detail in the next section.

6.3 Correction of thermal Images

The varying sensor characteristics presented in Sect. 6.2 require additional post processing steps to calculate a consistent mosaic of the captured area:

- Nonuniformity Correction (NUC),
- FFC Offset Correction,
- Drift Correction.

First, the nonuniformity correction is applied as it is necessary to calculate the FFC offsets in the overlapping area of two consecutive frames. In the final step, the remaining drift is corrected by calculating the offsets between all used frames. The effects of these corrections applied individually to each frame are visualized in Fig. 6.4. Each sub-figure shows the mean of all overlapping frames of one exemplary flight line.

Nonuniformity Correction

The spatial superposition of the desired signal shown in Fig. 6.2 is known as nonuniformity in the literature [24, 139]. In the datasets acquired with the thermal camera during the field campaign, the observed superposition is up to five times larger than the expected signal variation. A common method to correct this effect is the estimation of the parameters in a lab. For example [30] performs a laboratory calibration to estimate the NUC and applies the correction to the data acquired in the field. This is only possible due to the low speed of their aircraft and the housing around the camera which reduces environmental effects like wind. Another type of correction are single shot NUC methods (e.g. [115]). In [114] this approach was tested, but did not provide good results in an environment comparable with our study area and is therefore not applicable to the data used here as well. As the well-established methods for vignette correction do not fit the requirements and also methods for single shot thermal NUC did not provide good results in a study by Abolt et al. (2018) [114], a suitable post processing method was developed.

Two methods were tested to correct the nonuniformity. First, the nonuniformity was estimated on frames showing only water surface. To correct the NUC of all frames, the model of the nearest correction frame was used. Second, using as many frames as possible. This approach uses a classification algorithm to classify the pixels into the classes water and not water, and estimates the correction only on water pixels for each frame individually.

The first method uses frames which only show water. With each of these frames, the NUC is estimated. To correct the remaining frames, which also show land surface, the nearest available correction of another frame is assigned to the current frame. In Fig. 6.3c the result of using this method is visualized.

In contrast to the first method, the second approach aims to estimate an individual NUC for each frame, which is described in detail in the following. First, each pixel of a frame is classified as water or not water by calculating the standard deviation for each pixel in a 5x5 pixel neighborhood and applying a threshold. The threshold was set to 0.18 °C, whereas smaller values are classified as water. This value was chosen to classify water as land in uncertain cases and might be adjusted for other datasets (in [116] 0.25 °C was chosen to classify images). A particular advantage of this method is, that no data other than the thermal images themselves are required for classification. The resulting masks are then optimized using the morphologic operators opening and closing [140] to eliminate false positives. If the percentage of the water area in a frame is larger than 80 % it is used to model the nonuniformity. The NUC is then calculated in a two-step iterative process. First,

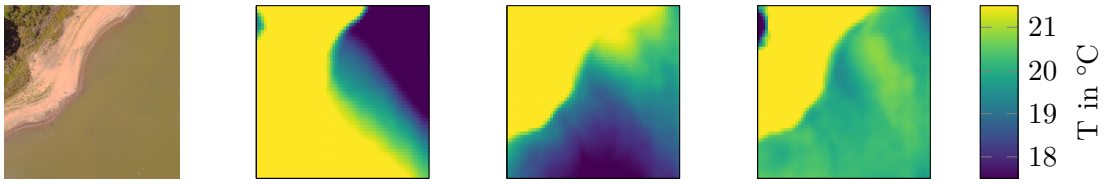

(a) RGB data. **(b)** Raw data. **(c)** NUC of a frame 15 s later. **(d)** NUC of current frame

Figure (6.3) Changing nonuniformity of the thermal images exemplarily shown for the same area as the RGB image in (a). The raw image (b) shows the signal superimposed by the sensor characteristics. The two other images show the same frame corrected by two different nonuniformity correction models where the water is visible as colder temperatures compared to the higher temperatures of the land surface. The image in (c) is corrected by a model estimated on a frame showing only water about 15 s later. In (d) the raw data is corrected by a model estimated on the current frame.

a quadratic polynomial surface is estimated on all water pixels, and the residual for each pixel is calculated. A threshold of three times the standard deviation of the residuals is then applied to exclude pixels from the final estimation of the NUC polynomial. In Fig. 6.3d the corrected raw data using the polynomial estimated with the second approach is visualized.

A comparison of the presented methods is shown in Fig. 6.3. The first image shows the scene captured by the RGB camera, and the other three false color images show the raw thermal image and the results of the two correction methods. The comparison of the two methods to correct the NUC illustrates that the second approach provides much better results than the first one. By assigning the estimated model of one frame to others, the changing characteristic of the nonuniformity can not be corrected reliably. Therefore, the first approach is not sufficient to correct the NUC, as the resulting data still show systematic errors after correction. In contrast, the second method provides much better results. Furthermore, it allows to estimate a correction for most frames of the data set and does not need any other data than the thermal images themselves. This indicates that the nonuniformity correction is not stable even for a relatively short time of less than a minute, which corresponds to Fig. 6.1. Therefore, an individual estimation of the NUC for as many frames as possible is recommended. After applying the individual nonuniformity correction to each frame, the effect is visible in Fig. 6.4b. On the left side of the image, first structures of the water are visible and the gradient in the middle has a clearer structure. This gradient is caused by the offset at an FFC event of the thermal camera, which can be corrected by applying the FFC offset correction described in the following.

FFC Offset Correction

The offsets occurring after the FFC events of the camera (see Fig. 6.1) are visible as a strong gradient in the mosaic after nonuniformity correction (see Fig. 6.4b). Using the relative orientation of the single frames from the navigational data, it is possible to estimate the

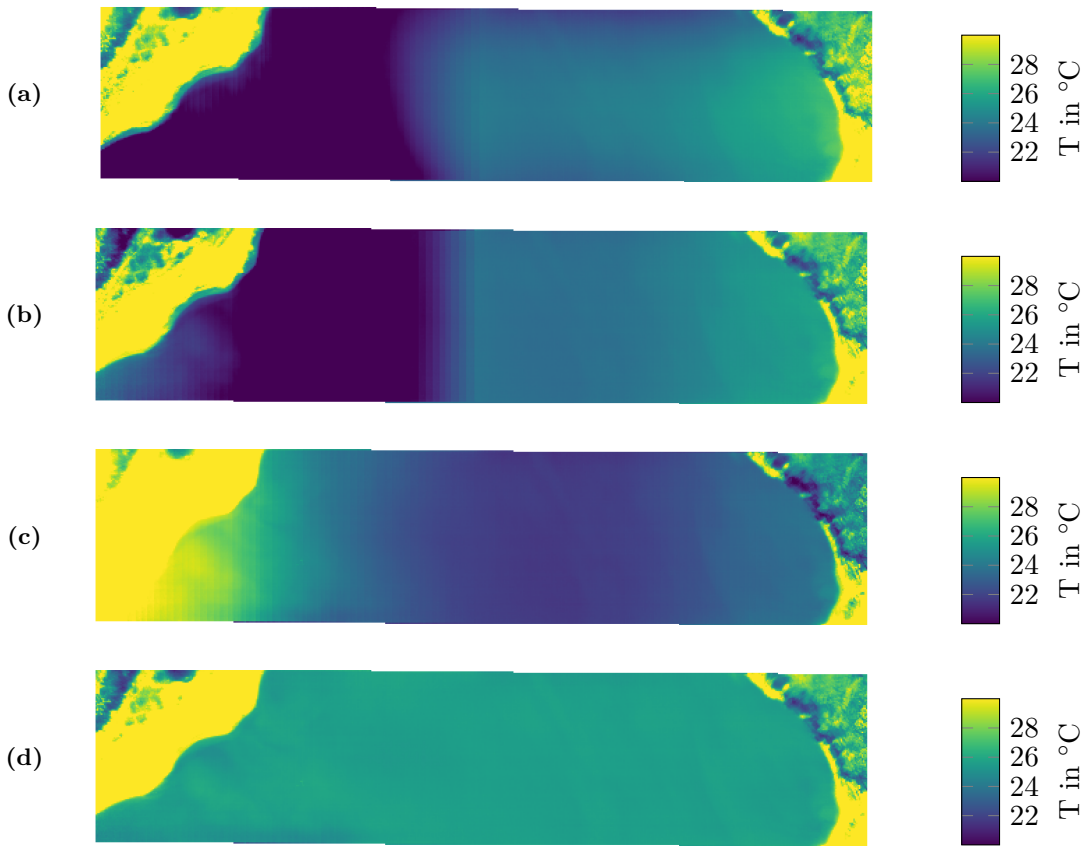

Figure (6.4) Visualization of the applied corrections using the example of a section from an aerial survey. The flight direction is from left to right. The shown mosaics consist of 94 single images, which were calculated as mean of all corresponding frames. (a) Mean mosaic of the raw data. An offset and the influence of the nonuniformity are visible in the center. (b) The estimation of individual NUC improves the mosaic.(c) Correcting the FFC offset removes the gradient in the center, but a variation from left to right is still remaining. (d) An image-based drift correction results in the final mosaic of this section.

temperature offset of the overlapping area of the frames before and after the event.
First, the pixel-wise difference and their mean value and standard deviation are calculated. Then, the pixels of the difference image that have larger deviations from the mean difference than the standard deviation are excluded from calculating the mean temperature offset between the frames. All the corrections are summed up, and the constant values are assigned to each section between the FFC events. After this correction, the strong gradient in the middle of the flight line in Fig. 6.4b is corrected, but a slight variation from left to right is still visible. This variation of the water temperature is not expected to occur in this area and the temperature drift is estimated and corrected in the next processing step.

Drift Correction

The remaining drift, as it is visible in Fig. 6.4c can not be fully explained by the sensor temperature drift and is therefore also corrected using the frame-based approach as it is used to estimate the FFC offsets. To do so, this method is applied to all used frames. Although this step can also include the FFC offset correction, it is performed separately so that it is possible to skip frames which can speed up the processing.

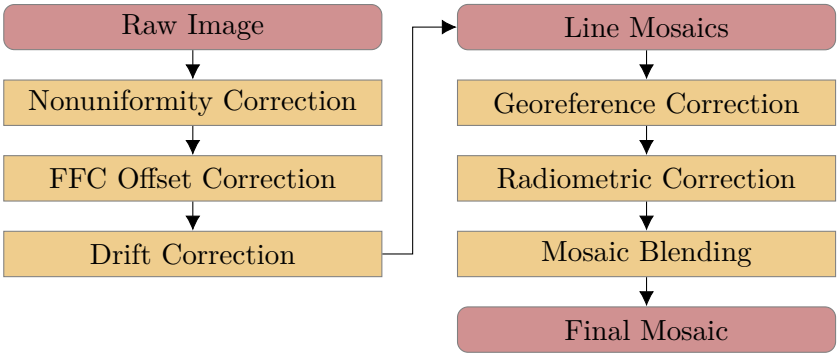

Figure (6.5) Processing steps from raw thermal images to image mosaics. The steps on the left side are presented in Sect. 6.3 and visualized in Fig. 6.4. The steps on the right side are described in Sect. 6.4 and visualized in Fig. 6.6.

6.4 Mosaic Generation

After the frame individual processing steps, presented in the previous section, it is possible to combine the single frames and calculate a mean mosaic. The methods to calculate a mosaic are presented in the following and the process is visualized in Fig. 6.5. Results of the intermediate steps are visualized exemplarily in Fig. 6.6 using two overlapping flight lines. The first plot shows the overlap of two flight lines and reveals two problems. First, a geometric offset, and second, a radiometric offset between the two lines. These offsets need to be corrected first, before calculating the final mosaic. The correction of the geometric offset is described in Sect. 5.3, as the process is identical for all imaging sensors in this thesis.

Radiometric Correction

Due to the sensor drift and the methods used during post processing a constant radiometric offset may occur between the overlapping flight lines. To correct this effect, the overlapping area of water pixels is used to estimate the offsets between the neighboring flight lines as a mean deviation, as it is done to estimate the offsets at FFC events.

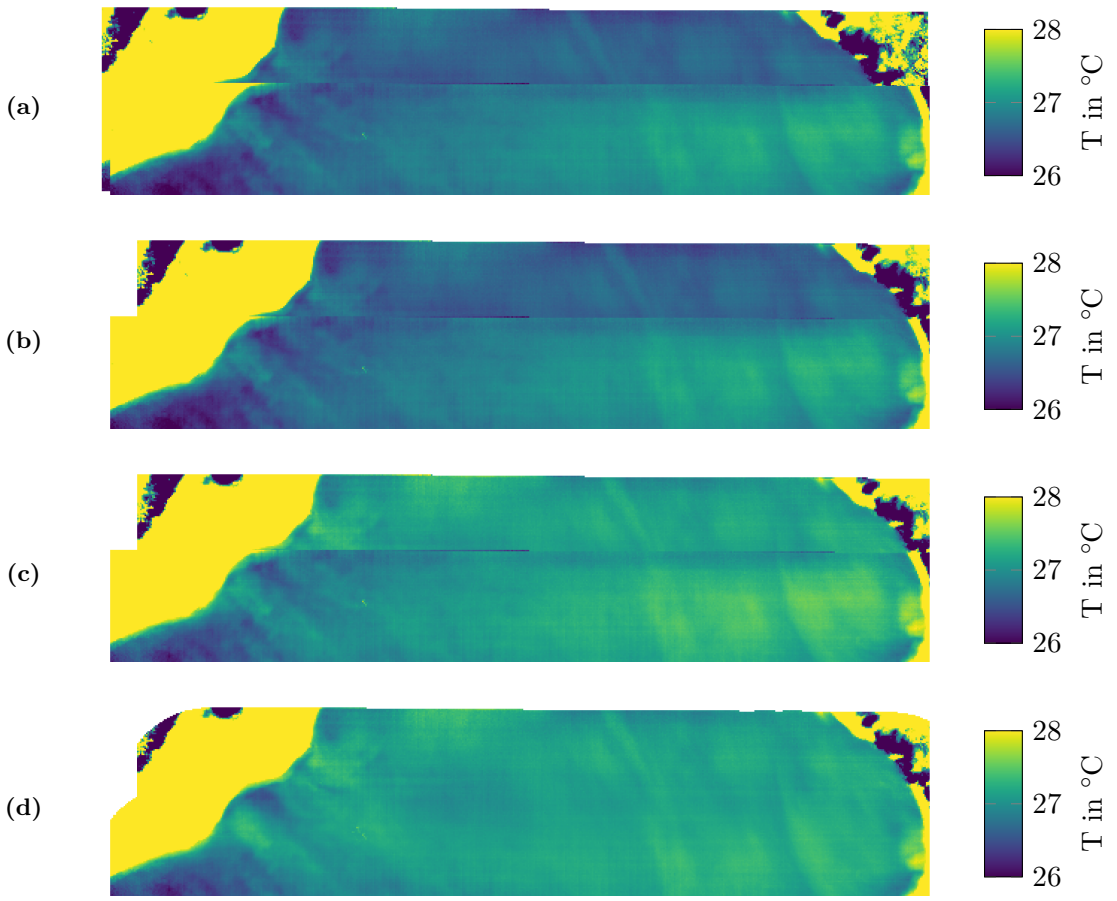

Figure (6.6) Overlapping mosaics of two overlapping flight lines. (a) A clear geometric offset can be seen at the edge areas as well as a slight radiometric offset. (b) Correction of geometric misalignment. (c) Adjusted radiometry to correct remaining offsets. (d) Mean mosaic of all frames. The mosaic is calculated as the weighted mean value per ground point of all corresponding pixels of the corrected thermal images. The weights are derived from the distance of the pixels to the respective image center of the frame.

Mosaic Blending

After applying all processing steps, the final mean mosaic is calculated as a weighted mean of all frames (see Fig. 6.6d). The initial weight $w_{u,v}$ of each pixel $P_{u,v}$ is calculated by the Euclidean distance $d_{u,v}$ of the pixel to the image center. Pixels with a distance value larger than 320 pixels are excluded from calculating the mosaic as it is expected that remaining sensor characteristics especially occur in the corners of the images.
First, the weight of each pixel is defined identically for all frames as

$$w_{u,v} = \left| \frac{d_{u,v}}{max(d)} - 1 \right| \tag{6.1}$$

After this, the weight images of all n frames are mapped to the world coordinate system and the individual weights of each pixel in each frame i are assigned to a world coordinate

X,Y. The individual weights are calculated as:

$$W_{X,Y,i} = \frac{w_{X,Y,i}}{\sum_{i=1}^{n} w_{X,Y,i}} \quad . \tag{6.2}$$

These weights are then used to calculate the mean temperature $T_{X,Y}$ for each point in the world coordinate system using all corresponding temperature values $T_{X,Y,i}$:

$$T_{X,Y} = \sum_{i=1}^{n} T_{X,Y,i} W_{X,Y,i} \quad . \tag{6.3}$$

The final result of processing the raw data to generate the mean mosaic is shown in Fig. 6.7b. In comparison to the mean mosaic of the raw data (see Fig. 6.7a), the enhancement is clearly visible. While the false color representation of the raw mosaic was scaled in the range from 20 °C to 40 °C, the mosaic of the processed data is scaled in the range from 26 °C to 28 °C and shows the details of small temperature variations of the water surface.

Combining two Mosaics

As the system is not able to record the orientation data of the gimbal and a permanent nadir view of the camera is assumed, the resulting mosaic is more blurry than the raw data due to small deviations from that assumption. In contrast to the used method, classical photogrammetry or structure from motion software could generate a high-resolution orthophoto. While it is possible to use this software to process data with lots of detectable and stable features as they appear over land, these algorithms can not be applied to the homogeneous and unstable structure of the water surface temperature. Moreover, the dynamic structure of the water surface results from waves and would be misleading for the algorithm.

However, a combination of both methods is possible. The mosaic of the water surface is calculated using the methods described above. All images containing more than 80 % non-water pixels can then be used for processing with a classical photogrammetry software (e.g. Agisoft Photoscan which was used here). In another step, the two mosaics can be combined, which is shown in Fig. 6.8. The combined data provide more details on the shoreline as it is also visualized by the enlargement of a small inflow of a cold water stream to the warmer water of the reservoir.

6.5 Evaluation

Due to the sensor characteristics and the chosen post processing methods, a direct absolute validation of the mosaics with the in-situ measurements is not possible. To reference the final mosaics an offset was applied so that the mean of all water pixels of the mosaics equals the corresponding mean of the raw data. These mosaics are then compared to the in-situ measurements. It follows first a visual qualitative evaluation and then a quantitative evaluation of the processed data.

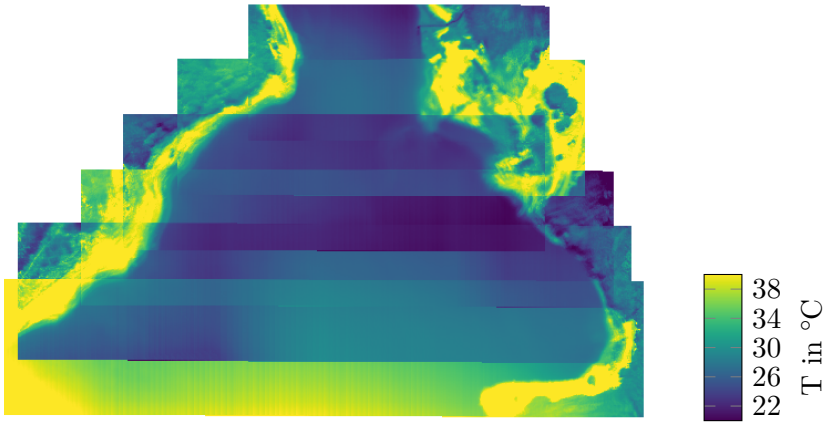

(a) Mosaic of the raw data. Calculated as the mean value of all corresponding pixels per ground point. There are drifts and offsets between the flight lines. The signal of the water is almost completely overlaid by sensor characteristics.

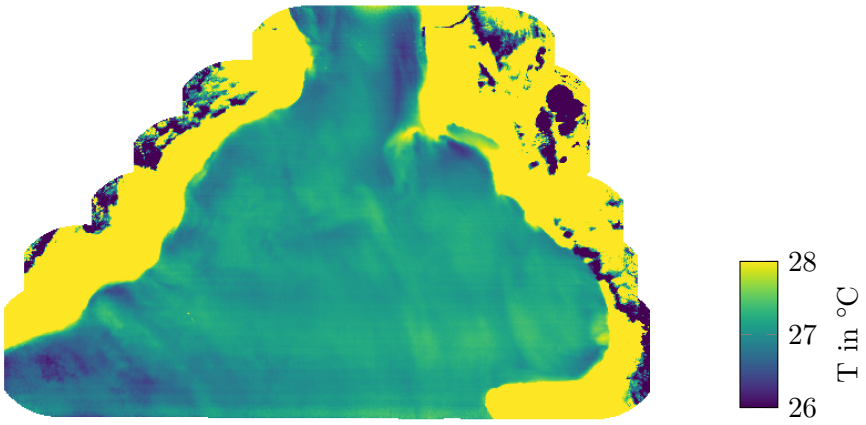

(b) Processed mosaic. A weighted mean mosaic was calculated using the corrected frames. The sensor characteristics have been removed and the signal of small temperature variations of the water surface is visible.

Figure (6.7) Image mosaics showing the mean mosaic of the captured raw data (upper plot) and the processed data using the developed method (lower plot). While the raw data shows large drifts of up to 20 °C, the processed data reveals the spatial structure of the water surface temperature.

Qualitative Evaluation

A qualitative, visual evaluation of the generated mosaics shows good results but also slight structures which are probably caused by remaining sensor characteristics. In Fig. 6.7b, this is indicated by slight horizontal stripes and temperature variations transverse to the flight direction which are probably not caused by the water temperature. Variations of the water temperature, which could be related to the water depth can only be seen in the littoral zone. Surface water, which was warmed up at the shore, is moved by wind and water current,

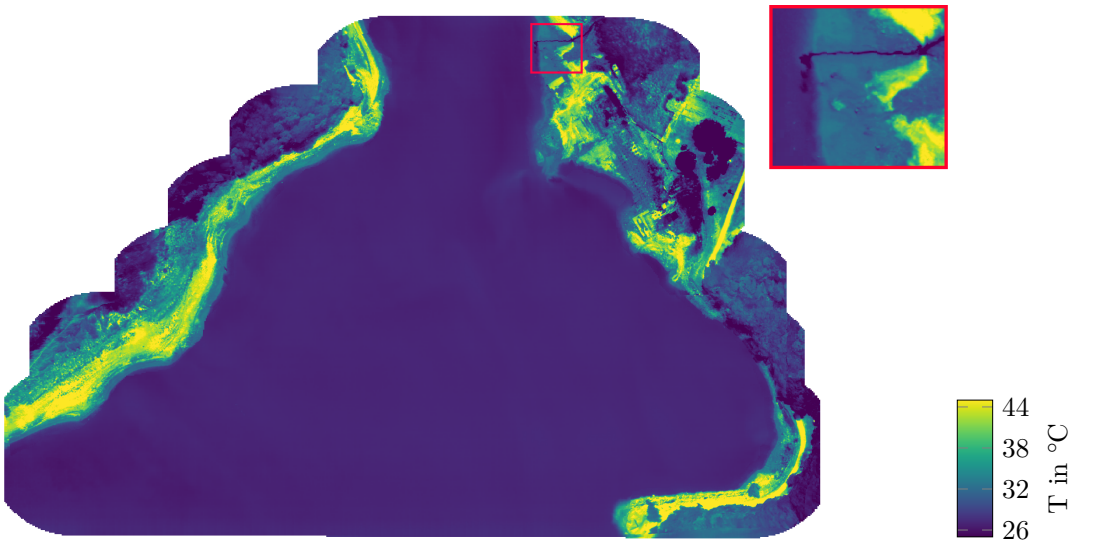

Figure (6.8) Combination of two methods to generate the mosaic of the water surface temperature. The water surface was mapped using the developed method and the land surface was calculated as a orthomosaic using a photogrammetric software.

which is also visible in the data. Also, the disturbance of the water surface by e.g. boats is visible in the data, which is not shown here.

The combination of mosaics using the presented method and a classical photogrammetric method shown in Fig. 6.8 still has inconsistencies in the overlapping water areas of the mosaics. As mentioned before, the application of methods relying on stable features can not be applied reliably to water surfaces. Therefore, this behavior is as expected and this data is not evaluated quantitatively. However, the used software provides good results for the land surface.

Quantitative Evaluation

The deviations between the temperature mosaics and the reference measurements are shown in Fig. 6.9a. The measurements marked with an $\times$ do not overlap spatially with the area captured by the respective flight. They are located in a radius of up to 100 m to existing measurement data. The partly large differences between the temperature of the mosaic and the reference measurements are caused by the sensor characteristics and the method to reference the temperature mosaics. In general, the temperature measured within the mosaics is lower than the corresponding in-situ measurements. Furthermore, the deviations between the in-situ data for single flights visible in Fig. 6.9a match the differences which are present in the in-situ data itself (cf. Fig. 5.2b in Sect. 5.2). These differences are caused by the period between the single in-situ measurements and the flights, during which the water itself warms up by the corresponding difference. In contrast, temperature differences within

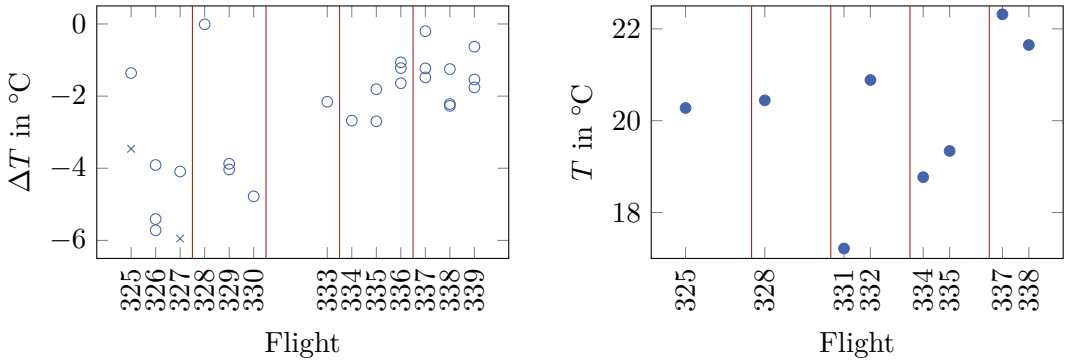

(a) Temperature differences between the processed mosaics and the reference measurements. Measurements marked with an × are not in the area of the corresponding flight.

(b) Temperature of a small cold water inflow to the reservoir. The measurements of different days and flights are visualized for comparison.

Figure (6.9) The temperature mosaics of each flight are evaluated using in-situ measurements at each day of the campaign (a). The temperature of a small cold water inflow is extracted from the mosaics and visualized in (b). The vertical lines indicate the days of the campaign.

a mosaic can be determined very precisely. Here, an average deviation of only 0.33 °C was determined by comparison with in-situ measurements.
An inflow of cold water into the warmer reservoir in the northeast (see red box in Fig. 6.8) allows further evaluation of the data. It is assumed that the temperature of the inflowing water is constant at least within one measuring day. On the second day of the campaign an in-situ temperature of 19.7 °C was measured. The temperature of the water of this narrow stream after referencing the mosaics is shown in Fig. 6.9b. Considering days four and five there is only a small variation between the temperature measured in the data of two flights. On day three, however, a large deviation is to be seen. Possible errors can be caused by an insufficient correction of the sensor characteristics because the chosen location for the measurement is surrounded by land, and therefore the NUC could be faulty. Also, the missing daily synchronous in-situ measurements to precisely reference the mosaics can lead to offsets due to the temporal variation of the water surface temperature. Furthermore, the influence of mixed pixels from water and land due to the resolution and the spatially narrow watercourse cannot be precluded. Altogether the temperature of the water inflow measured in the thermal images varies in the range from 17.2 °C to 22.2 °C.

6.6 Summary

The developed data driven methods provide good qualitative results and reveal the slight temperature variations of the water surface after applying the corrections to the raw data (cf. Fig. 6.7). The qualitative comparison of the image mosaics with other studies shows that the developed method facilitates a more consistent mosaic (cf. [116, 114]).

Good qualitative results were also achieved in [30]. They estimated the NUC in the laboratory and applied the corrections to the measurements. Presumably, the use of this preliminary estimation of nonuniformities and application to field measurements is possible due to the slow movement of the system with $1\,\mathrm{m\,s^{-1}}$, reducing a cooling through wind, and mounting the sensor system inside a box which further reduces environmental effects on the camera [141]. Mosaic generation was carried out with pixel-wise averaging, whereas the developed method in this work uses weighting according to the distance between the pixel and the image center. Furthermore, in [30] images are taken only along the boat's trajectory, which allows omitting the development of methods to combine overlapping flight lines.

A common approach to get absolute temperature values is the use of in-situ measurements to reference the data. Using this approach mean deviations of $0.33\,^{\circ}\mathrm{C}$ to other in-situ measurements could be achieved which aligns with the values in other studies (see [142, 136, 116]).

To further reduce remaining fixed pattern noise, additional filtering using e.g. Fourier transformation could generate better results. This requires a detailed investigation of the data to prevent filtering variations in water surface temperature instead of only reducing sensor characteristics. Besides optimizing the processing of the data, it is presumed that better protection of the camera against environmental effects would facilitate a significant reduction of the variable sensor characteristics (cf. [141]).

To sum up, with the help of the developed automatic processing workflow, the camera can be used quickly and without any special prior knowledge to investigate the temperature distribution of the water surface. This can be used to detect currents on the water surface and also colder or warmer water inflows into a water body. In addition, an absolute referencing of the data using synchronous in-situ temperature measurements facilitates precise temperature maps with accuracies below $1\,^{\circ}\mathrm{C}$.

CHAPTER 7

Spectral Data and Parameter Estimation

In addition to water temperature, other parameters such as total suspended solids (TSS) and chlorophyll-a (chl-a) provide essential information about the state of a surface water body. Since these substances in the water affect the properties of the sunlight reflected from the water body, variations in the reflectance spectrum can be measured with passive imaging sensors such as hyperspectral cameras and put in relation to these parameters. Based on this, methods can be developed to map the spatial distribution of these substances in near-surface water using UAV-borne hyperspectral cameras. In this chapter, the data acquired with the system are analyzed regarding their spectral characteristics to illustrate the processing challenges. For parameter estimation using the reflectance spectra, machine learning models are trained using simulated data, and the real-world data is evaluated using reference measurements. For the spatial mapping of the parameters, methods are developed to create maps of the parameters from many individual images. The developed methods focus on automating the process from data acquisition to the final parameter maps as far as possible to reduce interactions with the process which require expert knowledge or further in-situ measurements.

7.1 Spectral Data and Preprocessing

The estimation of water quality parameters such as total suspended solids (TSS) and chlorophyll-a (chl-a) is based on the variation of reflectance spectra which depends, among other influences, on the changing concentrations of the various components of the water body (see Chap. 2). In Fig. 7.1 this variation of reflectance spectra is shown. The three spectra were acquired during one flight of the field campaign at the drinking water reservoir Passaúna in the west of Curitiba, Brazil (see Chap. 5). Corresponding in-situ measurements showed higher TSS concentrations in the north than in the south and decreasing concentrations in between which is also represented by the spectra. In general, a low TSS concentration leads to a lower reflectance, which increases with increasing concentration. The vertical lines at 670 nm and 810 nm show the relevant points in the spectrum for chl-a absorption

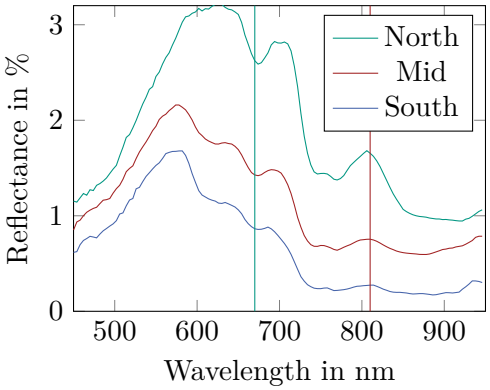

Figure (7.1) Reflectance spectra at three different positions measured by the hyperspectral sensorsystem during the field campaign. On a trajectory of 1 km length in the study area presented in Chap. 5 these positions were chosen as the TSS concentration decreases from north to south. The vertical lines at 670 nm and 810 nm show the relevant points in the spectrum for chl-a absorption (green) and scattering on non-algal particles (red). A low TSS concentration leads to a lower reflectance, which increases with increasing concentration.

and scattering at non-algal particles (NAP). The strong increase of reflectance in the region of 750 nm to 790 nm is also worth mentioning, which may be an indication of an increasing influence of reflections at the water surface such as reflection of sunlight (sun glint).

Particularly the influence of sun glint and under changing weather conditions, cloud shadows highly influence the data. Cloud shadows affect the measurements of the water leaving radiance but can also cause falsely assigned irradiance measurements to calculate the remote sensing ratio which leads to erroneous reflectance values. Sun glint on the other hand only affects the upwelling radiation which is measured with the hyperspectral camera in our case. Sun glint is the direct reflection of sunlight on the water surface and depends on the structure of the water surface, viewing geometry and sun position. It affects the signal in the NIR region of the spectrum where higher glint causes higher reflectance values. However, care must be taken for shallow or turbid waters as in these cases also changes occur in this region of the spectra [47]. Both influences, sun glint and cloud shadows, are presented in the following section and additionally in Fig. 7.2.

Within one frame the chosen image shows little sun glint (marked in blue) and also a slight cloud shadow (marked in red). The mean spectra and associated standard deviations shown in Fig. 7.2b represent the variation within the areas marked in Fig. 7.2a. Within the image shown, no variation in water quality parameters can be assumed, so the variations shown are only induced by ambient influences. The effect of glint on the measured spectrum is apparent. A general offset to the other spectra and especially an increase of the reflectance in the range of the longer wavelengths can be seen. Despite this high variation of reflectance within the image, it is possible to obtain a reliable estimate with low scatter within this scene using the PLS model presented in Sect. 7.2. However, a stronger glint has a greater

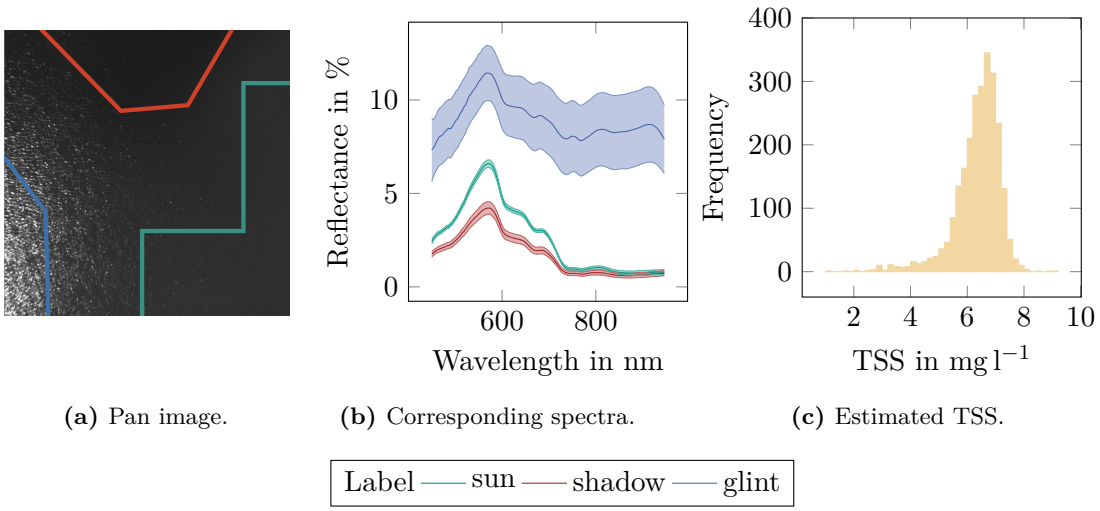

(a) Pan image. **(b)** Corresponding spectra. **(c)** Estimated TSS.

Figure (7.2) Panchromatic image (a) and corresponding mean spectra and standard deviation of the marked areas (b). Clearly visible is the sun glint in the lower left area of the image (blue). The cloud shadow in the upper part is hardly visible (red). The area illuminated directly by the sun without glint is marked green. To calculate the reflectance spectra an unshaded irradiance measurement was used. The histogram shows the estimated TSS values of all pixels of the corresponding hyperspectral image.

influence on the reflectance spectra (see Fig. 7.5). Therefore, the parameter estimation must consider this during processing or affected pixels could be excluded.

While the previously presented influences only affect the radiance detected by the hyperspectral camera, other influences affect the irradiance measurement. This particularly concerns the incorrect assignment of irradiance measurements to the individual pixels since this system assigns one representative measurement of the irradiance spectrometer to each image. A distinction can be made in the following four cases:

1. Irradiance spectrometer in the sun and ground point in the sun
2. Irradiance spectrometer in shadow and ground point in shadow
3. Irradiance spectrometer in the sun and ground point in the shadow
4. Irradiance spectrometer in the shadow and ground point in the sun

These cases are visualized in Fig. 7.3 where different reflectance spectra for all four cases of a ground point are shown. The dashed spectra show the correct cases one and two, and the dash dotted spectra the cases three and four. While case three gives a far too low reflectance, case four gives a much too high reflectance. However, it is also evident that the calculated spectra for cases one and two have slightly different characteristics, which is caused by the differences of direct and diffuse illumination. The variations presented here also affect the estimated parameters. Therefore, these effects must be considered during processing, which will be shown later in the chapter on map generation (see Sect. 7.3).

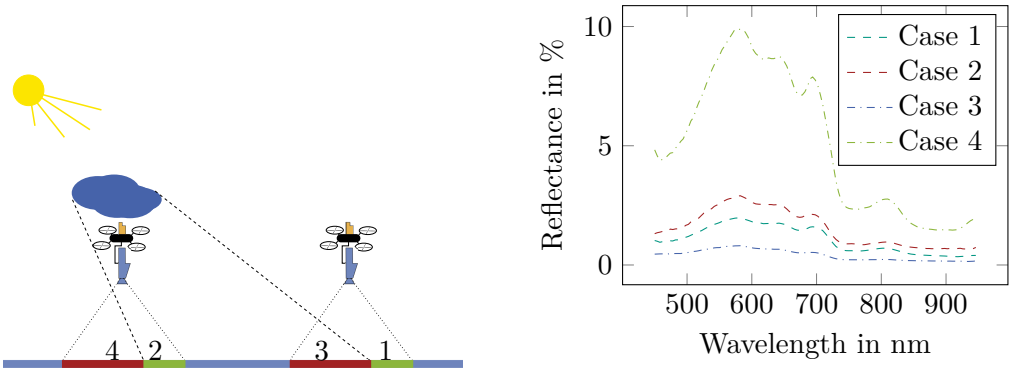

(a) Visualization of different irradiance allocations.

(b) Exemplary spectra.

Figure (7.3) Missallocation of the irradiance measurement affect the calculated reflectance spectra. The cases one and two in (a) represent the correct allocation of irradiance measurements to the ground pixels. The cases three and four represent falsely allocated irradiance measurements. The spectra in (b) correspond to these cases.

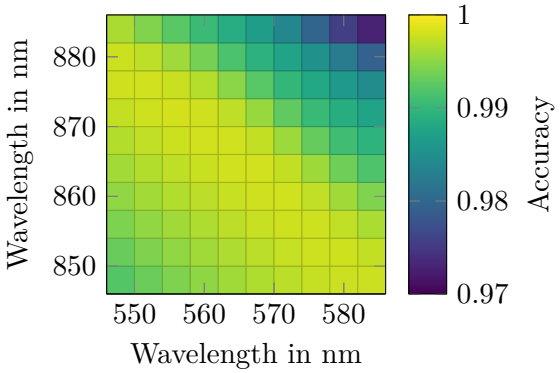

Figure (7.4) Accuracy values of the classification of pixels in water and non-water of the fine grid search for all combinations of channels in a selected range to find the optimal bands for NDWI calculation. The optimal wavelengths are 558 nm for G and 870 nm for NIR.

Data Cleansing

Before the data is actually processed, it must be automatically analyzed and, if necessary, pixels need to be sorted out according to the following criteria:

- Under- and overexposure
- Water and non-water
- Sun glint

First, only spectra whose maxima are in the range of 500 DN to 4000 DN are used for the calculation of the reflectance, to sort out possible underexposure and overexposure. The selection of this range is based on the dynamic range of the sensor.

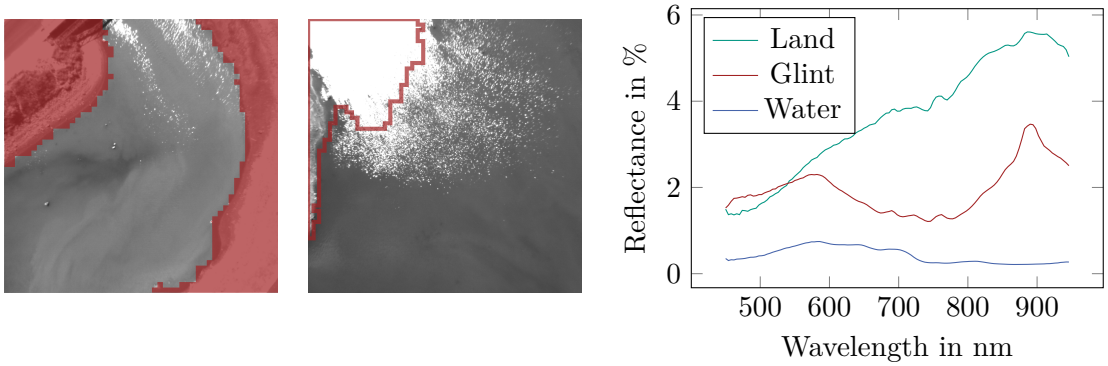

(a) **(b)** **(c)**

Figure (7.5) Two exemplary pan images with masked areas using NDWI. The red overlay in (a) shows the masking of non water pixels using the calculated NDWI. Besides masking non water pixels the NDWI can also be used to mask pixels with a high percentage of glint in the spectrum (red framed area in (b)). Exemplary spectra for land, water and glint are given in (c).

After calculating the reflectance, the normalized difference water index (NDWI, [143]) can be calculated for each spectrum. This is used to mask the land areas. To mask areas in the data which are part of the water surface an NDWI filter is used (see Fig. 7.5). The NDWI is calculated as:

$$NDWI = \frac{G - NIR}{G + NIR} \quad . \tag{7.1}$$

The most suitable bands for calculating the NDWI were determined using labeled data and calculating all possible combinations for wavelengths G : 546 nm to 586 nm and NIR : 846 nm to 886 nm. The spectra used for the fine grid search were labeled using the corresponding pan images. The optimal wavelengths are 558 nm for G and 870 nm for NIR. In Fig. 7.4 the classification accuracy values of the grid search are shown for all combinations of channels.
The classification of the hyperspectral images based on the NDWI is carried out by setting a threshold: values for $NDWI > 0$ are classified as water. In addition, the NDWI is able to mask water spectra strongly influenced by glint reliably with the data used here (see Fig. 7.5b).

While this selection of suitable spectra is automatically applied to all data, a further selection is performed to generate a well selected reference data set for the evaluation of the parameter estimation methods using the sampled ground truth data. The further selection is visualized in the form of histograms of a spectral channel for a ground point in Fig. 7.6. To reduce angle dependent influences only spectra with an azimuth difference between the sun and viewing direction in the range from 90° to 270° are selected after NDWI selection. A last manual step after reviewing the data excludes spectra under diffuse illumination or wrong irradiance assignment.

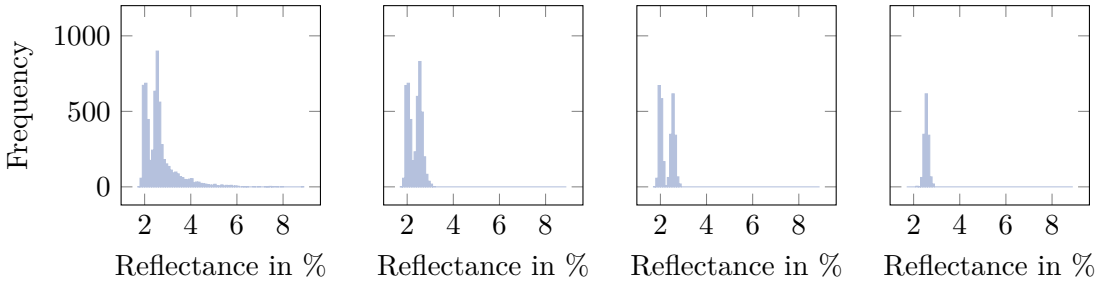

(a) All spectra. **(b)** NDWI. **(c)** Angle. **(d)** Manual.

Figure (7.6) Visualization of the selection process of extracted ground truth spectra with different thresholds. The histograms show the reflectance at 570 nm. The first figure shows all corresponding spectra in a radius of 8 m around the sampling point. Figure (b) shows the remaining spectra after applying the NDWI filter. Then a viewing angle based selection is applied (c). The last histogram (d) shows the spectra remaining after manually selecting spectra which are not shaded by clouds.

Simulated Measurements

In addition to the collected data, spectra were generated using the software WASI [35] (Water Color Simulator, version 5). This software, with its integrated physical model and extensive parameter customizability, allows, besides the inversion, the generation of reflectance spectra of water for a wide range of scenarios, such as glint and suspended solids variation.
In contrast to other available software like BOMBER [144] (only remote sensing reflectance) or Hydrolight [51] (commercial), WASI is freely available and allows the processing of radiance reflectance spectra which corresponds to the data acquired with the hyperspectral sensor system. The dataset generated with WASI in this work serves for the training of different machine learning models, whereby the evaluation of the collected reference data with independent data becomes possible. During the generation of spectra with the WASI tool, the parameters listed in Tab. 7.1 were changed stepwise to achieve the largest possible variation of relevant parameters. A limitation of the number of varied parameters is necessary because with WASI only three parameters can be changed at the same time. A developed software for the control of WASI allows the variation of seven parameters. The selection of the parameters was based on prior knowledge of the water body and analysis of measured reflectance spectra. Since the investigated water has mainly sediment influenced characteristics, the parameter C_X was chosen to determine the TSS concentration. As chl-a concentration the parameter C_5 (green algae) was chosen, because the influences of the variation of the concentration corresponded best to the variations in the real spectra. In addition, the type sand was chosen for the bottom type, because its spectral characteristic corresponds best to the bottom type of the reservoir. Due to the lack of measured values for the CDOM (C_Y) absorption, this parameter was also varied in the data. Because of the partly very shallow water depth, a focus was also put on the variation of the water

depth (zB). For the parameters C_X and zB a logarithmic distribution was used, especially to account for the influence of backscattering of the bottom at low water depth and low suspended matter concentrations. The parameters g_{dd}, g_{dsr} and g_{dsa} are used to create effects similar to sun and sky glint in the data. With g_{dd} the weighting of the direct solar radiation is done and thus the simulation of sun glint. The parameters g_{dsr} and g_{dsa} influence the simulated sky glint. The variation of the parameters resulted in a data set with 896 000 spectra.

Table (7.1) Varied parameters to build a simulated dataset with WASI.

Parameter	Range	Steps	Description
C_X in $\mathrm{mg\,l^{-1}}$	1 - 80	20	Concentration of non-algal particles Type I
C_5 in $\mathrm{\mu g\,l^{-1}}$	1 - 50	8	Concentration of chl-a
C_Y in $\mathrm{m^{-1}}$	0.1 - 5	10	Gelbstoff absorption
zB in m	0.2 - 5	7	Bottom depth
g_{dd} in $\mathrm{sr^{-1}}$	0 - 1	5	Fraction of sky radiance due to direct solar radiation
g_{dsr} in $\mathrm{sr^{-1}}$	0 - 2	4	Fraction of sky radiance due to molecule scattering
g_{dsa} in $\mathrm{sr^{-1}}$	0 - 1	4	Fraction of sky radiance due to aerosol scattering

7.2 Waterquality Parameter Estimation

Before calculating the parameter mosaics, the estimation must be performed on the individual images, since the calculation of an average spectral mosaic is possible only with the full correction of ambient influences which is beyond the scope of this work. In this work methods that can be fully automated in order to require as little expert knowledge of the user as possible were chosen and evaluated. First, different estimation methods are evaluated using simulated data sets to discuss their suitability. In a second step, the methods are evaluated with real data. As the concentrations of chl-a are very low, the presented methods and their evaluation include only the estimation of TSS. Only the simulated spectra and corresponding TSS values were used to train the models. Although bathymetry measurements are available, they were not used as input parameters for the models.

Training on Simulated Data

Besides the established band ratios which are part of the empirical models (see Sect. 2.3) and are mainly applied to satellite data, machine learning methods are increasingly used for the automatic processing of hyperspectral remote sensing data to estimate water quality parameters. Therefore, a selection of commonly used methods for hyperspectral regression tasks was made, which will be applied in the following and their results will be compared.

These are:

- Band Ratios (BR)
- Partial Least Squares Regression (PLS)
- Random Forest (RF)
- Artificial Neural Network (ANN)
- Convolutional Neural Network (CNN)

Before being applied to real data, these methods are trained and evaluated using the simulated data presented in Sect. 7.1. The training and evaluation presented here always refers to the parameter C_X in $\mathrm{mg\,l^{-1}}$, which stands for the TSS concentration in this work (see Tab. 7.1). To reduce the probability of overfitting, gaussian noise was added to the simulated data for the training data (subset of 70 % of the dataset). Gaussian noise with a standard deviation of 0.5 % of its value was added to each channel of the spectra and noise with 2 % of each value was added to the corresponding parameters. As a band ratio method the ratio between 538 nm and 794 nm from [81] was used. The RF and PLS used the Python implementations of scikit-learn [145]. As libraries for ANN and CNN the Python versions of Keras [146] and TensorFlow [147] were used. Within a hyperparameter search the architecture and parameters of the methods shown in Tab. 7.2 were chosen. The ANN and RF showed the best results for scaled input data, that is removing the mean of each feature and scaling to unit variance. While the systematic search for the optimal architecture and parameters was mainly possible, the setting of the number of epochs for ANN and CNN was determined using early stopping when the improvement of the loss function was low or the algorithm optimized parts of the parameter range much different than other parts.

After training, the models were evaluated using a separate subset of the simulated data without noise. The evaluation using the mean absolute error is shown in Tab. 7.3, where D1 stands for the use of the first derivative of the spectra and D0 for the original spectra.

Overall the RF and ANN methods produce very good results and also PLS could give good results with a mean absolute error below $4\,\mathrm{mg\,l^{-1}}$ for the best configuration which is small compared to the simulated range from $1\,\mathrm{mg\,l^{-1}}$ to $80\,\mathrm{mg\,l^{-1}}$ in the WASI dataset (cf. Tab. 7.1). While there is almost no difference between using the original spectrum and the first derivative for PLS, RF gives better results for D0 and ANN and CNN for D1.

It is remarkable that all methods achieve worse results for low concentrations than in the higher range. The results are particularly poor for the PLS model for C_X concentrations below $20\,\mathrm{mg\,l^{-1}}$ where the R^2 is only 0.06, but for concentrations higher than $20\,\mathrm{mg\,l^{-1}}$ an R^2 of 0.88 was achieved. The complete dataset on the contrary achieves an R^2 of 0.97. These results for low concentrations can be particularly attributed to the influence of water depth, whereby the estimation does not only depend on the signal of the water body, but also the backscatter of the water bottom influences the estimation. Using a dataset with only deep water this dependence does not arise. From this follows that especially for shallow

Table (7.2) Parameter setup for the different estimation methods.

Method	Setup
BR	Bands: 538 nm, 794 nm
PLS	Number of components: 40
RF	Treedepth: 15, Estimators:8
ANN	1 Dense Layer; 10 units; activation: ReLU 1 Dense Layer; 1 unit; activation: linear Batchsize: 256; Epochs: 32 Optimizer: Adam; loss: mse
CNN	1 Conv Layer; Filter size: 5; 10 units; activation: ReLU Max pooling; pool size: 2 1 Dense Layer; units: 10; activation: ReLU 1 Dense Layer; units: 1; activation: linear Batchsize: 256; Epochs: 2 Optimizer: Adam; loss: mse

waters the estimation should be discarded or appropriate models must take this effect into account with the help of measured bathymetry.

As the real data only consists of a small in-situ data set, the R^2 value is not given in the following, since it cannot be meaningfully evaluated.

Table (7.3) Evaluation of simulated data. The models were trained on simulated spectra. The mean absolute error in $\mathrm{mg\,l^{-1}}$ is given for each two cases: using the raw spectra (D0) and the first derivative (D1).

Derivative	BR	PLS	RF	ANN	CNN
D0	15.7	3.7	0.6	1.7	6.6
D1	-	3.6	1.1	1.2	5.8

Application to Real Data

After the training and evaluation of the methods using the simulated data, the evaluation using the UAV borne reflectance data measured during the campaign and the corresponding reference values follows. The evaluation is done using extracted spectra in a radius of 8 m around the sampling points. From these spectra a dataset was selected using the preprocessing methods presented in Sect. 7.1. For the evaluation, the corresponding parameters are estimated for all spectra of a point with the models presented in the previous section. Then, the mean value of all estimates per point is calculated. The following evaluations

refer in each case to these mean values. Due to the low water depth at the time of the campaign, there are dependencies of the errors to the water depth. This is shown by the green crosses in Fig. 7.7a which were estimated using a PLS model which was trained using only data with deep water. To reduce the effect of other ambient effects, the used spectra were manually selected. The blue circles, on the other hand, show the errors when using adapted models for different water depths. Separate models for the evaluation in Tab. 7.4 were used for PLS and RF for the following depths, as it was possible to train individual models with reduced dataset sizes:

- PLS: $< 0.5m; 0.5 - 1m; 1m - 1.7m; > 1.7m$
- RF: $< 0.5m; > 0.5m$

As with the use of the simulated data in the previous section, PLS achieves almost identical results with the original spectra and their first derivative using these depth dependent models. In contrary, the RF now performs much better using the first derivative. The CNN and ANN still show an improved accuracy with the first derivative. Especially the results for RF, ANN and CNN could indicate that other influences on the spectra which are not covered by the simulated data are present in the real world dataset. Even though BR seems to give good results, the results are not usable, which would be evident when looking at image mosaics, since this method only estimates parameters in the range of $0\,\mathrm{mg\,l^{-1}}$ to $10\,\mathrm{mg\,l^{-1}}$ independent from the input data and thus is not able to represent the expected variations and is therefore not further considered in this work.

Based on these results, PLS could be selected as the favorite, but further evaluation of the results after mapping is necessary to include possible spatial and depth dependent artifacts in the evaluation.

Table (7.4) Evaluation of real data. The models were trained with simulated spectra. The mean absolute error in $\mathrm{mg\,l^{-1}}$ is given for each two cases: using the raw spectra (D0) and the first derivative (D1). The methods PLS and RF used different models for different water depths.

Derivative	BR	PLS	RF	ANN	CNN
D0	3.1	2.3	7.5	4.6	3.9
D1	-	2.3	2.8	3.7	3.0

7.3 Mapping

After the training and evaluation of the estimation procedures using the simulated and selected real reference data in Sect. 7.2, the calculation of georeferenced image mosaics is carried out to visualize the spatial distribution of the estimated parameters. The processing procedure follows the steps shown in Fig. 7.8. First, the raw data are calibrated and synchronized (see Chap. 4) to enable the reflectance calculation. It follows the data cleansing (see Sect. 7.1) and the estimation of the parameters on the individual images. Then, the

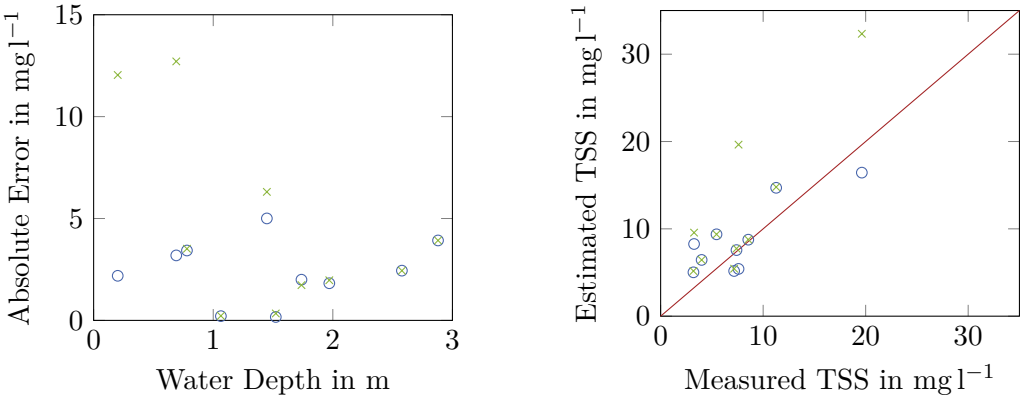

(a) Absolute Error dependent on water depth. **(b)** Scatter plot of measured and predicted TSS.

Figure (7.7) Evaluation of the selected PLS model using groundtruth measurements. The blue circles are the result of applying models dependent on the water depth. The green crosses mark the results for assuming deep water.

georeferencing of the individual images is carried out as described in Sect. 5.3. Subsequently, areas of the individual images are cropped to reduce the remaining influence of glint on the mosaics. The calculation of the mosaics is then done as a weighted average. In a final step, possible artifacts caused by changing irradiance are reduced. The individual steps are described below.

Mosaic Blending

The generation of image mosaics from adjacent or overlapping individual images is a common practice in the evaluation of remote sensing data. Existing methods are therefore adapted to the acquired data. The georeferenced individual images, which are available in a global coordinate system and have been resampled to a uniform raster, serve as the starting point for the following methods.
For the calculation of the image mosaics from the single images, the overlapping areas of the images can be used to calculate an average value for each ground point. Calculating a mean value of the redundant estimates of a single ground point provides spatially smoother results than selecting one representative value for each ground point. Using a simple averaging of all estimates per ground point, stripes with high spatial noise running from north to south are still visible in Fig. 7.9a. These stripes represent the areas where there is no overlap of adjacent flight trajectories. Espcially sun glint causes this spatial noise. Therefore, to calculate the mosaics, a weighted average is inevitable, taking into account the angle between the sun and the line of sight from the ground point to the camera $\nu_{u,v}$ and the distance of the respective pixel to the center of the image $d_{u,v}$. To calculate $\nu_{u,v}$, the relative position of the sun $\mathbf{S}$ is calculated as unit vector and the vector $\mathbf{C}$ to the camera each with

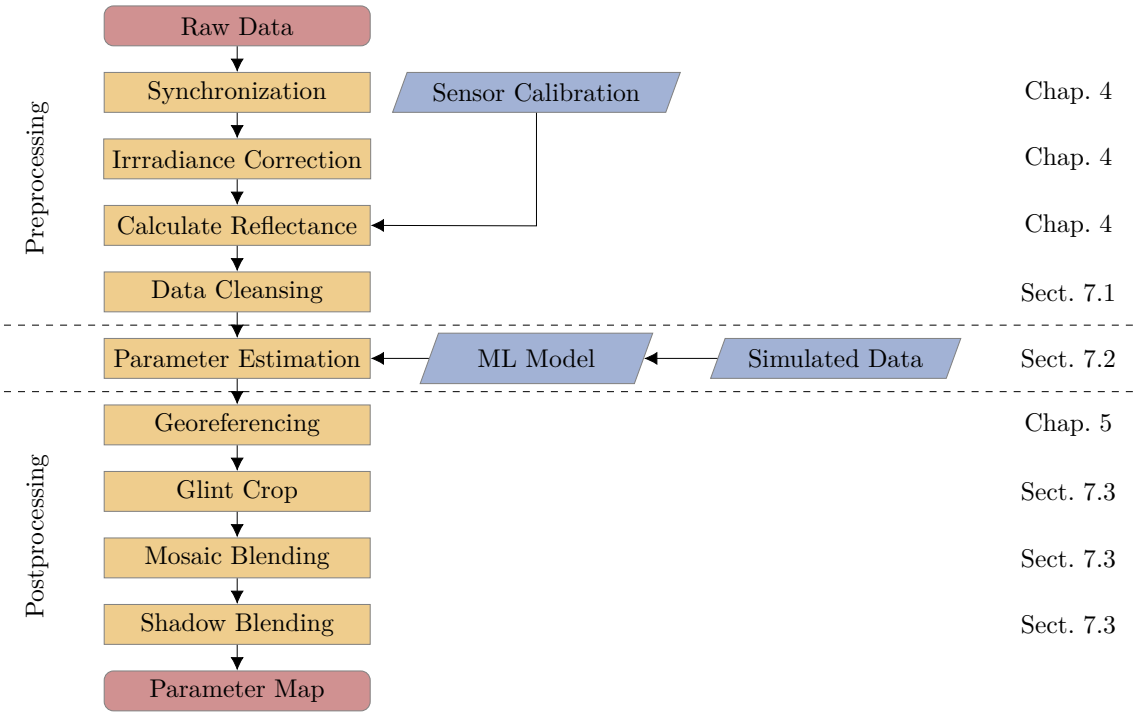

Figure (7.8) Scheme of the processing steps from spectral data to parameter maps. The corresponding chapters and sections are listed on the right side.

reference to the pixel:

$$\nu_{u,v} = \arccos\left(\frac{\mathbf{S}\cdot\mathbf{C}}{|\mathbf{S}||\mathbf{C}|}\right) \quad . \tag{7.2}$$

Then, for each pixel of an image, the previously calculated angles are normalized with

$$w_{\nu_{u,v}} = \left|\frac{\nu_{u,v} - \min(\nu)}{\max(\nu_{u,v} - \min(\nu))} - 1\right| \tag{7.3}$$

and normalized the weights of all n overlapping pixels of a ground point X,Y are calculated:

$$W_{\nu_{X,Y,i}} = \frac{w_{\nu_{X,Y,i}}}{\sum_{i=1}^{n} w_{\nu_{X,Y,i}}} \quad . \tag{7.4}$$

In a further step the weights are calculated which are based on the distances $d_{u,v}$ of the pixels to the image center. First, the distances are calculated and normalized for each pixel:

$$w_{d_{u,v}} = \left|\frac{d_{u,v}}{max(d)} - 1\right| \quad . \tag{7.5}$$

Then the normalized weights for all pixels of a ground point X,Y are calculated as follows:

$$W_{d_{X,Y,i}} = \frac{w_{d_{X,Y,i}}}{\sum_{i=1}^{n} w_{d_{X,Y,i}}} \quad . \tag{7.6}$$

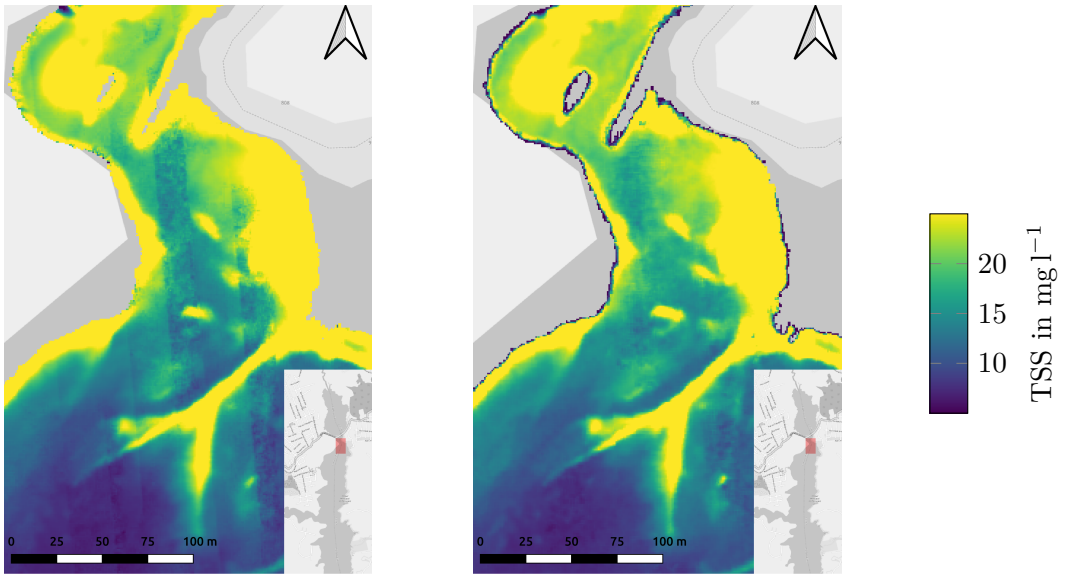

(a) Mean. **(b)** Weighted mean.

Figure (7.9) Mosaic generation using the TSS values estimated with a PLS model by calculating (a) the mean per ground point and (b) a weighted mean per ground point taking into account the position of the sun, the line of sight of each ground point and distance of each respective pixel to the image center.

Finally, the combined individual weights for all pixels of each ground point X,Y are calculated:

$$W_{X,Y,i} = \frac{W_{\nu_{X,Y,i}} W_{d_{X,Y,i}}}{\sum_{i=1}^{n} W_{\nu_{X,Y,i}} W_{d_{X,Y,i}}} \quad . \tag{7.7}$$

The weighted average of the parameter $P_{X,Y}$ for each ground point can then be calculated using:

$$P_{X,Y} = \sum_{i=1}^{n} W_{X,Y,i} P_{X,Y,i} \quad . \tag{7.8}$$

With the calculation of the weighted mean, a reduction of spatial noise was achieved (see Fig. 7.9b).

Glint Crop

To further reduce remaining spatial noise caused by strong sun glint, the glint affected parts of the single images can be cropped (see Fig. 7.10) which is possible because of a high redundancy of estimates per ground point. In this case a fixed percentage of the image is cut. To find the optimal threshold, more and more of the glint affected area of the frames were systematically cropped and for each step the mosaic was calculated and the mean of all local standard deviations in a 15×15 neighborhood was computed (see Fig. 7.10c). Based on this analysis, it was determined that 60 % of the respective frames must be cropped to reduce noise in the final mosaics as much as possible (see Fig. 7.10b). While less crop than

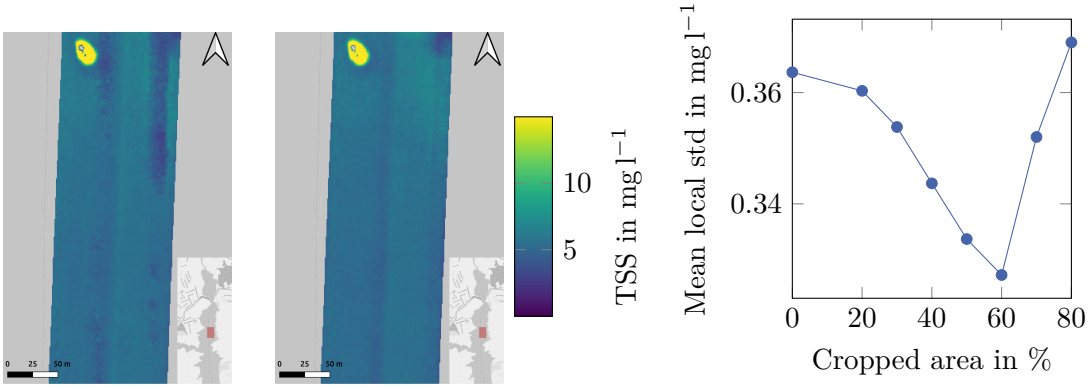

(a) Full images. **(b)** Cropped Images. **(c)**

Figure (7.10) Reducing the effect of sun glint induced erroneous estimations by removing parts of the image faced to the sun. The two maps show (a) using full images and (b) using cropped images (60 %) to calculate the map. The right plot (c) shows the mean of all local standard deviations per pixel with a 15×15 neighborhood as function of the cropped area.

this threshold results in too much glint, a higher value is not possible due to the decreasing number of available values.

Shadow Blending

Under changing irradiance due to clouds it is possible that cloud shadows affect the calculated reflectance spectra and therefore also the estimated parameters. A distinction of the problematic constellations can be made in two cases which are also visualized in Fig. 7.3. One case occurs when the irradiance spectrometer is in the sun and the ground point in the shadow (Case 3). The other case arises when the irradiance spectrometer is in the shadow and the ground point is in the sun (Case 4). For consistent maps a detection and correction of these effects is necessary. While in the context of this work it was not possible to fully correct shadow areas for the Case 3 (see Sect. 7.1), a significant reduction of the influence of the errors by Case 4 could be achieved. In Fig. 7.11a the influence is clearly visible. Measuring irradiance in the shadow of a cloud, and the water surface which is directly irradiated by the sun, leads to significantly higher reflectance values. Therefore, increased estimates for the TSS concentration in this area are obtained. These areas can be detected using different parameter estimations where the irradiance was measured either dynamic or a fixed measurement for sun or cloud shadow is selected. First the following differences are calculated:

$$\Delta_{diff} = M_{dyn} - M_{diff} \quad , \tag{7.9}$$

$$\Delta_{sun} = M_{dyn} - M_{sun} \quad . \tag{7.10}$$

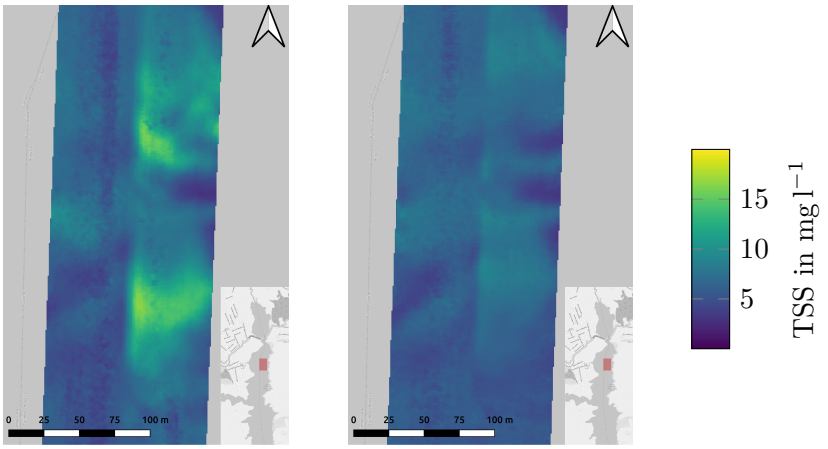

(a) Weighted mean. **(b)** Shadow correction.

Figure (7.11) Blending of different maps to reduce the effects of cloud shadows on the final map. The map in (a) shows the result without correction, in (b) the result after applying the shadow blending is shown where the overestimation of TSS due to misallocation of shadow irradiance measurements to sun pixels is reduced.

Here M_{diff} and M_{sun} represent data for which the reflectance was calculated with fixed diffuse or direct solar irradiance. M_{dyn} represents data for which the dynamic irradiance correction (see Sect. 4.4) was applied. By applying a threshold U_1 to the difference images, the areas with false irradiance assignment can be determined and a mask

$$F = (\Delta_{diff} <= -U_1) \wedge (\Delta_{sun} >= U_1) \tag{7.11}$$

can be calculated which extracts only the areas with wrong assignment. In the next steps, a weighting matrix B for blending is created.

$$B(\Delta_{sun} < U_2) = \Delta_{sun}(\Delta_{sun} < U_2) \tag{7.12}$$

$$B = B/max(B) \tag{7.13}$$

$$B(\Delta_{sun} >= U_2) = 1 \tag{7.14}$$

By element wise multiplication (notated as $\circ$) of the blending matrix B and the mask F, the final blending matrix is obtained:

$$B = B \circ F \quad . \tag{7.15}$$

The final mosaic

$$M_{mos} = M_{dyn} \circ |1 - B| + M_{sun} \circ B \tag{7.16}$$

is now computed as the sum of the weighted mosaics M_{dyn} and M_{sun}, reducing the artifacts due to misallocation of shadow irradiance measurements to sun pixels (see Fig. 7.11).

7.4 Evaluation and Discussion of Mosaics

The methods presented in the previous sections allow the generation of parameter maps which can now be evaluated. In the following, the importance of the dynamic irradiance measurement for a reliable parameter estimation is shown. Subsequently, an areal comparison of several flights is performed to evaluate the repeatability of the measurements. Furthermore, the absolute validation of the final parameter mosaics and a qualitative comparison of the different methods for parameter estimation are performed based on the processed mosaics.

Irradiance Correction

The cross calibrated spectral sensors allow the calculation of the reflectance using the continuous measurement of the irradiance, which makes it possible to take into account changing irradiance during a flight (see Chap. 4). In Fig. 7.12 the influence of the dynamic measurement of irradiance versus a single measurement of a white reference (WR) is illustrated. The three histograms show the estimation of the TSS values using a PLS model for a selected area under sunny and cloudy conditions, respectively, for three cases. First, the use of a WR measurement under sunny conditions, second, the use of the continuous irradiance measurement, and third, the continuous irradiance measurement including the compensation of the inclination of the spectrometer. Below the histograms are the visualizations of TSS maps for these cases. The western half of the mosaics was taken under sunny conditions, and the eastern half under cloudy conditions. The use of a single reference measurement in this case leads to large differences between the western and eastern halves. A clear alignment of the two parts of the mosaic is seen by using the dynamic irradiance measurement and a further improvement by applying the tilt correction.

Repeatability

Three overlapping, consecutive flights on two different days allow an areal comparison of the estimated parameters to evaluate the repeatability of the measurements. This comparison is shown in the form of histograms and scatter plots in Fig. 7.13 where the parameters were estimated with a PLS model. The results shown in the lower row in Fig. 7.13 are based on datasets taken under sunny weather conditions without changing cloud cover. This compares to the results in the upper row, which were taken under highly variable cloud cover. The histograms show in each case the differences in the parameter estimation at identical ground points between the individual flights. For the scatter plots the values of pairs of flights are compared. The flights mentioned first in the legend correspond to the X-axis. From the results shown, it is clear that the system produces consistent results and performs very well, especially under clear sky conditions. The wider scatter in Fig. 7.13a is due to the strongly changing cloud cover and the strong clustering is due to generally lower concentrations on this campaign day compared to Fig. 7.13c.

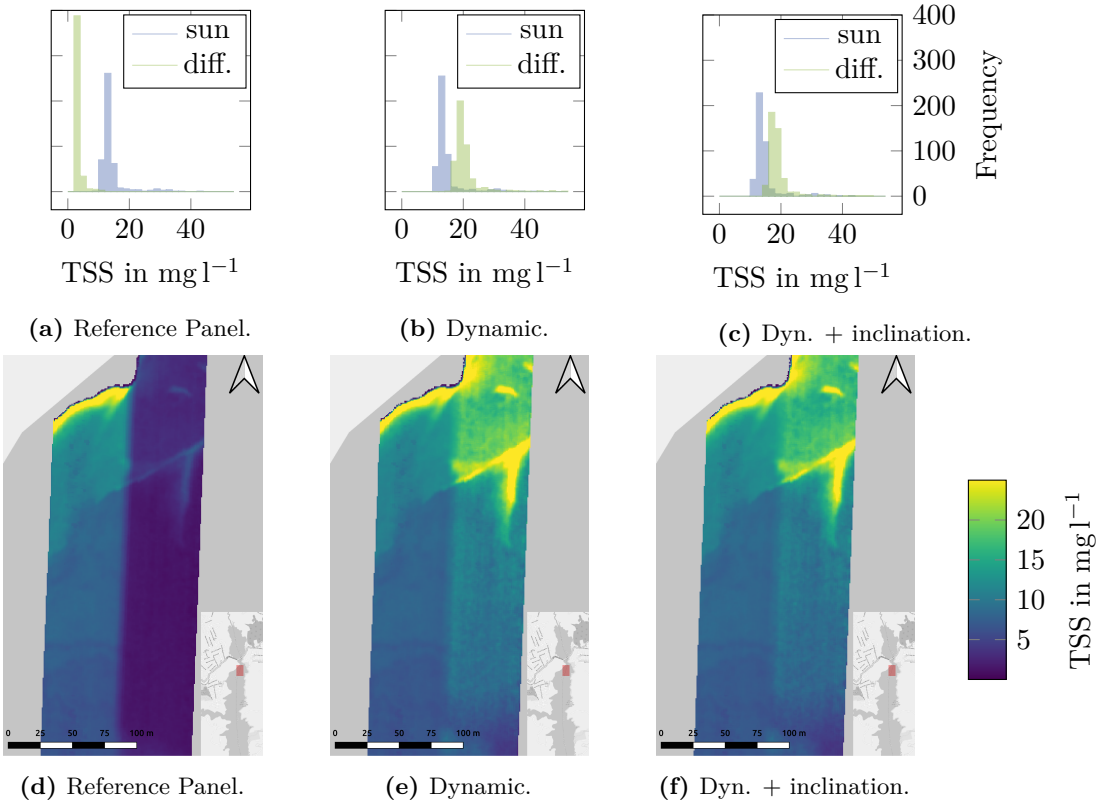

(a) Reference Panel. **(b)** Dynamic. **(c)** Dyn. + inclination.

(d) Reference Panel. **(e)** Dynamic. **(f)** Dyn. + inclination.

Figure (7.12) Effect of different irradiance measurements on the estimated parameters. The top row shows the histograms of the TSS estimation of an overlapping area of two images. One image was taken under diffuse conditions (green bars) the other under sunny conditions (blue bars). The columns show the results for three diferent cases: first using a single measurement of a reference panel under sunny conditions, second using individual irradiance spectrometer measurements and third using individual inclination corrected irradiance measurements for each image to calculate the reflectance.

Quantitaive Evaluation

While the evaluation of the methods in Tab. 7.4 is based on carefully selected spectra to achieve the best possible result, this is not possible for the evaluation of the final maps in Tab. 7.5, which are processed in an automated matter. The goal of this process is to achieve a complete map, which also includes pixels with e.g. less advantageous angular constellations including glint affected pixels. To calculate the metrics, all parameters were extracted and averaged from each flight within a radius of 8 m around the respective sampling positions. A distinction of the water depth was made again for the methods PLS and RF. The comparison of the methods shows that ANN and CNN perform better than PLS and RF, although no depth-dependent models were used here. The scatterplots of ground truth measurements and estimated TSS concentrations in Fig. 7.14 reveal that the methods PLS and CNN tend to slightly overestimate the values in this case. The mosaics calculated using the RF

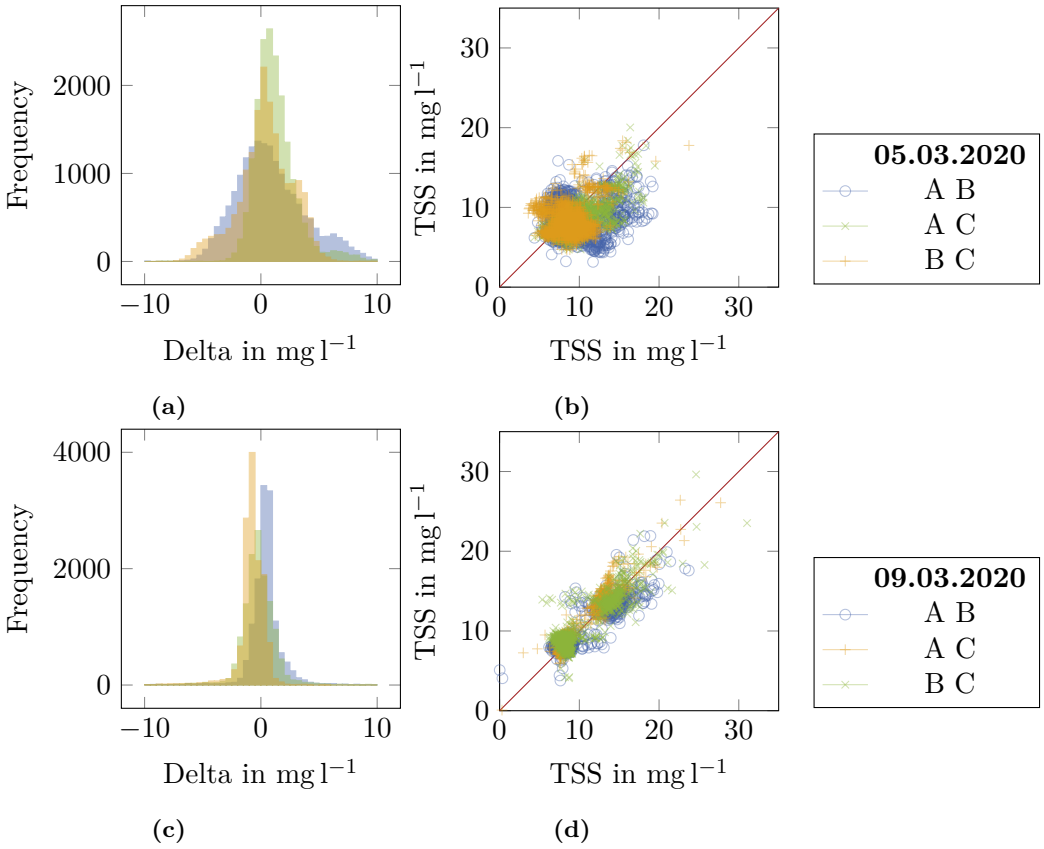

Figure (7.13) Pixel-wise spatial comparison of the flights acquired at the first campaign day under variable cloud cover (upper row) and the third campaign day with clear sky conditions (lower row). The histograms show the calculated delta between each two flight plan configurations and are limited to a range from $-10\,\mathrm{mg\,l^{-1}}$ to $10\,\mathrm{mg\,l^{-1}}$. The right panels show the scatter plot between each two flight plan configurations. The plotted data is limited to $\pm 3\sigma$ and only each tenth point is plotted.

estimated parameters are not shown due to high spatial noise among other spatial artifacts which are not visible in the results using the other methods. These problems of the RF can be attributed to the poor performance of this method to generalize well for the various effects on the spectra like sun glint.

Qualitative Evaluation

In addition, the quantitative evaluation of the data with reference values is followed by a visual qualitative evaluation of the mosaics and methods. Comparing the three mosaics in Fig. 7.14 reveals large spatial differences in addition to the variations in the scatter plots. It is obvious that the methods not only have different absolute offsets, but also different influences of bathymetry (cf. Fig. 5.5) on the results. For PLS this effect has to be corrected in a further step using bathymetric data and own models for different depths (see Fig. 7.15).

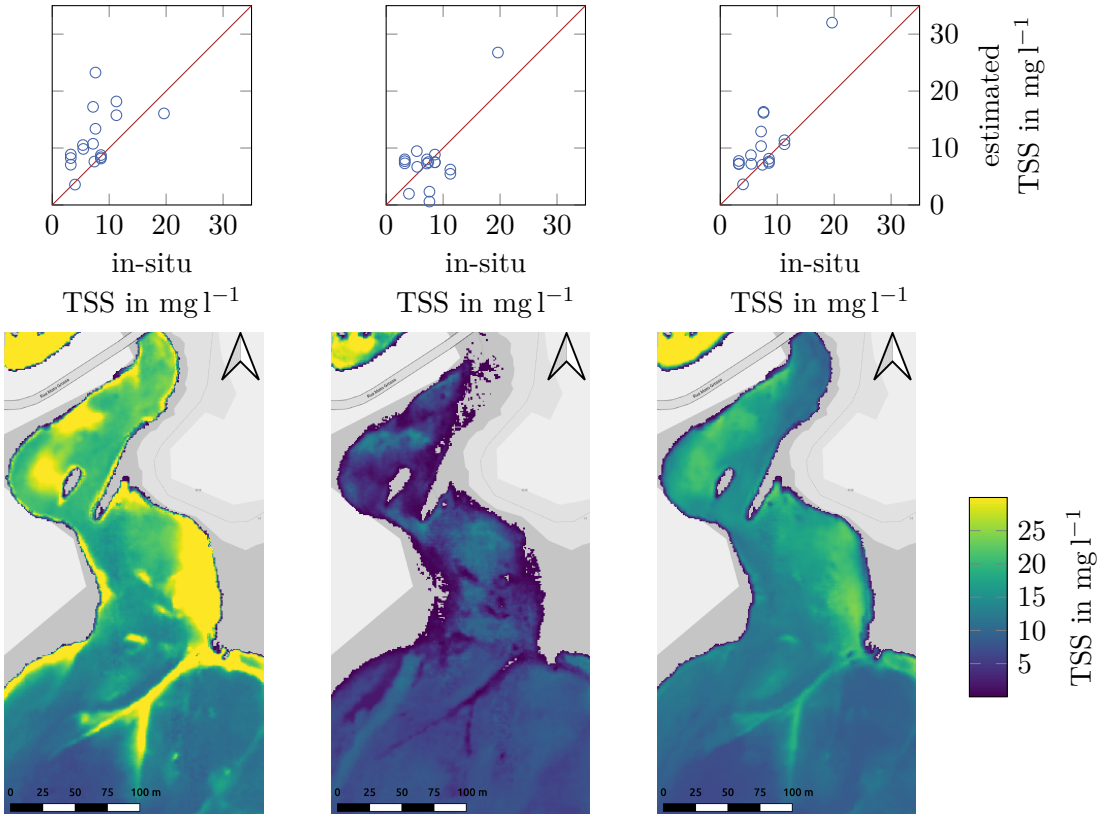

(a) PLS. **(b)** ANN. **(c)** CNN.

Figure (7.14) Visualization of the TSS estimation results as scatter plots and parameter maps for different machine learning algorithms. The scatter plots were created using the measured reference values and values extracted from the results at the corresponding positions. The methods PLS and CNN tend to slightly overestimate the TSS concentration. The map generated using the data from the ANN shows an inverse behavior for shallow water compared to the other methods.

Even though blending algorithms have reduced the hard edges by blending the different models, artifacts of the bathymetry are still visible in the data. A significant reduction of bathymetric influences can be seen when using a CNN. ANN in comparison with the methods PLS and CNN behaves however differently and in parts inversely. The influences of the bathymetry are almost not recognizable here and in contrast to the other methods now clearly lower estimates of the TSS content are shown in places with particularly shallow water than in adjacent deeper areas. In the southwestern part of the map in Fig. 7.14b the course of the old river (cf. Fig. 7.15c or Fig. 5.5b) with deeper water is now visible through the elongated structure with slightly elevated TSS values. In the northern part the model estimates very low values, or partly negative values which are filtered out.

Due to very low concentrations of the in-situ measured parameter chl-a, it was not evaluated quantitatively. However, during the last two days of the campaign, a slightly increased concentration was measured and therefore parameter estimations are shown here without

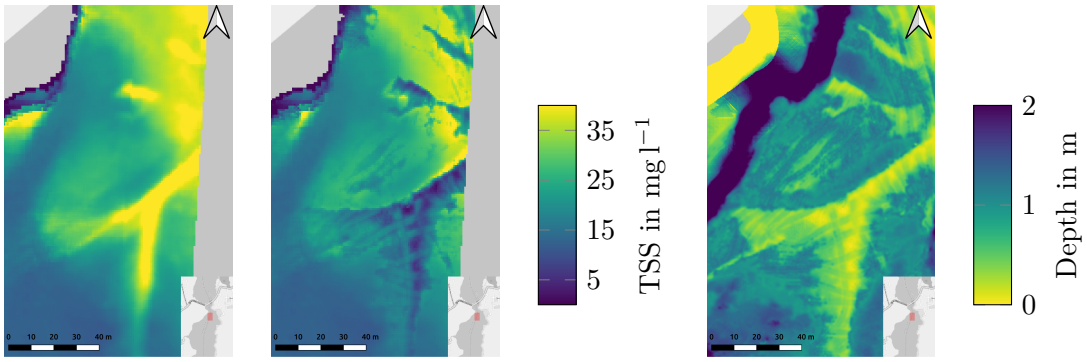

(a) Weighted mean. **(b)** Depth blended. **(c)** Bathymetry.

Figure (7.15) Comparison of a mean weighted result (a) and a map (b) where the water depth was taken into account for map generation. The parameters were estimated using a PLS model. In (c) the corresponding bathymetry is shown.

a quantitative evaluation. The chl-a concentration of the two mosaics in Fig. 7.16 were estimated using a PLS model trained with simulated data similar to the models to estimate TSS in this chapter. In Fig. 7.16a the corresponding parameter map to the data of Fig. 7.14 is shown. The mosaic clearly shows the low concentrations, although the mosaic has high spatial noise and in some cases the model estimates negative values. A chl-a mosaic of another day of the campaign (see Fig. 7.16b) was calculated and corresponds to the TSS map shown in Fig. 7.17. Clearly visible is a plume of higher chl-a concentration extending from north to south. Since no measurements were made within the plume, the estimated values cannot be validated absolutely.

7.5 Summary

The hyperspectral images acquired with the spectral sensor system form the basis for the estimation of water quality parameters such as TSS and chl-a. This chapter first discussed the measured spectra and showed the spectral variation between different areas of the observed water body. These variations are caused by the spatially changing concentration of the water constitutions in the study area. But also within a single image sun glint and cloud shadow affect the spectra. In addition, this chapter showed adverse constellations of

Table (7.5) Evaluation of the final parameter maps. The models were trained with simulated spectra. The mean absolute error in $\mathrm{mg\,l^{-1}}$ is given for the best method using either the raw spectra (D0) or the first derivative (D1). The methods PLS and RF used different models for different water depths.

PLS D0	RF D1	ANN D1	CNN D1
4.4	4.7	3.3	3.5

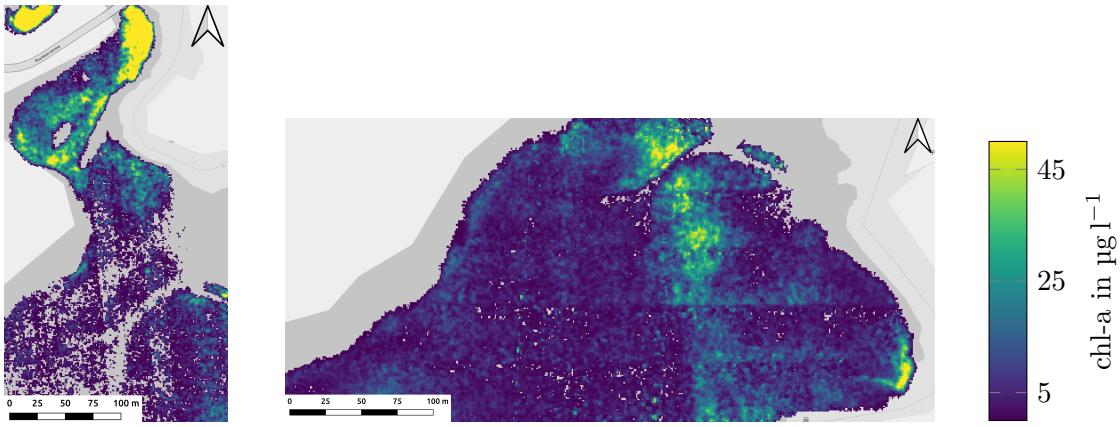

(a) Flight plan A. **(b)** Flight plan B.

Figure (7.16) Chl-a maps of campaign day 5. The maps are generated using a PLS model. The higher values in (b) also match the spatial distribution of TSS in Fig. 7.17.

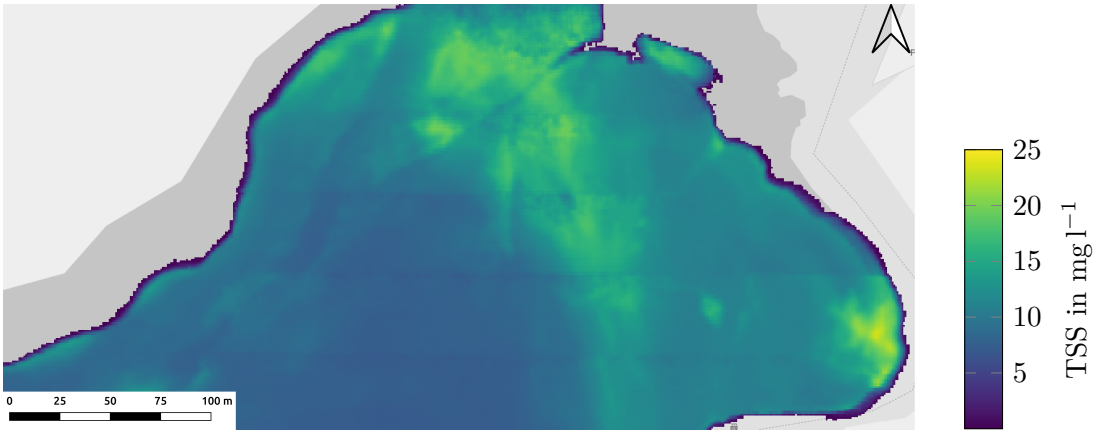

Figure (7.17) Estimated TSS concentration using the CNN model. The map shows the results for the data of flight plan type B acquired on the fifth day of the campaign. The spatial distribution of the higher TSS values is also visible as higher chl-a values in Fig. 7.16b.

sun, clouds and sensor system and describes the automated pre-processing of the spectra. Since the number of reference data collected in this work were not sufficient to train machine learning models, simulated data were used. The focus in this work is on the estimation of the TSS concentration. Various parameters, including the water depth, were varied to generate the simulated data. However, only the generated spectra and corresponding TSS values were used as input parameters for training the estimation models.

Five different methods were used to estimate the TSS concentration from spectral reflectance: Band Ratio (BR), Partial Least Squares Regression (PLS), Random Forest (RF), Artificial Neural Network (ANN) and Convolutional Neural Network (CNN). Based on the simulated data sets the optimal parameter settings for each method were determined and fixed for the subsequent analyses. The machine learning methods were tested with scaled and unscaled

data and also using the preprocessed spectra and their first derivative. In a first step the trained models were evaluated using a separate data set of simulated spectra. The evaluation of the models trained with simulated data showed that BR does not perform well at all. Except for RF, the machine learning models achieved better results using the first derivative. At this point RF performed best, closely followed by the ANN model.

Subsequently, the models trained with simulated data were used to estimate parameters using selected reference spectra which were acquired during the field campaign. The evaluation step used corresponding turbidity in-situ measurements and laboratory analyses of the TSS concentration in water samples. Here it was shown that the use of differentiated models with depth dependent training (PLS and RF) provide an improved accuracy compared to models that have to infer the influence of water depth on the measured spectra in the model itself based on the spectra (ANN and CNN). At this point, the differences in the results between the methods are smaller, and the CNN gives better results on the real data than on the simulated data.

In the next step, parameter mosaics were created. First, the developed method for the use of spatial redundancy by calculating a weighted mean per ground pixel was described and then further steps for the optimization of the mosaics were presented. These included cropping of strongly glint affected parts of the images and a developed semi-automatic method to reduce the influence of cloud shadow caused deviations. Finally, the individual steps of the mosaic calculation and the mosaics themselves were evaluated qualitatively and quantitatively using the reference data.

The calculated mosaics showed that using a weighted mean to calculate the single ground pixels enhances the result in terms of less spatial noise. The cropping of glint affected parts of the image further decreased the spatial noise.

A semi automatic method was developed to reduce the influence of falsely allocated irradiance measurements to ground pixels in case of variable cloud cover. It showed good results by reducing the error due to overestimation of parameters in the case that ground pixels were falsely allocated with irradiance measurements of cloud shadow.

A spatial comparison of large areas which were first illuminated by diffuse light under cloud cover and after this directly by sunlight reinforced the necessity of using the continuous measurement of the irradinace including the automatic correction of the inclination of the irradiance spectrometer caused by the movements of the UAV.

Another spatial comparison was possible due to multiple spatially overlapping flights on each of two campaign days. This comparison showed a good repeatability of the parameter estimation. However, higher variance due to strong variations in cloud cover is still visible in the results.

The quantitative evaluation of the methods based on the mosaics revealed that PLS and RF perform worse than on the strongly preselected reference data. In contrast, ANN and CNN still perform similarly in the evaluation using the reference spectra. This shows that

these models can probably handle the variable water depths and further ambient influences without providing any additional information to the model.

This assumption is reinforced by the qualitative comparison of the maps. Here it was shown that the prevailing shallow water depth is reflected differently in the results. PLS showed a particularly strong dependence on water depth which makes it necessary to mask shallow areas in the map or to use corresponding depth dependent models which makes a further blending step necessary. While the influence of the bathymetry is clearly reduced in the ANN and CNN models, it can be seen that the estimation using the ANN is partly inverse in comparison to the other methods, whereby shallow areas show a lower TSS estimation than adjacent deeper areas.

The chl-a concentration for the data of two flights was estimated using a PLS model trained with simulated data similar to the models to estimate TSS in this chapter. In general, the mosaics show low concentrations and have a high spatial noise. One mosaic shows a plume of higher chl-a concentration extending from north to south. However, due to very low concentrations of the in-situ measured parameter chl-a in general, and unavailable measurements in this plume, it could not be validated and evaluated quantitatively.

7.6 Discussion

The UAV borne multi-sensor system (see Chap. 4) and the developed methods to process the spectral data presented in this chapter proved to be suitable for estimating the water quality parameter TSS. Special focus was put on automating the process from data acquisition to the final parameter map as far as possible and that interactions with the process flow are possible even without expert knowledge. The result for the user is a parameter map of the area under investigation. It should be emphasized here that the models for parameter estimation were trained completely with simulated data using the WASI software. Thus, it could be shown by the evaluation that the models generalize well to different weather conditions and parameter ranges. In the following, some of the results obtained are shortly discussed.

A comparison of the used parameter estimation methods using the mean absolute error in the tables Tab. 7.3, Tab. 7.4 and Tab. 7.5 shows that the methods perform differently on the simulated and real data. For example, the results with RF are worse for the real data than for the simulated data. In contrast, the results of CNN are worse for simulated data than for real data. Possible reasons for this could be, for example, that the model of RF does not generalize well. That RF cannot make use of the high spectral resolution was also shown in [52] in the context of estimating chl-a concentrations.

A quantitative comparison of the obtained results is especially possible with research presented in [57]. There, under similar conditions, data was collected with the same camera also carried by a UAV of a peri-urban stream. They used PLS to estimate the TSS con-

centration and achieved an RMSE of $6.4\,\mathrm{mg\,l^{-1}}$. The methods used here achieve an RMSE of $4.1\,\mathrm{mg\,l^{-1}}$ for ANN and $5.8\,\mathrm{mg\,l^{-1}}$ for CNN when evaluating the final maps. Although no real data were used to train the models in this work, the RMSE for PLS is only slightly worse than in [57] with a value of $6.6\,\mathrm{mg\,l^{-1}}$.

While PLS and RF are not able to model bottom reflectance without further knowledge, it could be shown in the context of this work that ANN and CNN can partially infer this to a certain extent. Although the ANN and CNN perform better in general, a reason for the inverted effect of small water depth in the results of the ANN compared to CNN could not be finally identified. One possibility is the different number of training epochs and the different structure of the two methods. However, larger values of TSS in the ANN based estimations are observed along the course of the old river which is still present in the bathymetry. This is most likely correct, as the main water flow follows this course. Due to missing in-situ samples along this area, it is not possible to further evaluate this.

The spatial comparison of the methods shows the good repeatability of the measurements but also reveals still existing influences due to changing cloud cover. In particular, the estimated parameters obtained under diffuse illumination in cloud shadow suggest that the physical processes prevailing there are not fully covered by the trained models or even by the simulated data. However, by applying the developed methods for mosaicking, which use the high redundancy especially along the flight direction, these effects (sun glint and cloud shadow) could be clearly reduced. This demonstrated that the system can be used even under variable cloud cover. Another method to reduce surface effects is the inversion of adapted analytical models as it is presented in [109]. However, their method could not reliably reduce all surface effects and needed more input parameters and expert knowledge of the user compared to the methods developed in this work.
In addition to the good repeatability of the measurements, it can also be assumed that the methods and models can be applied to other inland water bodies. This can be explained by the fact that the models were trained exclusively with simulated data and the software used (WASI [35]) was mainly developed for European waters. In the context of this work, the application was made to a water reservoir in South America.

In general, the qualitative comparison of the mosaics concerning spatial noise and existing angle-dependent effects shows that the methods developed here provide smoother and probably more reliable results than comparable studies (cf. [92, 84, 148]). However, the qualitative comparison of the PLS, ANN and CNN methods showed that there are spatial differences in the results which are not revealed in the numerical comparison. The differences could have been influenced by the method but also by the parameters chosen to train the models. To be able to explain these effects, more reference data are especially necessary

From a user's point of view, it should be mentioned that the measured suspended matter concentrations are not only due to the sediment input into the water body. Increased concentrations can also be explained, for example, by the resuspension of sediment in shallow waters [149].

Furthermore, the estimated concentrations are always integrated along the water column. It is therefore not possible to determine the depth at which the measured concentration is present. The water depth up to which the backscattered sunlight has an influence on the measured signal is also directly related to the prevailing conditions such as the concentrations of the water quality parameters as well as the condition of the water surface [150, 32, 13]. Fig. 5.5a, which visualizes the relationship between secchi disk depth and water turbidity on the basis of measurements, can give a first impression.

CHAPTER 8

Summary

In this work, a multimodal sensor system consisting of a thermal camera, a hyperspectral camera and an irradiance spectrometer was integrated on a small UAV. For this, the spectral sensors were individually calibrated and cross-calibrated to be able to directly measure the remote sensing ratio (see Chap. 4) which is then used to estimate water quality parameters. The successful application of the system was demonstrated with several data sets acquired during a field campaign in March 2020 at the Passaúna reservoir, located in the west of Curitiba, Brazil (see Chap. 5). In Chap. 6 it was shown that the thermal camera together with the developed methods is suitable to map the water surface temperature. The spectral data and the developed methods to process the hyperspectral images to get image mosaics of the total suspended solids (TSS) concentration were presented in Chap. 7. In the following, the results of the individual chapters are taken up again and put into relation to current research.

Sensor System and Calibration Methods

In Chap. 4 the UAV and the integrated sensor system were initially presented before focusing on the calibration of the spectral sensors. Based on the general methods for the calibration of spectrometers, the necessary adaptations for the calibration of the hyperspectral camera were explained. After this, the cross calibration of both sensors was carried out. These cross calibrated spectral sensors then enable the direct measurement of the remote sensing ratio which is later used for parameter estimation. Finally, the developed method to synchronize the data of the spectral sensors with the navigational data of the UAV allows the inevitable inclination correction of the irradiance measurements. In the following, the relevant results of the chapter are presented and discussed.

The spectrometer could be calibrated reliably according to the established methods for calibration. The dark current was modeled as a function of temperature and integration time and can then be corrected. The nonlinearity of the sensor was determined in the

laboratory using a luminance standard and can also be corrected by a polynomial. Using lamps with known spectral signatures, the wavelength of each channel was calibrated.

Since the hyperspectral camera does not have an internal thermometer, modeling the dark current (DC) was not possible. Therefore, the DC was only investigated. If no DC measurement is available, a constant DC value of 2 DN can be assumed. The nonlinearity had to be determined individually for each channel to be able to correct this effect reliably. In contrast to other research (see [57, 111]), where the camera is operated only in the linear range, this represents an added value, since fewer spectra have to be discarded during the evaluation. The adapted method is suitable for regularly checking the wavelength calibration of the sensor. Since the hyperspectral camera was overhauled by the manufacturer, no improvement could be achieved compared to the factory calibration. To precisely calibrate the wavelength scale, a monochromator should be used (see [31, 57]). As with using a monochromator the low spectral resolution of the hyperspectral camera would not produce overlapping features in the measured spectra and therefore enable a better determination of the center wavelengths of each channel. A similar pattern compared to the observed vignette and residual pattern was also found in other works (see [110, 112, 121]) and could be caused by a coating of a beam splitter [111]. The effect was corrected by a pixel and channel dependent factor. Instead of an absolute calibration of the radiance and irradiance values, a cross calibration between the sensors was performed.

After calibration, it was found that reflectance standards should be used with care in outdoor environments as ambient effects like shadowing or hardly visible reflections onto the reference panel affect the measurements. This applies especially to flexible reflectance tarps when folded for transport. The remaining wrinkles after unfolding in the field can lead to deviations of up to 20 percent from the mean, which would directly affect the calculated reflectance spectra.

Due to the missing synchronization between the navigational data of the UAV and the spectral sensor system, a method for synchronization was developed that uses the acquired irradiance measurements and navigational data in combination with Lambert's cosine law. As this method is data driven, it is a valuable approach when data are not synchronized.

Finally, the cross calibrated sensors enable the direct measurement of the remote sensing ratio which is later used for the estimation of water quality parameters like the total suspended solids (TSS) concentration.

Water Surface Temperature

Remote sensing of the water surface temperature using the thermal camera integrated on the UAV was covered in Chap. 6. First, the characteristics of the thermal camera were presented. Then, data driven methods to correct these effects during post processing and to generate mosaics of the thermal images were developed.

The georeferencing of the images of both sensors, thermal and hyperspectral, was carried out assuming a nadir image using the intrinsic calibration parameters of the respective camera and the pose of the copter at the time of acquisition. As the initial georeferencing of the images of both sensors showed geometrical shifts between the flight lines, an image based method to reduce these offsets was developed. The geometrical shift between the flight lines was determined from several overlapping image pairs from adjacent flight lines. The used images were acquired over land and image features were detected. Subsequently, a mean offset was calculated using several image pairs.

For the correction of the presented characteristics of the thermal camera, data driven methods to estimate the nonuniformity, offsets and drift of the thermal images were developed, which are largely automated. As these methods are applied during post processing, laboratory calibration is not required. The development of suitable post processing methods was necessary, as the characteristics of the camera are strongly variable during the flight, which makes the use of laboratory calibration impossible.

To process the data, all pixels were first classified into water and nonwater to correct for nonuniformity by fitting a polynomial surface. The overlapping areas of neighboring thermal images along the flight line were then used to correct for existing large offsets between the frames and a general temperature drift. After this, the radiometry of adjacent flight lines was aligned using the existing overlap. Finally, an image mosaic of all individually corrected frames was created by weighted averaging, taking into account the distance of each pixel to the center of the image.
Applying these corrections, the effects of the sensor characteristics were reduced to a minimum. While the temperature range of the raw data of all water pixels was over 15 °C this could be reduced to 2 °C in the final mosaics, representing the natural variation. These mosaics reveal the fine structures of the spatial variation of the water surface temperature and correspond to the expected range of values (cf. in-situ temperature measurements in Sect. 5.2).

To reference the temperature of the thermal image mosaics the average temperature of all water pixels during processing from raw data to final mosaics was preserved. Another method to reference the data is the use of synchronous in-situ measurements. While using in-situ measurements is preferred as a reliable method, the other method showed that it is possible to achieve a coarse referencing with deviations of less than 6 °C compared to reference measurements. In general, this does not affect the good accuracy for relative temperature measurements within a mosaic, for which a mean absolute error of 0.33 °C was determined in this work. Therefore, in combination with in-situ measurements to reference the data, a reliable mapping of the water surface temperature is possible.

Comparable results to this work were also presented in [114],[116] and [30].
The study area of [114] is a small river that provides a large number of detectable image features and therefore they use feature tracking to compensate drift and a shutter based approach to reduce nonuniformity. This approach is not applicable to our system

as there are not enough stable feature points in the scenes and the temporal variations of the nonuniformity pattern are too large. The mosaic generation was carried out with pixel-wise averaging. In contrast, our developed method uses weighting according to the distance between the pixel and the image center resulting in only little and smooth gradients between overlapping image frames and flight lines. To reference the temperature mosaics they used in-situ measurements.
In [116] an approach was presented to investigate and model all influences of the camera characteristics and the ambiance on the acquired data. They achieved absolute mean deviations of up to 6 °C, which could only be reduced significantly by using in-situ measurements which is comparable to our results. However, there are still larger gradients in their image mosaics caused by the camera characteristics compared to the results achieved with the developed methods in this work.
Good qualitative and quantitative results were also achieved in [30]. They estimated the nonuniformity of the images in the laboratory and applied the corrections to the measurements. Presumably, the use of this preliminary estimation of nonuniformities and application to field measurements is possible due to the slow movement of the system with $1\,\mathrm{m\,s^{-1}}$, reducing a cooling through wind, and mounting the sensor system inside a box which further reduces environmental effects on the camera [141].

Although our results are comparable with other studies, the data driven approach developed here allows a high degree of automation and is therefore also applicable for nonexperts. Especially, the use of the pure data based correction of the influences represents a significantly lower effort compared to the complete modeling of all effects as e.g. in [116] where still residual effects are visible caused by an insufficient correction of the single images.

Spectral Data and Parameter Estimation

Using the calibrated spectral sensors (see Chap. 4), hyperspectral reflectance images were acquired during the measurement campaign at the drinking water reservoir Passaúna close to Curitiba, Brazil. These data were used in Chap. 7 to demonstrate and evaluate the application of the system with the goal of largely automated mapping of the total suspended solids (TSS) concentration. A flow chart of the developed processing pipeline is visualized in Fig. 7.8.
This chapter first presented the acquired data and their specifics, such as possible problems under changing irradiance and explained the automated data cleansing. As generalizing machine learning methods allow the processing of spectral data even by operators without deep expert knowledge, they were chosen in this work. Due to the lack of a large training data set which is inevitable for the application of machine learning (ML) techniques, reflectance spectra with corresponding reference values for the TSS concentration were simulated using the software WASI. A similar concept was also presented in [70] where simulated data were used within the framework of the estimation of the chlorophyll concentration using ground based spectral reflectance data. A special focus during the generation of

the simulated data was put on adding variations of ambient effects like sun glint and the water depth. Using these simulated data, different ML methods such as Partial Least Squares Regression (PLS), Random Forest (RF), Artificial Neural Networks (ANN) and Convolutional Neural Networks (CNN) were trained and the models were then applied to the real data to estimate the TSS concentration. The focus on the estimation of the total suspended solids (TSS) concentration was chosen since for this parameter sufficient in-situ measurements are available for an evaluation. For the data of two flights, the chl-a concentration was estimated using a PLS model trained with simulated data. Due to very low concentrations of the in-situ measured parameter chl-a in general, these mosaics could not be validated and evaluated quantitatively. However, the chl-a maps show the potential of using the system to map parameters other than the TSS concentration.

For the generation of parameter maps, an automatic mapping method was developed which uses the estimated parameters of the single image frames. Using the estimated parameter images is necessary because the raw spectra cannot be averaged due to influences such as glint. On the other hand, the chosen estimation methods consider these effects so that the resulting parameter images can be used for mapping. The developed method takes into account the angle to the sun and the distance to the center for each pixel of the image when calculating a weighted average of the corresponding ground point. It was shown that the resulting spatial noise in the parameter maps was significantly reduced by using the weighted average compared to simple averaging. It was also shown that only the use of dynamic irradiance measurements facilitates reliable data even below clouds. To reduce the influence of glint on the final maps, parts of the images with areas where glint is likely to occur were cropped.
Under constantly changing cloud cover, however, false assignments of irradiance measurements to ground pixels can occur. These misassignments result in the reflectance being incorrectly calculated and thus the estimated parameters being falsified. To reduce this error, a semi-automatic procedure was developed which significantly reduces these influences. While for the case that the irradiance spectrometer is in the shadow and the ground point is in the sun a significant reduction was achieved, for the case that the irradiance spectrometer is in the sun and the ground point in the shadow only minimal improvements could be achieved. One reason for this may be the spectral characteristics, which are not sufficiently covered by the simulated data for this case and no sufficient generalization was achieved using the ML models.
Due to the largely automated handling of the influences of glint and shadow on the data, the developed methods represent a clear advantage over other works that try to model these effects and require expert knowledge of the operator and in some cases use further in-situ measurements (cf. [109]).

The quantitative evaluation found that the trained models provide different results for manually preselected individual spectra compared to the automatically calculated mosaics. The methods PLS and RF gave better results than ANN and CNN for the manually selected reference spectra. This was reversed when evaluating the final parameter mosaics.

Here, ANN and CNN provided better results in the quantitative comparison. The better performance of ANN and CNN in this case is achieved by the good generalizability and the better handling of ambient influences of these ML methods.
The results of the ML methods were also compared to an empirical method, where a Band Ratio (BR) approach was selected as it is a widely used method. As this approach could only achieve reasonable results on manually preselected spectra with little ambient effects like sun glint, this method was not further used.
An examination of the repeatability of the measurements was possible with the help of three overlapping flights on each of two campaign days. This showed good repeatability of the measurements under optimal sunny conditions with only little artifacts in the parameter maps due to changing irradiance.

A quantitative comparison of the obtained results is especially possible with [57]. There, under similar conditions, data of a peri-urban stream was acquired with the same hyperspectral camera also carried by a UAV. They used PLS to estimate the TSS concentration and achieved an RMSE of $6.4\,\mathrm{mg\,l^{-1}}$. The methods used here achieve an RMSE of $4.1\,\mathrm{mg\,l^{-1}}$ for ANN and $5.8\,\mathrm{mg\,l^{-1}}$ for CNN when evaluating the final maps. Although no real data were used to train the models in this work, the RMSE for PLS is only slightly worse than the results in [57] with a value of $6.6\,\mathrm{mg\,l^{-1}}$.

The qualitative evaluation of the parameter maps showed that the methods PLS, ANN and CNN provide different results. RF on the contrary could not produce usable parameter maps at all due to a high spatial noise also present in the individual processed images and was therefore not considered in detail. The discrepancies between the different methods are especially visible at low water depths. While PLS cannot handle low water depths sufficiently and thus needs differentiated models with depth dependent training, the used ANN and CNN models can partially account for the influence of low water depth on the spectra and therefore provide better results.

The qualitative comparison of the mosaics concerning spatial noise and existing angle-dependent effects shows that the methods developed here provide smoother and probably more reliable results than comparable studies (cf. [92, 151, 93, 148]).
The results shown in [92] still show clear gradients between the data of different flight lines which indicates that large angle dependent effects are not corrected or handled in the mapping process. Also, they use only little reference measurements to train their models and correct the hyperspectral images with the use of synchronously acquired ground based spectra which is not necessary with our developed approach.
In [151] the authors use a hyperspectral camera for the mapping of turbidity and chlorophyll but could not achieve good results. Radiometric influences like glint are still visible in their presented maps.
A push broom scanner was used in [93] in combination with semi-analytical and semi-empirical models to map the chlorophyll-a concentration in shallow coastal waters where the results still show strong angle dependent effects in the mosaics.
Good quantitative and qualitative results are achieved for water transparency estimation

in [83] where they used in-situ reference data to train the models. This is contrary to our setup where we used only independent simulated data to train the models.

As a result of this study, it can be said that PLS can deliver good results under optimal conditions with low demands on the computing power and it is also applicable with limited ground truth data. In contrast, ANN and CNN provide more homogeneous parameter maps and better results even under changing irradiation and at low water depths.

CHAPTER 9

Conclusions and Outlook

This work was concerned with the setup of a compact and inexpensive sensor system on a UAV and contributes to current research in the field of automated monitoring of water quality parameters of inland waters. Methods to calibrate the sensors and to process the data to generate maps of water quality parameters were developed and applied to data sets acquired during a field campaign. In the following, the core findings, conclusions and an outlook will be presented. The research questions listed in the introduction (see Chap. 1) will be addressed.

9.1 Conclusions

This thesis is divided in three parts. First, the setup of the system and the calibration of the spectral sensors. Second, the remote sensing of the water surface temperature using the thermal camera. Third, the hyperspectral remote sensing using the cross calibrated hyperspectral camera and the irradiance spectrometer for the estitmation of water quality parameters. Following this partition, conclusions and addressing of the research questions are presented individually for the different parts. Finally, a general conclusion is given on the integrated system. In short, the research questions are the following:

1. Can a low budget multimodal sensor system mounted on a UAV be used for (a) easy data acquisition, and is it possible to (b) automatically process the data to (c) generate consistent and reliable parameter maps?
2. Is it possible to use the system below the cloud cover?
3. Is it possible to use only few ground truth data?

Sensor System and Calibration Methods

Especially for the estimation of water quality parameters like total suspended solids (TSS) the spectral sensors must be calibrated. Without calibration, the varying spectral characteristics of the individual pixels of a hyperspectral (HS) camera can lead to inconsistent data (cf. Fig. 3.1). In Chap. 4 the methods for the calibration of the spectral sensors were presented. The methods used and developed require as few absolute laboratory measurements as possible and thus keep the time and financial effort low. To synchronize the navigational data of the UAV and the spectral measurements, the developed data driven approach uses only data acquired during the field campaign. This synchronization enables the inevitable inclination correction of the irradiance measurements. The calibrated spectral sensor system is able to directly measure the remote sensing ratio which is later used for the estimation of water quality parameters. However, due to the simplified methods and measurement setups, it is not possible to measure absolute values for radiances and irradiances with this system.

The investigation of measurements on reflectance standards revealed that reference measurements could be biased. The bias depends e.g. on the acquisition geometry causing for example reflections from the UAV itself on the reference panel. Reflectance tarps on the other hand can have wrinkles due to folding during transport which also adds a bias pattern to the reference measurements. It can be concluded, that using a calibrated spectral sensor system to directly measure the remote sensing ratio is beneficial compared to the traditional method of using reflectance standards, especially for UAV applications under intermittent clouds.

Research question 1a can be answered with yes since for the measurement of the remote sensing ratio only a reliable cross calibration between the hyperspectral camera and irradiance spectrometer is necessary, which was achieved by the developed methods. Especially, the operation of UAVs is getting easier due to the fast advancing developments of this technology so the acquisition of data can be done by briefly trained technical staff in the meantime.

Water Surface Temperature

The analysis of the thermal data showed that the actual signal is overlaid by strong sensor characteristics. The observed influences are a general drift of the temperature, large offsets between individual frames and a strong nonuniformity within the frames. The correction of the nonuniformity was particularly challenging since it varies strongly during a flight, as e.g. a changing wind direction affects the temperature distribution inside the camera which is not protected against these influences. Therefore, it cannot be calibrated in the laboratory. However, the developed methods allow an automated processing of the data to reduce remaining artifacts to a minimum. The resulting temperature maps can achieve absolute deviations of less than 6 °C without the use of in-situ measurements, which is similar to the results of other research. Measured temperature differences within the temperature

maps, however, deviate on average only by 0.33 °C from reference measurements. It follows that the parameter maps allow reliable measurements by using in-situ measurements to absolutely reference the maps as it is common practice in current research. However, since water surface temperature can vary by a few degrees Celsius over a day, care must be taken when acquiring in-situ measurements for referencing the temperature maps to ensure temporal proximity between in-situ measurement and acquisition of thermal images with the UAV.

Addressing the research questions, research question 1 can be answered as follows: The used thermal camera is easy to use and the automated processing of the data produces consistent and reliable results.
The evaluated data did not show any influence by a changing cloud cover, therefore research question 2 can be answered with yes for the thermal data.
Since only a few in-situ measurements for absolute referencing are necessary for the reliability of the temperature maps, research question 3 can also be answered with yes.

Spectral Data and Parameter Estimation

The processing of spectral data requires more comprehensive methods compared to thermal data since these data are influenced by ambient factors such as changing cloud cover and total reflection of sunlight (sun glint) at the water surface. In order to achieve an automated processing of the data as far as possible, methods for the preprocessing of the spectral data were developed. In a further step, simulated data were used to train machine learning (ML) models (PLS, RF, ANN, CNN) which were then used to estimate water quality parameters of the real data. A developed mapping procedure combined the single parameter images to consistent parameter maps. In this context, it could be shown that the dynamic measurement of irradiance is mandatory for consistent image mosaics, as it is the only way to account for effects such as changing irradiance under intermittent cloud cover.

Although the quantitative results with Random Forest (RF) were in the same range as the other machine learning methods, the parameter maps showed a strong spatial noise which can be attributed to a low generalization, especially for ambient influences on the spectra like sun glint and cloud shadows. It can be concluded that this method is not able to generalize using the simulated data, and therefore, a transfer to the real data is not possible. Especially, the machine learning methods Partial Least Squares Regression (PLS), Artificial Neural Networks (ANN) and Convolutional Neural Networks (CNN) perform well on the real data. The achieved results are comparable to other research while in this work the used models were trained without any in-situ data.

However, influences of the water depth are always visible in the parameter maps. This can be attributed to the low sediment concentration in the water and the bottom substrate influencing the measured spectra in the same regions as the TSS concentration. The comparison of the methods shows that the ML methods ANN and CNN can take this effect

into account much better than the simpler methods due to the better generalization of the models.

The purely numerical comparison also shows that PLS performs worse on the final mosaics than, for example, ANN and CNN, but the differences are not particularly large. Therefore, depending on the application, PLS can achieve good results while only requiring low computing capacity. Empirical methods such as BR, which can also be implemented with multispectral cameras, can also be useful in individual cases because particularly inexpensive hardware can be used. The main disadvantage of empirical methods is the strong adaptation to the local conditions and possibly even a seasonal dependency. By contrast, the models generated in this work with the aid of simulated training data can be assumed to be highly generalizable and easily transferable to other waters.

Due to the low number of reference measurements for the evaluation, a numerical comparison with other research is difficult. Besides the few ground truth measurements, the relatively small range in which the TSS concentrations varied and the very low chl-a concentration make an optimal evaluation of the data difficult.
However, it should be highlighted that this work has completely avoided in-situ measurements for training the models and thus uses completely independent data sets for training the models and evaluating the real data, which is a decisive difference from the majority of the literature, which mostly uses empirical models or models trained with in-situ data or further prior knowledge.

The developed methods are largely automated and provide consistent and reliable maps. To process the data, the operator does not need deep knowledge in this field, so the research questions 1b and 1c can be answered with yes. The only constraint in using the system is the need for the UAV operator to have practical experience.
Based on the results, research question 2 can be answered: The system can be used below cloud cover and intermittent clouds while the parameter maps show few artifacts due to ambient effects.
A comparison with other recent research also shows that the sensor system and the developed methods can achieve similar results. In this work, the developed methods mostly achieve more consistent parameter maps with low spatial noise, and, in some cases, better quantitative results. Therefore, regarding research question 3, it can be concluded that the system can deliver reliable results even without ground truth measurements as only simulated data was used to train the models.

General Conclusions

To sum up, the system is suitable for practical use, and the research questions posed at the beginning can be answered in the affirmative for the system as a whole. Especially, the qualitative analysis of the generated temperature and parameter maps shows the good performance of the system. The high consistency of the maps is remarkable, with only

minor artifacts of the sensor characteristics and ambient influences on the sensors visible in the parameter maps. Thus, the results obtained stand out positively from a large number of similar studies. Weaknesses of the conducted studies, however, are to be seen in the reliability of the quantitative evaluation. Because of the few existing in-situ reference measurements, future work with this system will have to include a robust quantitative evaluation in particular.

Also, the high degree of automation of the system and the data evaluation leads to easy handling. Thus, the developed system stands out from many approaches of current research and makes an important contribution to automated remote sensing of water quality parameters. In practice, however, the short flight time of less than 15 min is a limiting factor for the use of this system.

Possible use cases of the system in the context of monitoring water quality parameters are presented in the following. The system can be used to collect high-resolution data at any time, even within a day, e.g. from areas that are necessary for the numerical modeling of processes in the water. It could be used to map the spatial distribution of parameters around structures to e.g. identify sediment traps and study internal flows. This is a clear added value compared to satellites which provide only data in intervals of days or even weeks with lower spatial resolution. Besides this, the number of usable satellite images is further reduced due to frequent cloud cover. The flexible and fast setup of the system in the field also allows to capture phenomena with diurnal variations like algae blooms with a high spatial and temporal resolution. Finally, the system can also be used to detect parameter gradients and highly dynamic areas, which can be used to optimally determine the positions for in-situ samplings and sensors for long-term monitoring.

9.2 Outlook

Based on the experience gained from the practical use of the system and the findings obtained in the studies, further challenges for future research can be identified. The remaining challenges and outlooks listed below concern the hardware and processing of the data as well as their use.

The biggest added value of a UAV-borne sensor system can be achieved if the flight time is long and thus the area that can be covered is large. With conventional vertical launching multicopters like the one used in this work, this is usually not possible. However, the ongoing development of UAVs in recent years has resulted in vertical take-off UAVs which switch to a flight mode corresponding to that of a fixed wing UAV after take-off. With these versatile UAVs, large-scale data acquisition at still low costs and a high degree of flexibility will be possible soon.

In particular, the collection of sufficient reference data is a critical task for the training and evaluation of parameter estimation methods. Since manual sampling requires additional

personnel in a boat on the water, it makes sense to automate this part as well. Here, autonomously driving boats with in-situ sensors or UAVs that can take water samples in an automated way could be useful [152, 153].

Regarding the thermal camera, the results from [30] show, that with the help of an optimized setup in which the camera is protected from as many environmental influences as possible by an additional housing, data with good quality can be acquired and its potential should be investigated in detail in further research. Also, the use of the thermal camera with an additional external shutter which is heated could be beneficial. As it could provide a more reliable reference than the internal shutter during flight and thus allows better correction of nonuniformity and drift.

The spectral sensor system could be improved by the use of irradiance sensors that are tailored to UAV applications [154] and are partly available for multispectral cameras (e.g. [155]).

A special challenge in the processing of image data acquired over water is their exact georeferencing, where traditional image-based methods are usually not applicable. For further work, it is therefore imperative to be able to measure the exact orientation of the camera to georeference the images correctly.

To further reduce ambient influences like sun glint affecting the measured spectra, the optimal orientation of the hyperspectral camera should also be investigated, just as optimal orientations have been determined for point spectrometers in the past.

Under changing irradiance, some minor artifacts still exist in the parameter maps. For this purpose, further methods for their optimal correction have to be explored.

In this work, the spectral data were used only to estimate and evaluate the parameter TSS. A first attempt of mapping the chl-a concentration was shown but not evaluated. Future studies should therefore extend the developed methods to other relevant water quality parameters and evaluate them accordingly. Also, the system should be tested on different types of waters to confirm the applicability for different scenarios.

Since a system has been developed within the framework of this work that is suitable for practical use, possible applications should be investigated in further studies. The easiest to implement is the search for optimal positions for taking water samples [156] or the positioning of in-situ probes for long-term measurements. Studies of phenomena that vary within a day, such as algal blooms [15], are also particularly interesting. In the context of management concepts for water reservoirs, for example, the parameter maps can serve as a contribution to the setup and validation of numerical models and thus support e.g. sediment management.

In general, the system is not limited to the sole use of remote sensing of inland waters. For example, the data could be used for validation of e.g. satellite data, as it was implemented in [157] with multispectral cameras. The integrated sensors can also be used for mapping birds and other animals on the water or at the shore where also the predominant vegetation

is of interest. In the catchment of a water reservoir, the hyperspectral camera could be used to determine vegetation indices or even map the distribution of individual plant and tree species. With this system this has already been tested in [158] for a small data set with the aim of classifying different crops on an agricultural farm.

To sum up, the system performs well for the presented studies and the results are promising for a variety of future works where the flexible acquisition of high resolution remote sensing data is needed. Especially, when satellite data does not offer the necessary flexibility and spatial resolution, and airborne systems are not economically viable. Nevertheless, more research is necessary to improve the system and further automate the processing with the aim of achieving a market ready product which then will make a decisive contribution to the management of surface waters.

List of Figures

List of Tables

Bibliography

[1] UNESCO World Water Assessment Programme. *The United Nations World Water Development Report 2020: Water and Climate Change*. UNESCO, Paris, 2020.

[2] Paul R. Hunter, Alan M. MacDonald, and Richard C. Carter. Water Supply and Health. *PLOS Medicine*, 7(11):e1000361, November 2010.

[3] Anna Mercè Rio Carrillo and Christoph Frei. Water: A key resource in energy production. *Energy Policy*, 37(11):4303–4312, November 2009.

[4] Arun Lal Srivastav, Rajni Dhyani, Manish Ranjan, Sughosh Madhav, and Mika Sillanpää. Climate-resilient strategies for sustainable management of water resources and agriculture. *Environmental Science and Pollution Research*, 28(31):41576–41595, August 2021.

[5] Edward B. Barbier. Water and Economic Growth. *Economic Record*, 80(248):1–16, 2004.

[6] UN DESA. The Sustainable Development Goals Report. Technical report, New York, July 2022.

[7] Directive 2000/60/EC of the European Parliament and of the Council of 23 October 2000 establishing a framework for Community action in the field of water policy, October 2000.

[8] Claudia Copeland. Clean Water Act: A Summary of the Law. 1948.

[9] Stephan Fuchs, Stephan Hilgert, Klajdi Sotiri, Franz Nestmann, Frank Seidel, Wendy Gonzalez Otero, Stefan Hinz, Andreas Schenk, Jens Kern, Fachbereich Siedlungswasserwirtschaft und Wassergütewirtschaft Karlsruher Institut für Technologie, and Karlsruhe Institut für Photogrammetrie und Fernerkundung. MuDak-WRM - Multidisciplinary data acquisition as the key for a globally applicable water resource management. Technical report, Karlsruhe, 2021.

[10] Blake A. Schaeffer, Kelly G. Schaeffer, Darryl Keith, Ross S. Lunetta, Robyn Conmy, and Richard W. Gould. Barriers to adopting satellite remote sensing for water quality management. *International Journal of Remote Sensing*, 34(21):7534–7544, November 2013.

[11] Katja Dörnhöfer and Natascha Oppelt. Remote sensing for lake research and monitoring – Recent advances. *Ecological Indicators*, 64:105–122, May 2016.

[12] Deepak Mishra, Igor Ogashawara, and Anatoly Gitelson. *Bio-Optical Modeling and Remote Sensing of Inland Waters*. May 2017.

[13] Curtis Mobley and IOCCG. The Oceanic Optics Book. 2022.

[14] R. H. Rogers, N. J. Shah, V. E. Smith, and J. B. Mckeon. Computer Mapping of Water Quality in Saginaw Bay with LANDSAT Digital Data. Technical Report E76-10124, January 1976.

[15] Katja Dörnhöfer, Philip Klinger, Thomas Heege, and Natascha Oppelt. Multi-sensor satellite and in situ monitoring of phytoplankton development in a eutrophic-mesotrophic lake. *Science of The Total Environment*, 612:1200–1214, January 2018.

[16] Igor Ogashawara, Christine Kiel, Andreas Jechow, Katrin Kohnert, Thomas Ruhtz, Hans-Peter Grossart, Franz Hölker, Jens C. Nejstgaard, Stella A. Berger, and Sabine Wollrab. The Use of Sentinel-2 for Chlorophyll-a Spatial Dynamics Assessment: A Comparative Study on Different Lakes in Northern Germany. *Remote Sensing*, 13(8):1542, January 2021.

[17] Milad Niroumand-Jadidi, Francesca Bovolo, and Lorenzo Bruzzone. Water Quality Retrieval from PRISMA Hyperspectral Images: First Experience in a Turbid Lake and Comparison with Sentinel-2. *Remote Sensing*, 12(23):3984, January 2020.

[18] Fang Shen, Haiyang Zhao, Qing Zhu, Xuerong Sun, and Yinnian Liu. Chinese Hyperspectral Satellite Missions and Preliminary Applications of Aquatic Environment. In *2021 IEEE International Geoscience and Remote Sensing Symposium IGARSS*, pages 1233–1236, July 2021.

[19] Mariano Bresciani, Claudia Giardino, Alice Fabbretto, Andrea Pellegrino, Salvatore Mangano, Gary Free, and Monica Pinardi. Application of New Hyperspectral Sensors in the Remote Sensing of Aquatic Ecosystem Health: Exploiting PRISMA and DESIS for Four Italian Lakes. *Resources*, 11(2):8, February 2022.

[20] Leif G. Olmanson, Patrick L. Brezonik, and Marvin E. Bauer. Airborne hyperspectral remote sensing to assess spatial distribution of water quality characteristics in large rivers: The Mississippi River and its tributaries in Minnesota. *Remote Sensing of Environment*, 130:254–265, March 2013.

[21] Jong Cheol Pyo, Mayzonee Ligaray, Yong Sung Kwon, Myoung-Hwan Ahn, Kyunghyun Kim, Hyuk Lee, Taegu Kang, Seong Been Cho, Yongeun Park, and Kyung Hwa Cho. High-Spatial Resolution Monitoring of Phycocyanin and Chlorophyll-a Using Airborne Hyperspectral Imagery. *Remote Sensing*, 10(8):1180, August 2018.

[22] Syed Moosa Ali, Anurag Gupta, Mini Raman, Arvind Sahay, Gunjan Motwani, Pradipta R. Muduli, Aswathy Vijaya Krishna, and Anima Tirkey. Improved estimates of bio-optical parameters in optically complex water using hyperspectral remote sensing data. *International Journal of Remote Sensing*, 42(8):3056–3073, April 2021.

[23] Max Gerhards, Martin Schlerf, Kaniska Mallick, and Thomas Udelhoven. Challenges and Future Perspectives of Multi-/Hyperspectral Thermal Infrared Remote Sensing for Crop Water-Stress Detection: A Review. *Remote Sensing*, 11(10):1240, January 2019.

[24] Julia Kelly, Natascha Kljun, Per-Ola Olsson, Laura Mihai, Bengt Liljeblad, Per Weslien, Leif Klemedtsson, and Lars Eklundh. Challenges and Best Practices for Deriving Temperature Data from an Uncalibrated UAV Thermal Infrared Camera. *Remote Sensing*, 11(5):567, January 2019.

[25] Roghieh Eskandari, Masoud Mahdianpari, Fariba Mohammadimanesh, Bahram Salehi, Brian Brisco, and Saeid Homayouni. Meta-analysis of Unmanned Aerial Vehicle (UAV) Imagery for Agro-environmental Monitoring Using Machine Learning and Statistical Models. *Remote Sensing*, 12(21):3511, January 2020.

[26] Mercedes Vélez-Nicolás, Santiago García-López, Luis Barbero, Verónica Ruiz-Ortiz, and Ángel Sánchez-Bellón. Applications of Unmanned Aerial Systems (UASs) in Hydrology: A Review. *Remote Sensing*, 13(7):1359, January 2021.

[27] Helge Aasen, Eija Honkavaara, Arko Lucieer, and Pablo J. Zarco-Tejada. Quantitative Remote Sensing at Ultra-High Resolution with UAV Spectroscopy: A Review of Sensor Technology, Measurement Procedures, and Data Correction Workflows. *Remote Sensing*, 10(7):1091, July 2018.

[28] Jens Kern and Andreas Schenk. A MULTI-MODAL SYSTEM FOR MONITORING OF WATER QUALITY - SETUP AND FIRST RESULTS FROM PASSAUNA RESERVOIR. In *Anais Do XIX Simpósio Brasileiro de Sensoriamento Remoto*. INPE, April 2019.

[29] Ji-Yeon Baek, Young-Heon Jo, Wonkook Kim, Jong-Seok Lee, Dawoon Jung, Dae-Won Kim, and Jungho Nam. A New Algorithm to Estimate Chlorophyll-A Concentrations in Turbid Yellow Sea Water Using a Multispectral Sensor in a Low-Altitude Remote Sensing System. *Remote Sensing*, 11(19):2257, January 2019.

[30] Abolfazl Irani Rahaghi, Ulrich Lemmin, Daniel Sage, and David Barry. Achieving high-resolution thermal imagery in low-contrast lake surface waters by aerial remote sensing and image registration. *Remote Sensing of Environment*, 221:773–783, February 2019.

[31] Johannes F. S. Brachmann, Andreas Baumgartner, and Karim Lenhard. Calibration procedures for imaging spectrometers: Improving data quality from satellite missions to UAV campaigns. In *Sensors, Systems, and Next-Generation Satellites XX*, volume 10000, page 1000010. International Society for Optics and Photonics, October 2016.

[32] John T. O. Kirk. *Light and Photosynthesis in Aquatic Ecosystems*. Cambridge University Press, Cambridge, UNITED KINGDOM, 2010.

[33] Richard L. Miller. *Remote Sensing of Coastal Aquatic Environments: Technologies, Techniques and Applications / Ed. by Richard L. Miller ...* 2005.

[34] Laurie Lee Richardson. *Remote Sensing of Aquatic Coastal Ecosystem Processes: Science and Management Applications / Edited by Laurie L. Richardson ...* Springer, 2006.

[35] Peter Gege. WASI-2D: A software tool for regionally optimized analysis of imaging spectrometer data from deep and shallow waters. *Computers & Geosciences*, 62:208–215, January 2014.

[36] R. W. Preisendorfer. Hydrologic Optics. Volume 2. Foundations. Technical report, Honolulu : U.S. Dept. of Commerce, National Oceanic and Atmospheric Administration, Environmental Research Laboratories, Pacific Marine Environmental Laboratory, 1976.

[37] Simon N. Topp, Tamlin M. Pavelsky, Daniel Jensen, Marc Simard, and Matthew R. V. Ross. Research Trends in the Use of Remote Sensing for Inland Water Quality Science: Moving Towards Multidisciplinary Applications. *Water*, 12(1):169, January 2020.

[38] Alan E. Strong. Remote sensing of algal blooms by aircraft and satellite in Lake Erie and Utah Lake. *Remote Sensing of Environment*, 3(2):99–107, January 1974.

[39] Anclré Morel and Louis Prieur. Analysis of variations in ocean color1. *Limnology and Oceanography*, 22(4):709–722, 1977.

[40] G. R. Aiken, D. M. McKnight, R. L. Wershaw, and P. MacCarthy. Humic Substances in Soil, Sediment, and Water. 1985. *Soil Science*, 142(5):323, November 1986.

[41] Mohammad Gholizadeh, Assefa Melesse, and Lakshmi Reddi. A Comprehensive Review on Water Quality Parameters Estimation Using Remote Sensing Techniques. *Sensors*, 16(8):1298, August 2016.

[42] Annick Bricaud, Andre Morel, and Louis Prieur. Absorption by dissolved organic matter of the sea (yellow substance) in the UV and visible domains1. *Limnology and Oceanography*, 26(1):43–53, 1981.

[43] Patrick L. Brezonik, Leif G. Olmanson, Jacques C. Finlay, and Marvin E. Bauer. Factors affecting the measurement of CDOM by remote sensing of optically complex inland waters. *Remote Sensing of Environment*, 157:199–215, February 2015.

[44] Adrian Wagner. *Event-Based Measurement and Mean Annual Flux Assessment of Suspended Sediment in Meso Scale Catchments*. PhD thesis, KIT, Karlsruhe, 2020.

[45] E Al Shaw and John S Richardson. Direct and indirect effects of sediment pulse duration on stream invertebrate assemblages and rainbow trout (Oncorhynchus mykiss) growth and survival. *Canadian Journal of Fisheries and Aquatic Sciences*, 58(11):2213–2221, November 2001.

[46] David Doxaran, Jean-Marie Froidefond, Samantha Lavender, and Patrice Castaing. Spectral signature of highly turbid waters: Application with SPOT data to quantify suspended particulate matter concentrations. *Remote Sensing of Environment*, 81(1):149–161, July 2002.

[47] Susan Kay, John D. Hedley, and Samantha Lavender. Sun Glint Correction of High and Low Spatial Resolution Images of Aquatic Scenes: A Review of Methods for Visible and Near-Infrared Wavelengths. *Remote Sensing*, 1(4):697–730, December 2009.

[48] Nariane Bernardo, Enner Alcântara, Fernanda Watanabe, Thanan Rodrigues, Alisson Carmo, Ana Gomes, and Caroline Andrade. Glint Removal Assessment to Estimate the Remote Sensing Reflectance in Inland Waters with Widely Differing Optical Properties. *Remote Sensing*, 10(10):1655, October 2018.

[49] Charles Cox and Walter Munk. Measurement of the Roughness of the Sea Surface from Photographs of the Sun's Glitter. *JOSA*, 44(11):838–850, November 1954.

[50] Curtis D. Mobley. Estimation of the remote-sensing reflectance from above-surface measurements. *Applied Optics*, 38(36):7442–7455, December 1999.

[51] John D Hedley and Curtis D Mobley. HYDROLIGHT 6.0 ECOLIGHT 6.0. https://www.numopt.com/doc/HE60TechDoc.pdf, 2021.

[52] Philipp M. Maier. *Towards a Generalized Machine Learning Approach for Estimating Chlorophyll Values in Inland Waters with Spectral Data / von Philipp M. Maier*. PhD thesis, Karlsruher Institut für Technologie, Karlsruhe, 2021.

[53] Svante Wold, Michael Sjöström, and Lennart Eriksson. PLS-regression: A basic tool of chemometrics. *Chemometrics and Intelligent Laboratory Systems*, 58(2):109–130, October 2001.

[54] Felix M. Riese and Sina Keller. Supervised, Semi-supervised, and Unsupervised Learning for Hyperspectral Regression. In Saurabh Prasad and Jocelyn Chanussot, editors, *Hyperspectral Image Analysis: Advances in Machine Learning and Signal Processing*, Advances in Computer Vision and Pattern Recognition, pages 187–232. Springer International Publishing, Cham, 2020.

[55] Kenneth A. Sudduth, Gab-Sue Jang, Robert N. Lerch, and E. John Sadler. Long-Term Agroecosystem Research in the Central Mississippi River Basin: Hyperspectral Remote Sensing of Reservoir Water Quality. *Journal of Environmental Quality*, 44(1):71–83, 2015-01/0001-02.

[56] A. Wagner, S. Hilgert, T. Kattenborn, and S. Fuchs. Proximal VIS-NIR spectrometry to retrieve substance concentrations in surface waters using partial least squares modelling. *Water Supply*, 19(4):1204–1211, October 2018.

[57] Christian Josef Köppl. *Hyperspectral Sensing from Unmanned Aerial Systems for Water Quality and Quantity in Terrestrial and Aquatic Systems*. DTU Environment, Kgs. Lyngby, 2022.

[58] Leo Breiman. Random Forests. *Machine Learning*, 45(1):5–32, October 2001.

[59] Philipp M. Maier and Sina Keller. Machine learning regression on hyperspectral data to estimate multiple water parameters. *2018 9th Workshop on Hyperspectral Image and Signal Processing: Evolution in Remote Sensing (WHISPERS)*, pages 1–5, September 2018.

[60] Daniel Andrade Maciel, Claudio Clemente Faria Barbosa, Evlyn Márcia Leão de Moraes Novo, Rogério Flores Júnior, and Felipe Nincao Begliomini. Water clarity in Brazilian water assessed using Sentinel-2 and machine learning methods. *ISPRS Journal of Photogrammetry and Remote Sensing*, 182:134–152, December 2021.

[61] Rabia Munsaf Khan, Bahram Salehi, Milad Niroumand-Jadidi, and Masoud Mahdianpari. Quantification and Mapping of Water Clarity for Freshwater Lakes Using Sentinel-2 Data and Random Forest Regression Model: Application on Finger Lakes, New York. In *IGARSS 2023 - 2023 IEEE International Geoscience and Remote Sensing Symposium*, pages 2890–2893, July 2023.

[62] Aurélien Géron, Kristian Rother, and Thomas Demmig. *Praxiseinstieg Machine Learning mit Scikit-Learn, Keras und TensorFlow: Konzepte, Tools und Techniken für intelligente Systeme / Aurélien Géron ; deutsche Übersetzung von Kristian Rother & Thomas Demmig*. 2020.

[63] Ethem Alpaydın. *Introduction to Machine Learning / Ethem Alpaydin*. 2020.

[64] Daniel Sonnet. *Neuronale Netze kompakt: Vom Perceptron zum Deep Learning*. IT kompakt. Springer Fachmedien Wiesbaden, Wiesbaden, 2022.

[65] Diederik P. Kingma and Jimmy Ba. Adam: A Method for Stochastic Optimization, January 2017.

[66] Yirgalem Chebud, Ghinwa M. Naja, Rosanna G. Rivero, and Assefa M. Melesse. Water Quality Monitoring Using Remote Sensing and an Artificial Neural Network. *Water, Air, & Soil Pollution*, 223(8):4875–4887, October 2012.

[67] Yishan Zhang, Lun Wu, Huazhong Ren, Yu Liu, Yongqian Zheng, Yaowen Liu, and Jiaji Dong. Mapping Water Quality Parameters in Urban Rivers from Hyperspectral Images Using a New Self-Adapting Selection of Multiple Artificial Neural Networks. *Remote Sensing*, 12(2):336, January 2020.

[68] Y. LeCun, B. Boser, J. S. Denker, D. Henderson, R. E. Howard, W. Hubbard, and L. D. Jackel. Backpropagation Applied to Handwritten Zip Code Recognition. *Neural Computation*, 1(4):541–551, December 1989.

[69] Ian Goodfellow, Yoshua Bengio, and Aaron Courville. *Deep Learning: das umfassende Handbuch : Grundlagen, aktuelle Verfahren und Algorithmen, neue Forschungsansätze / Ian Goodfellow, Yoshua Bengio, Aaron Courville*. 2018.

[70] Philipp M. Maier, Sina Keller, and Stefan Hinz. Deep Learning with WASI Simulation Data for Estimating Chlorophyll a Concentration of Inland Water Bodies. *Remote Sensing*, 13(4):718, January 2021.

[71] Jiannan Cai, Jun Chen, Xianhui Dou, and Qianguo Xing. Using Machine Learning Algorithms With In Situ Hyperspectral Reflectance Data to Assess Comprehensive Water Quality of Urban Rivers. *IEEE Transactions on Geoscience and Remote Sensing*, 60:1–13, 2022.

[72] Erchan Aptoula and Sema Ariman. Chlorophyll-a Retrieval From Sentinel-2 Images Using Convolutional Neural Network Regression. *IEEE Geoscience and Remote Sensing Letters*, 19:1–5, 2022.

[73] *Optical Oceanography*. Elsevier, May 2014.

[74] Robert C. Wrigley and Alexander J. Horne. Remote sensing and lake eutrophication. *Nature*, 250(5463):213–214, July 1974.

[75] R. W. Preisendorfer. Hydrologic Optics. Volume 1. Introduction. Technical report, Honolulu : U.S. Dept. of Commerce, National Oceanic and Atmospheric Administration, Environmental Research Laboratories, Pacific Marine Environmental Laboratory, 1976.

[76] Ferdi L. Hellweger, Will Miller, and Kehinde Sarat Oshodi. Mapping Turbidity in the Charles River, Boston Using a High-resolution Satellite. *Environmental Monitoring and Assessment*, 132(1):311–320, September 2007.

[77] Kaire Toming, Tiit Kutser, Alo Laas, Margot Sepp, Birgot Paavel, and Tiina Nõges. First Experiences in Mapping Lake Water Quality Parameters with Sentinel-2 MSI Imagery. *Remote Sensing*, 8(8):640, August 2016.

[78] Milad Niroumand-Jadidi, Francesca Bovolo, Mariano Bresciani, Peter Gege, and Claudia Giardino. Water Quality Retrieval from Landsat-9 (OLI-2) Imagery and Comparison to Sentinel-2. *Remote Sensing*, 14(18):4596, January 2022.

[79] Claudia Giardino, Vittorio E. Brando, Arnold G. Dekker, Niklas Strömbeck, and Gabriele Candiani. Assessment of water quality in Lake Garda (Italy) using Hyperion. *Remote Sensing of Environment*, 109(2):183–195, July 2007.

[80] Kevin Sylvain Barbieux. Airborne Hyperspectral Imaging of Lakes. http://infoscience.epfl.ch/record/255561, 2018.

[81] Els Knaeps, Sindy Sterckx, and Dries Raymaekers. A Seasonally Robust Empirical Algorithm to Retrieve Suspended Sediment Concentrations in the Scheldt River. *Remote Sensing*, 2(9):2040–2059, August 2010.

[82] Claudia Giardino, Mariano Bresciani, Emiliana Valentini, Luca Gasperini, Rossano Bolpagni, and Vittorio E. Brando. Airborne hyperspectral data to assess suspended particulate matter and aquatic vegetation in a shallow and turbid lake. *Remote Sensing of Environment*, 157:48–57, February 2015.

[83] Lifei Wei, Zhou Wang, Can Huang, Yu Zhang, Zhengxiang Wang, Huiqiong Xia, and Liqin Cao. Transparency Estimation of Narrow Rivers by UAV-Borne Hyperspectral Remote Sensing Imagery. *IEEE Access*, 8:168137–168153, 2020.

[84] Alejandro Román, Antonio Tovar-Sánchez, Adam Gauci, Alan Deidun, Isabel Caballero, Emanuele Colica, Sebastiano D'Amico, and Gabriel Navarro. Water-Quality Monitoring with a UAV-Mounted Multispectral Camera in Coastal Waters. *Remote Sensing*, 15(1):237, January 2023.

[85] Lei Deng, Zhihui Mao, Xiaojuan Li, Zhuowei Hu, Fuzhou Duan, and Yanan Yan. UAV-based multispectral remote sensing for precision agriculture: A comparison between different cameras. *ISPRS Journal of Photogrammetry and Remote Sensing*, 146:124–136, December 2018.

[86] Telmo Adão, Jonáš Hruška, Luís Pádua, José Bessa, Emanuel Peres, Raul Morais, and Joaquim João Sousa. Hyperspectral Imaging: A Review on UAV-Based Sensors, Data Processing and Applications for Agriculture and Forestry. *Remote Sensing*, 9(11):1110, November 2017.

[87] Richard H. Becker, Michael Sayers, Dustin Dehm, Robert Shuchman, Kaydian Quintero, Karl Bosse, and Reid Sawtell. Unmanned aerial system based spectroradiometer for monitoring harmful algal blooms: A new paradigm in water quality monitoring. *Journal of Great Lakes Research*, 45(3):444–453, June 2019.

[88] Georg Bareth, Helge Aasen, Juliane Bendig, Martin Leon Gnyp, Andreas Bolten, András Jung, René Michels, and Jussi Soukkamäki. Low-weight and UAV-based Hyperspectral Full-frame Cameras for Monitoring Crops: Spectral Comparison with Portable Spectroradiometer Measurements. *Photogrammetrie - Fernerkundung - Geoinformation*, 2015(1):69–79, February 2015.

[89] Heikki Saari, Ilkka Pölönen, Heikki Salo, Eija Honkavaara, Teemu Hakala, Christer Holmlund, Jussi Mäkynen, Rami Mannila, Tapani Antila, and Altti Akujärvi. Miniaturized hyperspectral imager calibration and UAV flight campaigns. volume 8889, pages 88891O–88891O–12, 2013.

[90] Bikram Pratap Banerjee, Simit Raval, and P. J. Cullen. UAV-hyperspectral imaging of spectrally complex environments. *International Journal of Remote Sensing*, 41(11):4136–4159, June 2020.

[91] Carmen Cillero Castro, Jose Antonio Domínguez Gómez, Jordi Delgado Martín, Boris Alejandro Hinojo Sánchez, Jose Luis Cereijo Arango, Federico Andrés Cheda Tuya, and Ramon Díaz-Varela. An UAV and Satellite Multispectral Data Approach to Monitor Water Quality in Small Reservoirs. *Remote Sensing*, 12(9):1514, January 2020.

[92] Lifei Wei, Can Huang, Yanfei Zhong, Zhou Wang, Xin Hu, and Liqun Lin. Inland Waters Suspended Solids Concentration Retrieval Based on PSO-LSSVM for UAV-Borne Hyperspectral Remote Sensing Imagery. *Remote Sensing*, 11(12):1455, January 2019.

[93] Yingying Gai, Dingfeng Yu, Yan Zhou, Lei Yang, Chao Chen, and Jun Chen. An Improved Model for Chlorophyll-a Concentration Retrieval in Coastal Waters Based on UAV-Borne Hyperspectral Imagery: A Case Study in Qingdao, China. *Water*, 12(10):2769, October 2020.

[94] Erin Lee Hestir, Vittorio E. Brando, Mariano Bresciani, Claudia Giardino, Erica Matta, Paolo Villa, and Arnold G. Dekker. Measuring freshwater aquatic ecosystems: The need for a hyperspectral global mapping satellite mission. *Remote Sensing of Environment*, 167:181–195, September 2015.

[95] Chuiqing Zeng, Murray Richardson, and Douglas J. King. The impacts of environmental variables on water reflectance measured using a lightweight unmanned aerial vehicle (UAV)-based spectrometer system. *ISPRS Journal of Photogrammetry and Remote Sensing*, 130:217–230, August 2017.

[96] Hanting Ying, Kai Xia, Xinxi Huang, Hailin Feng, Yinhui Yang, Xiaochen Du, and Leijun Huang. Evaluation of water quality based on UAV images and the IMP-MPP algorithm. *Ecological Informatics*, 61:101239, March 2021.

[97] Jayan Wijesingha, Thomas Astor, Damian Schulze-Brüninghoff, Matthias Wengert, and Michael Wachendorf. Predicting Forage Quality of Grasslands Using UAV-Borne Imaging Spectroscopy. *Remote Sensing*, 12(1):126, January 2020.

[98] Mary B. Stuart, Andrew J. S. McGonigle, and Jon R. Willmott. Hyperspectral Imaging in Environmental Monitoring: A Review of Recent Developments and Technological Advances in Compact Field Deployable Systems. *Sensors*, 19(14):3071, January 2019.

[99] Ralph Holst. Grundlagen – Einsatzgebiete – rechtliche Rahmenbedingungen für Drohnensysteme. *Bautechnik*, 95(10):699–704, 2018.

[100] A. Burkart, S. Cogliati, A. Schickling, and U. Rascher. A Novel UAV-Based Ultra-Light Weight Spectrometer for Field Spectroscopy. *IEEE Sensors Journal*, 14(1):62–67, January 2014.

[101] J. Kern, A. Schenk, and S. Hinz. Radiometric Calibration of a UAV-Mounted Hyperspectral Snapshot Camera with Focus on Uniform Spectral Sampling. In *2018 9th Workshop on Hyperspectral Image and Signal Processing: Evolution in Remote Sensing (WHISPERS)*, pages 1–5, September 2018.

[102] Minsu Kim, Joong Yong Park, Yuri Kopilevich, Grady Tuell, and William Philpot. Correction for reflected sky radiance in low-altitude coastal hyperspectral images. *Applied Optics*, 52(32):7732–7744, November 2013.

[103] P Gege and P Groetsch. A spectral model for correcting sun glint and sky glint. 2016.

[104] Philipp M. M. Groetsch, Robert Foster, and Alexander Gilerson. Exploring the limits for sky and sun glint correction of hyperspectral above-surface reflectance observations. *Applied Optics*, 59(9):2942–2954, March 2020.

[105] Patrick Clifton Gray, Anna E. Windle, Julian Dale, Ivan B. Savelyev, Zackary I. Johnson, Greg M. Silsbe, Gregory D. Larsen, and David W. Johnston. Robust ocean color from drones: Viewing geometry, sky reflection removal, uncertainty analysis, and a survey of the Gulf Stream front. *Limnology and Oceanography: Methods*, 20(10):656–673, 2022.

[106] Philipp M. M. Groetsch, Peter Gege, Stefan G. H. Simis, Marieke A. Eleveld, and Steef W. M. Peters. Validation of a spectral correction procedure for sun and sky reflections in above-water reflectance measurements. *Optics Express*, 25(16):A742–A761, August 2017.

[107] Carlos Carrizo, Alexander Gilerson, Robert Foster, Andrii Golovin, and Ahmed El-Habashi. Characterization of radiance from the ocean surface by hyperspectral imaging. *Optics Express*, 27(2):1750–1768, January 2019.

[108] Ryan E. O'Shea, Ryan E. O'Shea, Samuel R. Laney, and Zhongping Lee. Evaluation of glint correction approaches for fine-scale ocean color measurements by lightweight hyperspectral imaging spectrometers. *Applied Optics*, 59(7):B18–B34, March 2020.

[109] Anna Göritz, Stella A. Berger, Peter Gege, Hans-Peter Grossart, Jens C. Nejstgaard, Sebastian Riedel, Rüdiger Röttgers, and Christian Utschig. Retrieval of Water Constituents from Hyperspectral In-Situ Measurements under Variable Cloud Cover—A Case Study at Lake Stechlin (Germany). *Remote Sensing*, 10(2):181, February 2018.

[110] H. Aasen, J. Bendig, A. Bolten, S. Bennertz, M. Willkomm, and G. Bareth. Introduction and preliminary results of a calibration for full-frame hyperspectral cameras to monitor agricultural crops with UAVs. In *ISPRS - International Archives of the Photogrammetry, Remote Sensing and Spatial Information Sciences*, volume XL-7, pages 1–8. Copernicus GmbH, September 2014.

[111] Helge Aasen, Andreas Burkart, Andreas Bolten, and Georg Bareth. Generating 3D hyperspectral information with lightweight UAV snapshot cameras for vegetation monitoring: From camera calibration to quality assurance. *ISPRS Journal of Photogrammetry and Remote Sensing*, 108:245–259, October 2015.

[112] Guijun Yang, Changchun Li, Yanjie Wang, Huanhuan Yuan, Haikuan Feng, Bo Xu, and Xiaodong Yang. The DOM Generation and Precise Radiometric Calibration of a UAV-Mounted Miniature Snapshot Hyperspectral Imager. *Remote Sensing*, 9(7):642, July 2017.

[113] Christian J. Köppl, Radu Malureanu, Carsten Dam-Hansen, Sheng Wang, Hongxiao Jin, Stefano Barchiesi, Juan M. Serrano Sandí, Rafael Muñoz-Carpena, Mark Johnson, Ana M. Durán-Quesada, Peter Bauer-Gottwein, Ursula S. McKnight, and Monica Garcia. Hyperspectral reflectance measurements from UAS under intermittent clouds: Correcting irradiance measurements for sensor tilt. *Remote Sensing of Environment*, 267:112719, December 2021.

[114] Charles Abolt, Todd Caldwell, Brad Wolaver, and Henry Pai. Unmanned aerial vehicle-based monitoring of groundwater inputs to surface waters using an economical thermal infrared camera. *Optical Engineering*, 57(5):053113, May 2018.

[115] Yanpeng Cao and Christel-Loic Tisse. Single-image-based solution for optics temperature-dependent nonuniformity correction in an uncooled long-wave infrared camera. *Optics Letters*, 39(3):646–648, February 2014.

[116] Katharina Fricke, Björn Baschek, Alexander Jenal, Caspar Kneer, Immanuel Weber, Jens Bongartz, Jens Wyrwa, and Andreas Schöl. Observing Water Surface Temperature from Two Different Airborne

Platforms over Temporarily Flooded Wadden Areas at the Elbe Estuary—Methods for Corrections and Analysis. *Remote Sensing*, 13(8):1489, January 2021.

[117] Adrian Kaehler and Gary Bradski. *Learning OpenCV 3 : Computer Vision in C++ with the OpenCV Library*, volume First edition. O'Reilly Media, Sebastopol, CA, 2016.

[118] Michele Meroni, Lorenzo Busetto, Luis Guanter, Sergio Cogliati, Giovanni Franco Crosta, Mirco Migliavacca, Cinzia Panigada, Micol Rossini, and Roberto Colombo. Characterization of fine resolution field spectrometers using solar Fraunhofer lines and atmospheric absorption features. *Applied Optics*, 49(15):2858–2871, May 2010.

[119] Alexander Kramida, Yuri Ralchenko, J. Reader, and and NIST ASD Team. NIST Atomic Spectra Database (ver. 5.8), 2020.

[120] Wolfgang Kohn and Riza Öztürk. *Statistik für Ökonomen: Datenanalyse mit R und SPSS*. Springer-Lehrbuch. Springer Berlin Heidelberg, Berlin, Heidelberg, 2017.

[121] Can Demirkesen and Uğur Murat Leloğlu. Estimation of noise model parameters for images taken by a full-frame hyperspectral camera. In *Image and Signal Processing for Remote Sensing XXI*, volume 9643, page 96430G. International Society for Optics and Photonics, October 2015.

[122] Klajdi Sotiri. *Integrated Sediment Yield and Stock Assessment for the Passaúna Reservoir, Brazil*. PhD thesis, 2020.

[123] Klajdi Sotiri, Stephan Hilgert, and Stephan Fuchs. Sediment classification in a Brazilian reservoir: Pros and cons of parametric low frequencies:. *Advances in Oceanography and Limnology*, 10(1), May 2019.

[124] Christine da Fonseca Xavier, Leda Neiva Dias, and Renato Fernando Brunkow. QUALIDADE DAS ÁGUAS DOS RESERVATÓRIOS DO ESTADO DO PARANÁ. Technical report, IAP - Instituto Ambiental do Paraná, 2017.

[125] Adrie F. G. Jacobs, Bert G. Heusinkveld, Aline Kraai, and Krijn P. Paaijmans. Diurnal temperature fluctuations in an artificial small shallow water body. *International Journal of Biometeorology*, 52(4):271–280, March 2008.

[126] Nikki Vercauteren, Hendrik Huwald, Elie Bou-Zeid, John S. Selker, Ulrich Lemmin, Marc B. Parlange, and Ivan Lunati. Evolution of superficial lake water temperature profile under diurnal radiative forcing. *Water Resources Research*, 47(9), 2011.

[127] Leonore S. Clesceri, American Public Health Association, American Water Works Association, and Water Pollution Control Federation. *Standard Methods: For the Examination of Water and Wastewater*. 1998.

[128] Klajdi Sotiri, Stephan Hilgert, and Stephan Fuchs. Sediment classification in a Brazilian reservoir: Pros and cons of parametric low frequencies: Parametric echo sounders for sediment classification. *Advances in Oceanography and Limnology*, 10(1), May 2019.

[129] Pablo Fernández Alcantarilla, Adrien Bartoli, and Andrew J. Davison. KAZE Features. In Andrew Fitzgibbon, Svetlana Lazebnik, Pietro Perona, Yoichi Sato, and Cordelia Schmid, editors, *Computer Vision – ECCV 2012*, Lecture Notes in Computer Science, pages 214–227, Berlin, Heidelberg, 2012. Springer.

[130] Jürgen Schwoerbel and Heinz Brendelberger. *Einführung in die Limnologie: Stoffhaushalt - Lebensgemeinschaften - Technologie*. Springer, Berlin, Heidelberg, 2022.

[131] J. M. Anderson, R. W. Duck, and J. McManus. Thermal radiometry: A rapid means of determining surface water temperature variations in lakes and reservoirs. *Journal of Hydrology*, 173(1):131–144, December 1995.

[132] Richard G. Lathrop and Thomas M. Lillesand. Calibration of thematic mapper thermal data for water surface temperature mapping: Case study on the Great Lakes. *Remote Sensing of Environment*, 22(2):297–307, July 1987.

[133] Christian E Torgersen, Russell N Faux, Bruce A McIntosh, Nathan J Poage, and Douglas J Norton. Airborne thermal remote sensing for water temperature assessment in rivers and streams. *Remote Sensing of Environment*, 76(3):386–398, June 2001.

[134] Jörg Albertz. *Einführung in die Fernerkundung: Grundlagen der Interpretation von Luft- und Satellitenbildern / Jörg Albertz.* 2009.

[135] Austin M. Jensen, Bethany T. Neilson, Mac McKee, and YangQuan Chen. Thermal remote sensing with an autonomous unmanned aerial remote sensing platform for surface stream temperatures. In *2012 IEEE International Geoscience and Remote Sensing Symposium*, pages 5049–5052, July 2012.

[136] Stephen J Dugdale. A practitioner's guide to thermal infrared remote sensing of rivers and streams: Recent advances, precautions and considerations. *WIREs Water*, 3(2):251–268, 2016.

[137] Thomas Luhmann. *Nahbereichsphotogrammetrie: Grundlagen, Methoden und Anwendungen / Thomas Luhmann.* 2010.

[138] Alistair Brown. Sub-100g uncooled thermal imaging camera design. In *Electro-Optical and Infrared Systems: Technology and Applications V*, volume 7113, pages 165–171. SPIE, October 2008.

[139] Olivier Riou, Stephane Berrebi, and Pierre Bremond. Nonuniformity correction and thermal drift compensation of thermal infrared camera. In *Thermosense XXVI*, volume 5405, pages 294–302. SPIE, April 2004.

[140] Robert M. Haralick, Stanley R. Sternberg, and Xinhua Zhuang. Image Analysis Using Mathematical Morphology. *IEEE Transactions on Pattern Analysis and Machine Intelligence*, PAMI-9(4):532–550, July 1987.

[141] Jean-Luc Liardon and D. A. Barry. Adaptable imaging package for remote vehicles. *HardwareX*, 2:1–12, October 2017.

[142] Jennifer E. Kay, Stephanie K. Kampf, Rebecca N. Handcock, Keith A. Cherkauer, Alan R. Gillespie, and Stephen J. Burges. Accuracy of Lake and Stream Temperatures Estimated from Thermal Infrared Images1. *JAWRA Journal of the American Water Resources Association*, 41(5):1161–1175, 2005.

[143] S. K. McFEETERS. The use of the Normalized Difference Water Index (NDWI) in the delineation of open water features. *International Journal of Remote Sensing*, 17(7):1425–1432, May 1996.

[144] Claudia Giardino, Gabriele Candiani, Mariano Bresciani, Zhongping Lee, Stefano Gagliano, and Monica Pepe. BOMBER: A tool for estimating water quality and bottom properties from remote sensing images. *Computers & Geosciences*, 45:313–318, August 2012.

[145] Fabian Pedregosa, Gaël Varoquaux, Alexandre Gramfort, Vincent Michel, Bertrand Thirion, Olivier Grisel, Mathieu Blondel, Peter Prettenhofer, Ron Weiss, Vincent Dubourg, Jake Vanderplas, Alexandre Passos, David Cournapeau, Matthieu Brucher, Matthieu Perrot, and Édouard Duchesnay. Scikit-learn: Machine Learning in Python. *Journal of Machine Learning Research*, 12(85):2825–2830, 2011.

[146] François Chollet. *Deep learning mit Python und Keras: das Praxis-Handbuch vom Entwickler der Keras-Bibliothek / Francois Chollet ; Übersetzung aus dem Amerikanischen von Knut Lorenzen.* 2018.

[147] Martın Abadi, Paul Barham, Jianmin Chen, Zhifeng Chen, Andy Davis, Jeffrey Dean, Matthieu Devin, Sanjay Ghemawat, Geoffrey Irving, Michael Isard, Manjunath Kudlur, Josh Levenberg, Rajat Monga, Sherry Moore, Derek G Murray, Benoit Steiner, Paul Tucker, Vijay Vasudevan, Pete Warden, Martin Wicke, Yuan Yu, and Xiaoqiang Zheng. TensorFlow: A system for large-scale machine learning.

[148] Xin Pan, Zhangjun Wang, Habib Ullah, Chao Chen, Xiufen Wang, Xianxin Li, Hui Li, Quanfeng Zhuang, Boyang Xue, and Yang Yu. Evaluation of Eutrophication in Jiaozhou Bay via Water Color Parameters Determination with UAV-Borne Hyperspectral Imagery. *Atmosphere*, 14(2):387, February 2023.

[149] Martin Søndergaard, Jens Peder Jensen, and Erik Jeppesen. Role of sediment and internal loading of phosphorus in shallow lakes. *Hydrobiologia*, 506(1):135–145, November 2003.

[150] C. H. Whitlock. An estimate of the influence of sediment concentration and type on remote sensing penetration depth for various coastal waters. Technical Report NASA-TM-X-73906, March 1976.

[151] I. Pölönen, H.-H. Puupponen, E. Honkavaara, A. Lindfors, H. Saari, L. Markelin, T. Hakala, and K. Nurminen. UAV-based hyperspectral monitoring of small freshwater area. page 923912, October 2014.

[152] Cengiz Koparan, Ali Bulent Koc, Charles V. Privette, Calvin B. Sawyer, and Julia L. Sharp. Evaluation of a UAV-Assisted Autonomous Water Sampling. *Water*, 10(5):655, May 2018.

[153] Dinesh Manoharan, C. Gajendran, M.K. Padmanabhan, S. Vignesh, S. Rajesh, and G.D. Bhuvaneshwaran. Design and development of autonomous amphibious unmanned aerial vehicle for in situ water quality assessment and water sampling. *Journal of Unmanned Vehicle Systems*, 9(3):182–204, September 2021.

[154] Juha Suomalainen, Raquel A. Oliveira, Teemu Hakala, Niko Koivumäki, Lauri Markelin, Roope Näsi, and Eija Honkavaara. Direct reflectance transformation methodology for drone-based hyperspectral imaging. *Remote Sensing of Environment*, 266:112691, December 2021.

[155] RedEdge-P - Drone Sensors. *AgEagle Aerial Systems Inc.*, October 2023.

[156] Björn Baschek, Katharina Fricke, Katja Dörnhöfer, and Natascha Oppelt. Grundlagen und Möglichkeiten der passiven Fernerkundung von Binnengewässern. In *Handbuch Angewandte Limnologie: Grundlagen - Gewässerbelastung - Restaurierung - Aquatische Ökotoxikologie - Bewertung - Gewässerschutz*, chapter 1.7, pages 1–28. John Wiley & Sons, Ltd, 2018.

[157] Paul Naethe, Maryam Asgari, Caspar Kneer, Michel Knieps, Alexander Jenal, Immanuel Weber, Tina Moelter, Filip Dzunic, Paul Deffert, Edvinas Rommel, Michael Delaney, Björn Baschek, Gilles Rock, Jens Bongartz, and Andreas Burkart. Calibration and Validation from Ground to Airborne and Satellite Level: Joint Application of Time-Synchronous Field Spectroscopy, Drone, Aircraft and Sentinel-2 Imaging. *PFG – Journal of Photogrammetry, Remote Sensing and Geoinformation Science*, 91(1):43–58, March 2023.

[158] Mario Ernesto Jijón-Palma, Jens Kern, Caisse Amisse, and Jorge Antonio Silva Centeno. Improving stacked-autoencoders with 1D convolutional-nets for hyperspectral image land-cover classification. *Journal of Applied Remote Sensing*, 15(2):026506, April 2021.